MEASUREMENT OF (ANTI-)NEUTRINO–NUCLEON STRUCTURE FUNCTIONS IN CHORUS EXPERIMENT

A THESIS SUBMITTED TO
THE GRADUATE SCHOOL OF NATURAL AND APPLIED SCIENCES
OF
MIDDLE EAST TECHNICAL UNIVERSITY

BY

SAMİ KAMA

IN PARTIAL FULFILLMENT OF THE REQUIREMENTS
FOR
THE DEGREE OF MASTER OF SCIENCE
IN
PHYSICS

AUGUST 2005

Approval of the Graduate School of Natural and Applied Sciences

Prof. Dr. Canan Özgen
Director

I certify that this thesis satisfies all the requirements as a thesis for the degree of Master of Science.

Prof. Dr. Sinan Bilikmen
Head of Department

This is to certify that we have read this thesis and that in our opinion it is fully adequate in scope and quality, as a thesis for the degree of Master of Science.

Assoc. Prof. Dr. Meltem Serin
Supervisor

Examining Committee Members

Prof. Dr. Ali Ulvi Yılmazer	(ANKARA. UNI., PHYS ENG)	
Assoc. Prof. Dr. Meltem Serin	(METU, PHYS)	
Dr. Jaap Panman	(CERN)	
Prof. Dr. Gürsevil Turan	(METU, PHYS)	
Assoc. Prof. Dr. Bayram Tekin	(METU, PHYS)	

I hereby declare that all information in this document has been obtained and presented in accordance with academic rules and ethical conduct. I also declare that, as required by these rules and conduct, I have fully cited and referenced all material and results that are not original to this work.

Name, Last name : Sami KAMA

Signature :

ABSTRACT

MEASUREMENT OF (ANTI-)NEUTRINO–NUCLEON STRUCTURE FUNCTIONS IN CHORUS EXPERIMENT

KAMA, Sami

M.Sc., Department of Physics

Supervisor : Assoc. Prof. Dr. Meltem Serin

August 2005, 89 pages

In this work an analysis of the CHORUS (anti-)neutrino-nucleon scattering data taken on lead–scintillator calorimeter during the 1998 run is presented. The differential cross-sections are measured in the range of $0.01 \leq x \leq 0.7$, $0.05 \leq y \leq 0.95$, $10 \leq E_\nu \leq 200$GeV for both anti-neutrino and neutrino beam modes. The anti-neutrino and neutrino–nucleon structure functions $2xF_1$, F_2 and xF_3 is extracted by making 2, 3 and 6-parameter fits to the measured differential cross-sections. The comparisons of these results with the earlier experiments, CDHSW and CCFR is given.

Keywords: (Anti-)Neutrino–Nucleon Structure Functions, Neutrino, CHORUS, differential cross-section measurement.

ÖZ

CHORUS DENEYİNDE (ANTİ-)NÖTRİNO–NÜKLEON YAPI FONKSİYONLARININ ÖLÇÜMÜ

KAMA, Sami

Yüksek Lisans, Fizik Bölümü

Tez Yöneticisi : Assoc. Prof. Dr. Meltem Serin

Ağustos 2005, 89 sayfa

Bu çalışmada CHORUS deneyinin kurşun–sintilatör kalorimetresinden 1998 yılında alınan veriler ile yapılan (anti-)nötrino–nükleon saçılması ile ilgili bir analiz sunulmaktadır. Anti-nötrino ve nötrino akı tipleri için $0.01 \leq x \leq 0.7$, $0.05 \leq y \leq 0.95$, $10 \leq E_\nu \leq 200$GeV aralığında diferansiyel tesir kesiti ölçümü yapılmıştır. Anti-nötrino ve nötrino–nükleon yapı fonksiyonları $2xF_1$, F_2 ve xF_3'ü ölçümü yapılan tesir kesitine 2, 3 ve 6 değişkenli oturtmalar yaparak belirlenmiştir. Bu sonuçların daha önceki CDHSW ve CCFR deneylerinin sonuçları ile karşılaştırılmalarıda sunulmaktadır.

Anahtar Kelimeler: (Anti-)Nötrino–Nükleon yapı fonksiyonları, Nötrino, CHORUS, diferansiyel tesir kesiti ölçümü.

To the angels on earth, Sabri Kama and Figen (Altınbozar) Kama.

ACKNOWLEDGEMENTS

I have taken my first particle physics courses from Perihan Tolun and met with the high energy phyiscs. In the fall of 2000 I did a project on the higgs search at LHC with Meltem Serin, increasing my interest in HEP. In the following summer, she suggested me to CERN as a summer student. The 3 months at CERN helped me to choose the field of research in my academic career. In the masters program Meltem Serin gave me the subject of this thesis and guided me as supervisor. She and Perihan Tolun, the METU CHORUS group leader, suggested me to CHORUS group to work on the related analysis in the CHORUS-DIS group. Meltem Serin has spent a great effort to send me to the CERN for the workshops and studies, many times overcoming the bureaucratical and financial problems. She supported and encouraged me when I was down.

Jaap Panman accepted me in his group and arranged some funds for me to study at the CERN. His experience and knowledge inspired me. He corrected and guided me, explained things and made creative comments.

Rolf Oldeman has done the first analysis on the subject and written the Mickey and the analysis chain tools. I've continued his work, added new tools, updated the some parts in his programs, adding new efficiencies and systematics studies. He explained to me how the tools work. His programming style improved my programming, comments helped me understand the code easier. Without his work this study was not possible.

Ilya Tsoukerman prepared the EFICASS samples for the efficiency studies. He was always helpful, always answering my questions. Andrei Artamanov helped me about spectrometer related things, programming issues and the data. Helge Meinhard thought me how to prepare the chorus offline setup and also made useful suggestions about computational problems.

Alfredo Cocco and Marcello Messina invited me to the Napoli as part of INFN-Napoli. They helped me on the detector efficiency studies. They also, with Roberto Santorelli,

prepared the NN for the hadronic shower and event vertex measurements.
Demet Gülen helped me with the statistics and provided moral support.
I would like to thank all of them for their help and support.
I would like to thank my sister, Fulya Kama for the proofreading.
I also would like to mention that due to frequent power failures I lost early versions of the updates, utilities, several hardware pieces (mostly HDDs) and very precious time and effort.

TABLE OF CONTENTS

LIST OF TABLES

LIST OF FIGURES

CHAPTER 1

INTRODUCTION

Since their postulation in the early 1930's and discovery in 1953 neutrinos have been a very interesting subject in the physics. According to the standard model (SM) they are chargeless, massless particles with no magnetic moment which interacts with matter only via weak interactions. Although now it is known that the neutrinos have mass [1], they will be assumed massless throughout this study.

Nucleons, protons and neutrons, are composed of inner constituents called quarks and gluons [2]. The interactions of quarks and qluons have been described by the theory of quantum chromodynamics (QCD). Neutrinos' property of interacting only via weak interactions makes them great probes for nucleon's inner structure. In this thesis the inner structure of the nucleon was studied by measuring the differential cross-section of the neutrino-nucleon scattering in CHORUS detector. Neutrinos interact with matter in two ways, first one is via a neutral Z boson exchange, second is via a charged W boson exchange. These interactions are named as neutral current (NC) and charged current (CC) respectively. In CC neutrino-nucleon interactions, the final state is a μ^- and a hadronic final state(X) 1.1). In the anti-neutrino case, the final state contains μ^+ instead of μ^- (1.2).

$$\nu_\mu + N \rightarrow \mu^- + X, \tag{1.1}$$

$$\overline{\nu}_\mu + N \rightarrow \mu^+ + X \tag{1.2}$$

In this thesis N is the target of the calorimeter of the detector. The Feynman diagram for the process is given in figure 1.1. In the figure k and k' represents 4-momentum of incoming ν and outgoing μ, p and p' represents 4-momentum of incoming nucleon and outgoing hadronic final state. The q is the transferred 4-momentum and defined as $q = k - k' = p - p'$. If the q is small, that is nucleon is not destroyed, then the event is called a quasi-elastic (QE) scattering event. If the q is large, nucleon is destroyed and final state is a hadronic shower, then the event is called a deep inelastic scattering (DIS) event.

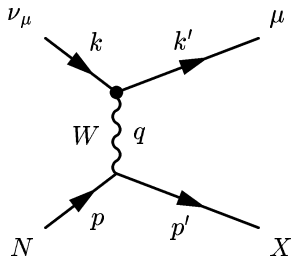

Figure 1.1: Feynman diagram for ν-nucleon deep inelastic scattering

1.1 Kinematics and Cross-section

Typical representation of a DIS event in laboratory frame is given in figure 1.2. In this study the observables of a DIS event are the muon momentum p_μ, muon angle θ_μ, total energy of the hadronic shower E_{had} or E_{shower}. Observing only the total energy of the hadronic shower makes this study an inclusive one. In single W exchange

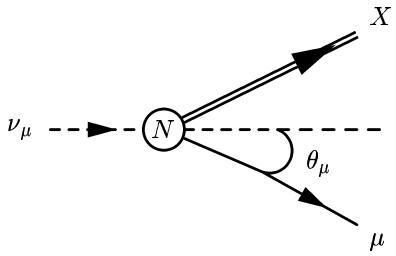

Figure 1.2: A typical DIS event. X is the final hadronic shower, θ_μ is the angle of μ with respect to direction of incoming ν.

approximation, neutrino-nucleon differential cross-section can be written in terms of E_ν, incoming neutrinos energy, $Q^2 = -q \cdot q$, the 4-momentum transfer squared, x, Bjorken variable $x = \frac{Q^2}{2\,q\cdot p}$, and y, the inelasticity $y = \frac{p\cdot q}{p\cdot k}$, [3, 4] as

$$\frac{d^2\sigma}{dxdy} = \frac{G_F^2 M_N E_\nu}{\pi(1+Q^2/M_W^2)^2}\left[\frac{1}{2}y^2\,2x\mathrm{F}_1(x,Q^2) + \left(1-y-\frac{M_N x y}{2E_\nu}\right)\mathrm{F}_2(x,Q^2)\right.$$

$$\pm \quad \left(y - \frac{1}{2}y^2\right) x\mathrm{F}_3(x,Q^2)\Big] \tag{1.3}$$

where G_F is Fermi constant, M_N nucleon mass, M_W W boson mass. The reconstruction of these variables from the measured quantities in the laboratory system is a matter of simple calculations

$$E_\nu = E_\mu + E_{had}, \tag{1.4}$$

$$y = \frac{E_{had}}{E_\nu}, \tag{1.5}$$

$$Q^2 = 2E_\nu(E_\mu - p_\mu \cos\theta_\mu) - m_\mu^2, \tag{1.6}$$

$$x = \frac{Q^2}{2M_N E_{had}}, \tag{1.7}$$

The x and Q^2 dependent functions F_1, F_2 and F_3 are called the structure functions of the nucleon. $2xF_1$ and F_2 contributes to the cross-section in both electromagnetic and weak interactions, whereas xF_3 contributes only in weak interactions and changes sign between neutrino and anti-neutrino interactions. In the kinematic domain of the experiment, $Q^2 \gg m_\mu^2$, which simplifies Q^2 to

$$Q^2 \approx 4E_\nu p_\mu \sin^2\frac{1}{2}\theta_m u \tag{1.8}$$

Also since $Q^2 \ll M_W^2$ the factor $\frac{1}{(1+Q^2/M_W^2)^2}$ can be taken as 1 in the equation 1.3.

1.2 The Parton Model

The cross-section equation, equation 1.3, does not make any assumption about the structure of the nucleon. However, it has been known that neutrinos interact with quarks in the nucleon [3]. In the "naïve" quark-parton model, partons carry a portion ξ of the total 4-momentum of the target nucleon. If the energy transferred to the parton is large, *i.e.* $(\xi p)^2 \approx (\xi p + q)^2 \approx 0$, then momentum fraction ξ can be appoximated to the $\xi = \frac{-q^2}{2p\cdot q} = x$ [4]. By using Callan-Gross relation, $2xF_1 = F_2$, neutrino-quark differential cross-section on free quarks in terms of s, the center-of-mass energy of the ν–q system, can be given as [2]

$$\frac{d\sigma}{dy}(\nu\, q) = \frac{d\sigma}{dy}(\overline{\nu}\,\overline{q}) = \frac{G_F^2 s}{\pi}, \tag{1.9}$$

$$\frac{d\sigma}{dy}(\nu\,\overline{q}) = \frac{d\sigma}{dy}(\overline{\nu}\,q) \;=\; \frac{G_F^2 s}{\pi}(1-y)^2 \tag{1.10}$$

For a quark in a nucleus, cross-section should be described in terms of weighted quark distribution function $q(\xi)$, which is defined in a way such that $\xi^{-1}q(\xi)d\xi$ is the number of the quarks in the nucleon with 4-momentum fraction between ξ and $\xi + d\xi$. Then neutrino-nucleon cross-section becomes

$$\frac{d^2\sigma^{\nu}}{dyd\xi} \;=\; \frac{G_F^2 M_N E_\nu}{\pi}\left(2q(\xi) + 2\overline{q}(\xi)(1-y)^2\right), \tag{1.11}$$

$$\frac{d^2\sigma^{\overline{\nu}}}{dyd\xi} \;=\; \frac{G_F^2 M_N E_\nu}{\pi}\left(2q(\xi)(1-y)^2 + 2\overline{q}(\xi)\right). \tag{1.12}$$

Using the equations 1.9, 1.10 and 1.3 we can find the relation between the structure functions and quark distribution as follows:

$$2xF_1 = F_2 \;=\; 2(q(\xi) + \overline{q}(\xi)), \tag{1.13}$$

$$xF_3 \;=\; 2(q(\xi) - \overline{q}(\xi)), \tag{1.14}$$

Since b and t quarks are too heavy for the domain of this study, relations 1.13 and 1.14 can be rewritten as

$$2xF_1^{\nu} = F_2^{\nu} \;=\; 2(d + \overline{u} + s + \overline{c}), \tag{1.15}$$

$$2xF_1^{\overline{\nu}} = F_2^{\overline{\nu}} \;=\; 2(\overline{d} + u + \overline{s} + c), \tag{1.16}$$

$$xF_3^{\nu} \;=\; 2(d - \overline{u} + s - \overline{c}), \tag{1.17}$$

$$xF_3^{\overline{\nu}} \;=\; 2(-\overline{d} + u - \overline{s} + c). \tag{1.18}$$

One can define the above equations for a isoscalar target, by averaging the neutron and proton structure functions, getting

$$2xF_1^{\nu N} = F_2^{\nu N} \;=\; d^p + \overline{d}^p + u^p + \overline{u}^p + 2s^p + 2\overline{c}^p, \tag{1.19}$$

$$2xF_1^{\overline{\nu} N} = F_2^{\overline{\nu} N} \;=\; d^p + \overline{d}^p + u^p + \overline{u}^p + 2\overline{s}^p + 2c^p, \tag{1.20}$$

$$xF_3^{\nu N} \;=\; d^p - \overline{d}^p + u^p - \overline{u}^p + 2s^p - 2\overline{c}^p, \tag{1.21}$$

$$xF_3^{\overline{\nu} N} \;=\; d^p - \overline{d}^p + u^p - \overline{u}^p - 2\overline{s}^p + 2c^p. \tag{1.22}$$

Assuming a symmetric sea quark distribution, $s=\overline{s}$ and $c=\overline{c}$, leads to $2xF_1^{\nu N} = 2xF_1^{\overline{\nu}N}$ and $F_2^{\nu N} = F_2^{\overline{\nu}N}$. The difference of the structure functions xF_3 for neutrinos and anti-neutrinos, $\Delta xF_3^N = xF_3^{\nu N} - xF_3^{\overline{\nu}N}$, is $4(s-c)$, which is in general non-zero.

It has been observed that the Callan-Gross relation is not exact; violations are usually expressed in terms of R:

$$R = \left(1 + \frac{4M_N^2 x^2}{Q^2}\right) \frac{F_2}{2xF_1} - 1, \tag{1.23}$$

where R can be interpreted as the ratio of the longitudinal and transverse cross-section, σ_L/σ_T. Non-zero values of R can be attributed in large part to higher order scattering, involving gluons, and to intrinsic transverse momenta of the nucleon constituents, which are not accounted for in the naïve parton model.

In this study the structure functions F_2 and xF_3 and the Callan-Gross R has been extracted, for the first time, on lead target with high statistics.

CHAPTER 2

THE EXPERIMENTAL SETUP

The CHORUS experiment was a neutrino oscillation experiment. It's main purpose was to search for the appearance of τ^- from the ν_μ beam. In 1998 the experiment was extended with some small changes in the detector [5]. Then it was proposed that the detector can also be used to study the CC ν–nucleon structure functions [6]. General picture of the detector can be seen in figure 2.1.

2.1 The Neutrino Beam

The neutrino beam for the oscillation study was produced at the West Area Neutrino Facility (WANF) [7]. Layout of the WANF can be seen in figure 2.2. To produce the (anti-)neutrino beam protons, accelerated to 450 GeV by SPS, directed to the beryllium target. The beryllium target was composed of 11 rods of 10 cm length and 3 mm diameter spaced 9 cm apart from each other to minimize the interactions of produced pions and kaons. Then these pions and kaons are focused or defocused according to their charge by two specially designed air core magnets called the horn and the reflector. Neutrino beam mode is selected by focusing positively charged pions and kaons and defocusing the negatively charged particles to minimize the anti-neutrino contamination. These π and K decay to ν_μ dominantly. Properties of the mesons related to neutrino production has been given in table 2.1. Most of these focused pions and kaons decay in flight, giving neutrinos with transverse momentum

$$p_T = \frac{m_{\pi,K}^2 - m_\mu^2}{2m_{\pi,K}} \sin\theta, \tag{2.1}$$

and longitudinal momentum

$$p_L = E\left(1 - \frac{m_\mu^2}{m_{\pi,K}^2}\right)\left(\frac{1}{2} + \frac{1}{2}\cos\theta\right), \tag{2.2}$$

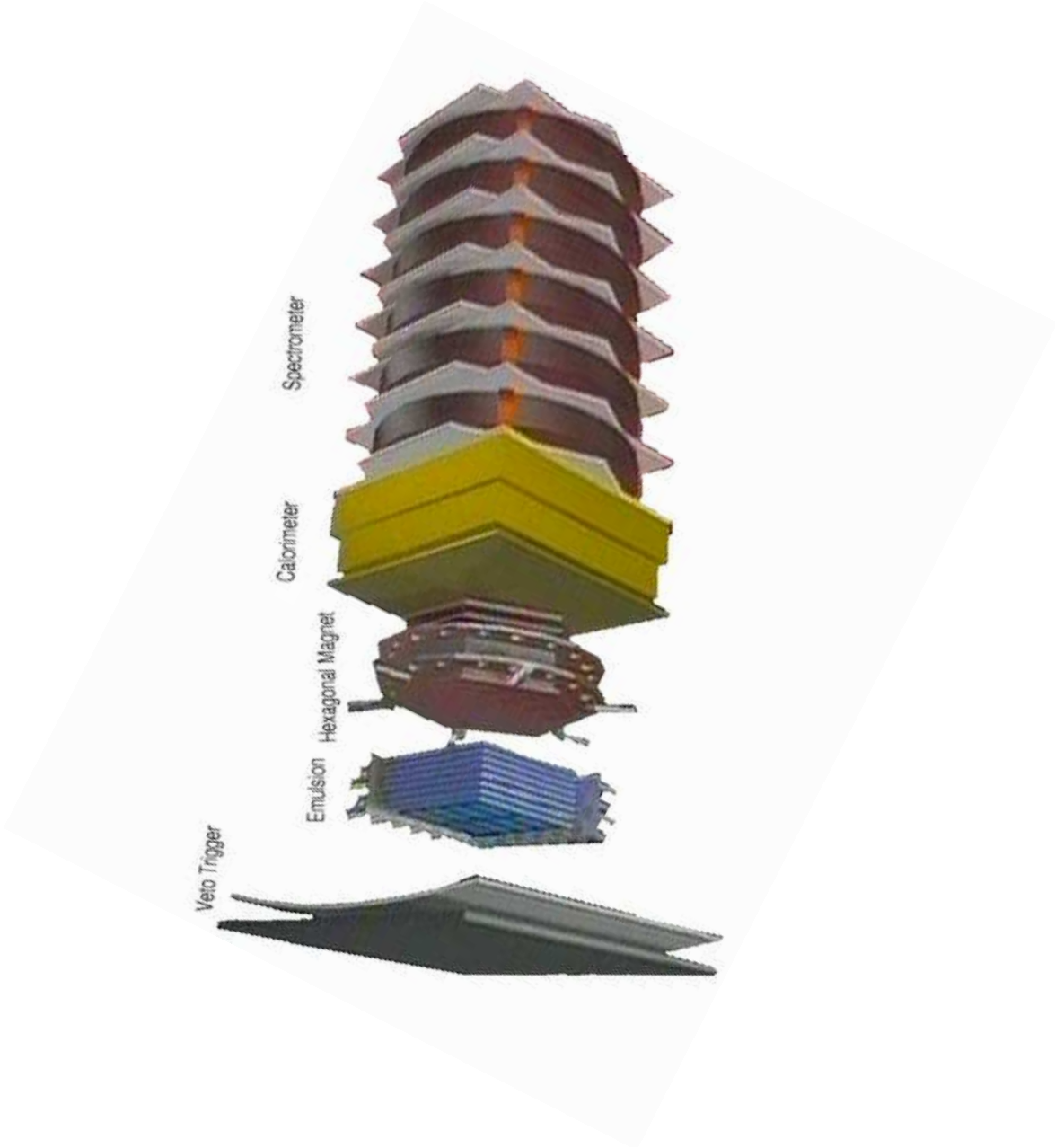

Figure 2.1: The layout of the detector. Hexagonal magnet and emulsion held in a 5°C cool box.

Figure 2.2: Layout of the West Area Neutrino Facility

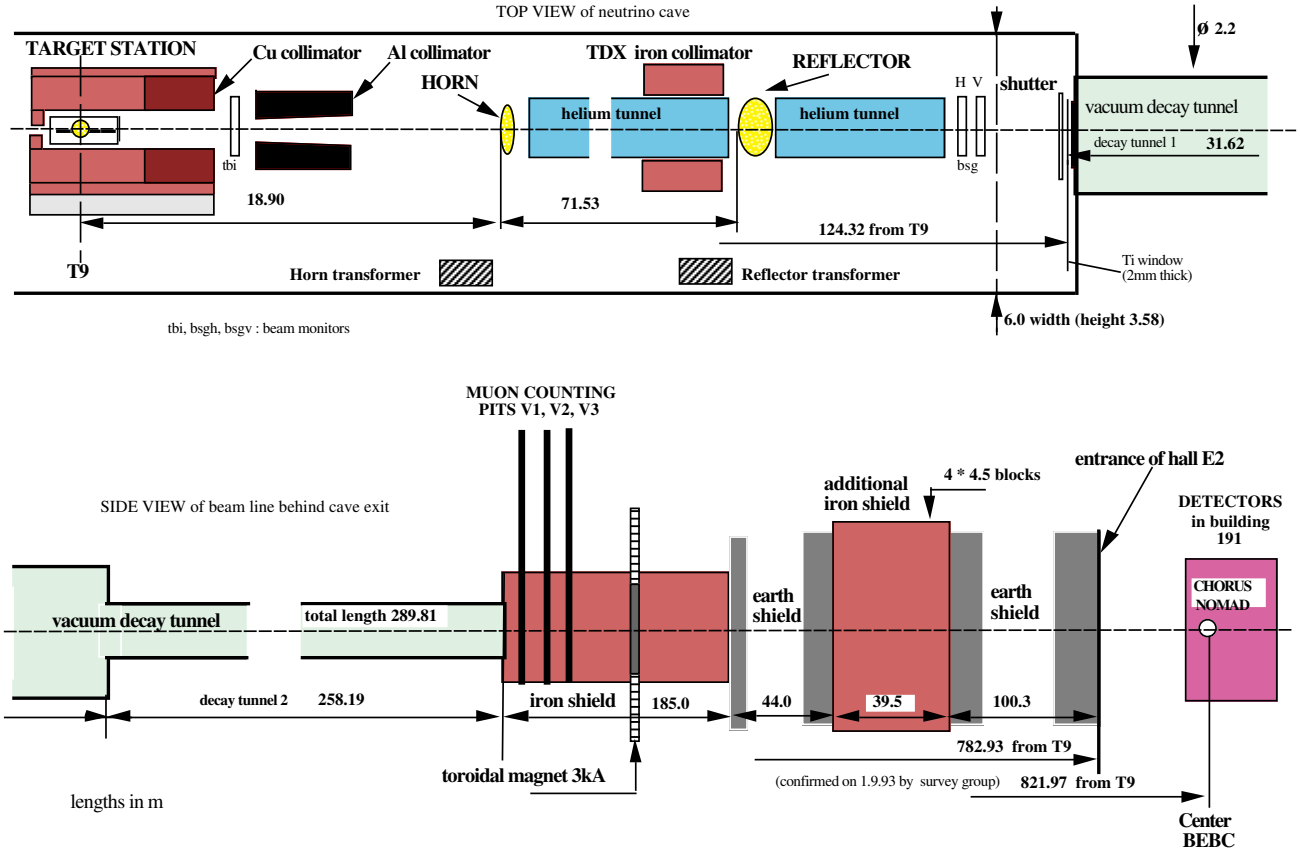

Table 2.1: Summary of the properties of the positively charged pions and kaons relevant for neutrino production. The same values hold for the charge conjugates.

Property	π^+	K^+
mass	139.6 MeV	493.7 MeV
lifetime	26.0 ns	12.4 ns
flight length	55.9 m/GeV	7.52 m/GeV
$Br(\rightarrow \mu^+\nu_\mu)$	99.987%	63.39%
maximum p_T of ν_μ	29.8 MeV	235.6 MeV
maximum p_L of ν_μ	0.427 p_π	0.944 p_K

with E being the energy of the π or K and θ being the angle between the mesons momentum vector in laboratory frame and the momentum vector of the neutrino in the mesons rest frame. μ's from the decay of the meson is either stopped by the approximately 370 meters of iron and earth shielding or defocused by the toroidal magnet. As a result, pretty few μ's reaches the detector.

2.2 The Calorimeter

The calorimeter of the CHORUS experiment is composed of three different parts, electro-magnetic part (EM), first hadronic part (HAD1) and second hadronic part (HAD2). The EM part contains four planes of which has 31 modules. Each module consists of 21 layers of grooved lead, 1.9 mm thick, interspersed with plastic scintillating fibers of 1 mm diameter, packed in a 0.8 mm stainless steel box. The length of a module is 262 cm and the width is 82.4 mm. There are 740 fibers in each module. On both sides of a module, the fibers are assembled into two bundles. Each bundle is coupled to a Photo-multiplier tube (PMT) via a Plexiglas light guide.

Each plane of the five planes of HAD1 sector contains 40 modules. Each module consists of 43 layers of lead, identical in width and groove size to those used for the EM sector, but with a length of 335 cm, and packed in a 1.0 mm steel box. There are 1554 scintillating plastic fibers in each module. At both ends, the fibers are collected into one bundle and coupled via a light guide to a PMT.

Each plane of the HAD2 sector contains 18 modules. Each module is built up as a

Table 2.2: Material composition of the calorimeter. The column "other" refers to scintillator material for EM, HAD1 and HAD2, and to PVC and aluminum for the streamer tubes.

	planes	density g/cm^2	lead g/cm^2	iron g/cm^2	other g/cm^2	x/x_0	x/λ_I
EM	4	37.33	34.67	1.89	0.77	5.60	0.203
HAD1	5	76.09	71.36	3.15	1.58	11.47	0.412
HAD2	5	92.23	87.93	2.36	1.94	14.02	0.495
Streamer Tubes	22	0.77			0.77	0.02	0.009
total		1007.86	935.13	35.11	37.62	150.29	5.556

sandwich of five layers of lead with a thickness of 1.6 cm and five layers of 4 mm thick scintillator strips, packed in 1.0 mm steel. The modules are 369 cm long and 20 cm wide. Each module is coupled via light guides to four PMTs, two on either side.

Eleven sets of streamer tube detectors, with a wire pitch of 1.05 cm and an active area of 3.7×3.7 m, are installed between the calorimeter planes. Each set consists of one plane with vertical wires and one with horizontal wires. These streamer tubes have not been used in the present analysis.

Since the calorimeter is used here as a target, the material composition is of particular importance. This is summarized in Table 2.2. The total thickness of the calorimeter corresponds to about 150 radiation lengths or 5.6 hadronic interaction lengths. Therefore, most hadrons from neutrino interactions in the emulsion target are fully contained. However, hadronic showers from neutrino interactions originating in the calorimeter itself may have a significant energy leakage into the muon spectrometer. This is taken into account by using the scintillators of the muon spectrometer as a shower tail catcher.

2.3 The Spectrometer

The main purpose of the CHORUS spectrometer is to identify muons and determine their charge, trajectory and momentum. Most of the particles have been absorbed by the calorimeter, thus spectrometer contains mainly μ and in some cases the shower particles that leak from the shower. Figure 2.1 and 2.3 shows the 6 iron-core, toroidal

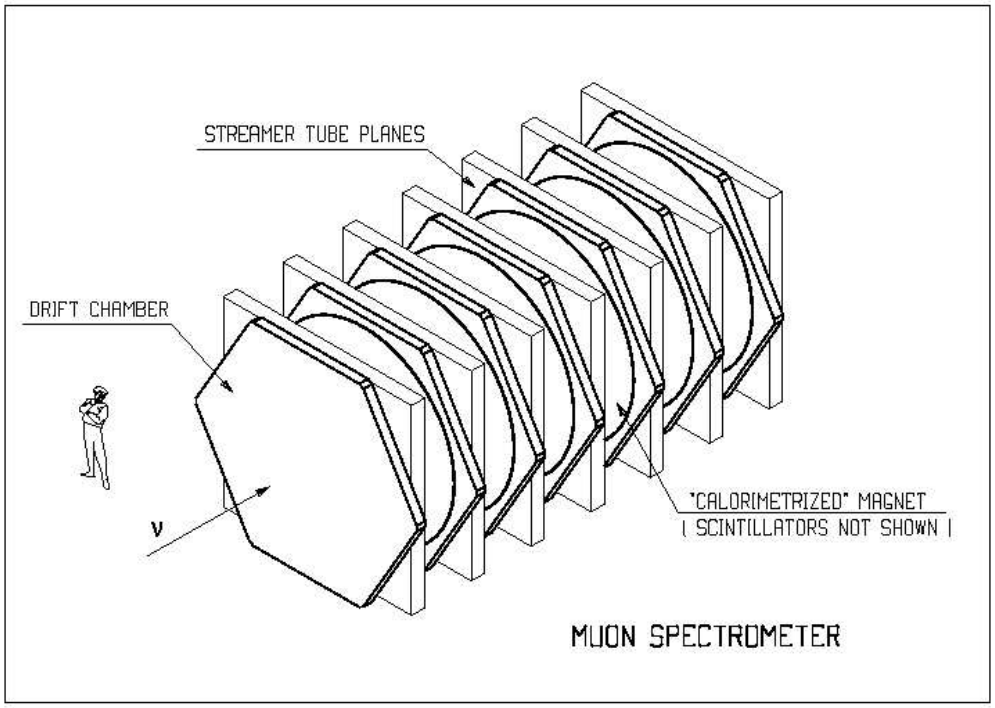

Figure 2.3: Layout of the spectrometer.

magnets and scintillator planes. Scintillator planes provide a measure of the leak from the calorimeter. As can be seen from the figure 2.4 toroidal iron-core magnets contain drift chambers, streamer tubes, scintillator planes and 2.5 cm thick iron disks with 375 cm outer diameter. Each scintillator plane is 0.5 cm thick and inserted in the 0.6 cm gaps between 20 iron disks. Iron Core magnets have been magnetized by water cooled copper coils passing through 8.5 cm diameter hole in the center. The 700 A current applied to the coils produces a nearly azimuthally symmetric toroidal field with average strength of 1.7 T. Direction of the current is inverted depending on the beam mode to defocus the contamination component μ.

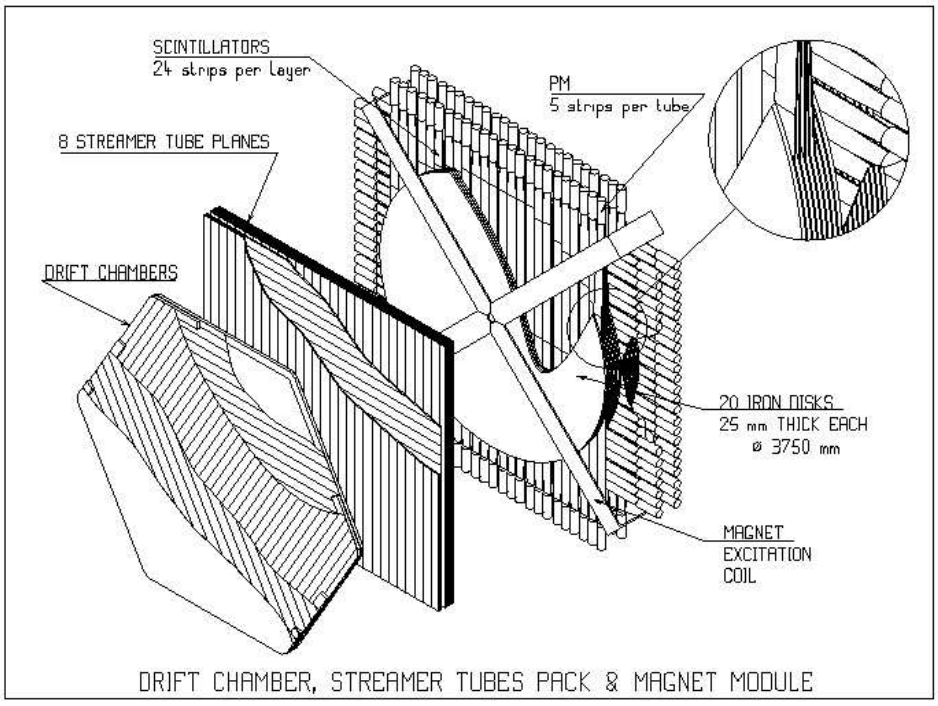

Figure 2.4: Layout of a section of the spectrometer.

CHAPTER 3

CHORUS DETECTOR EFFICIENCIES

In order to be able to extract the structure functions, a simulation of the detector is necessary. Detector simulation is done in several layers [8].

First layer is neutrino beam simulation. Parent mesons of neutrinos, π and K, are modelled with FLUKA [9] by NOMAD collaboration [10]. Then these mesons are fed into the GBEAM [11], the CHORUS neutrino beam simulator. GBEAM tracks and models their decays in the WANF tunnel creating 4-momentum, flavour and creation vertex as output.

Second layer is the generation of DIS events. DIS event simulation is handled with JETTA package [12].

The third and the last layer is the simulation of detector responses. Simulation of detector response is done with the EFICASS (Emulsion FIbers CAlorimeter and Spectrometer Simulation) package. The EFICASS package contains a very detailed description of the detector in the GEANT 3.21 framework [13]. Coordinate system in EFICASS is defined as a right-handed coordinate system with x-direction being parallel to the ν-beam.

Using these packages, smearing effects of the detector has been studied. For this study the reconstruction efficiency, θ and momentum resolution of the μ, event vertex location and hadronic shower energy resolution should be quantified. The smearing effects has been studied on EFICASS sample satisfiying following properties:

- y coordinate of the event vertex (y_{evnt}) should be between -90 cm. and 90 cm
- z coordinate of the event vertex (z_{evnt}) should be between -90 cm. and 90 cm
- μ^- originating from the DIS should go in to the spectrometer.

Also there are other criterias depending on the type of smearing.

3.1 Muon Efficiency

Muon efficiency can be splitted into two, muon reconstruction efficiency and momentum resolution. Reconstruction efficiency basically is the ratio of the found events over the total number of events. Momentum resolution is a measure of how close is the momentum of the found muon to its true value.

3.1.1 Reconstruction Efficiency

Reconstruction efficiency of the detector is mainly affected by the length of the tracks, thus the momentum of the muon, and the amount of the shower particles that leaks into the spectrometer. Low momentum of the muon may cause the reconstruction algorithms to fail, resulting it to be lost. High leakage from the calorimeter may cause falsely reconstructed muons as well as very large errors in the momentum of the reconstructed muon. Example events have been given in figure 3.1 and 3.2. In figures detector is given from the top view and side view. Identified μ tracks are drawn with lines. It can clearly be seen that increased activity in the spectrometer due to shower leakage causes falsely reconstructed muons.

The reconstruction efficiency (RE) of the detector depends on E_{had}, p_μ and the vertex plane (x_{vtx}) of the event (RE = RE(x_{vtx}, E_{had}, p_μ)). RE has been parameterized in bins of these variables. Function is split into 12 bins in x_{vtx}, 1 bin for each plane, 12 bins in E_{had} and 12 bins in p_μ. Bins in E_{had} and p_μ are spaced with respect to the event density in the region.

To define RE a *reconstructed event* should be defined first. A reconstructed event is defined as:

- The neural network algorithm should be able to find an event vertex x_{vtx} and a E_{had} for the event.
- μ track should be reconstructed from the begining of the spectrometer.
- μ track should have at least 7 scintillator hits in both y-direction and z-direction. It also should pass through at least 5 magnets.

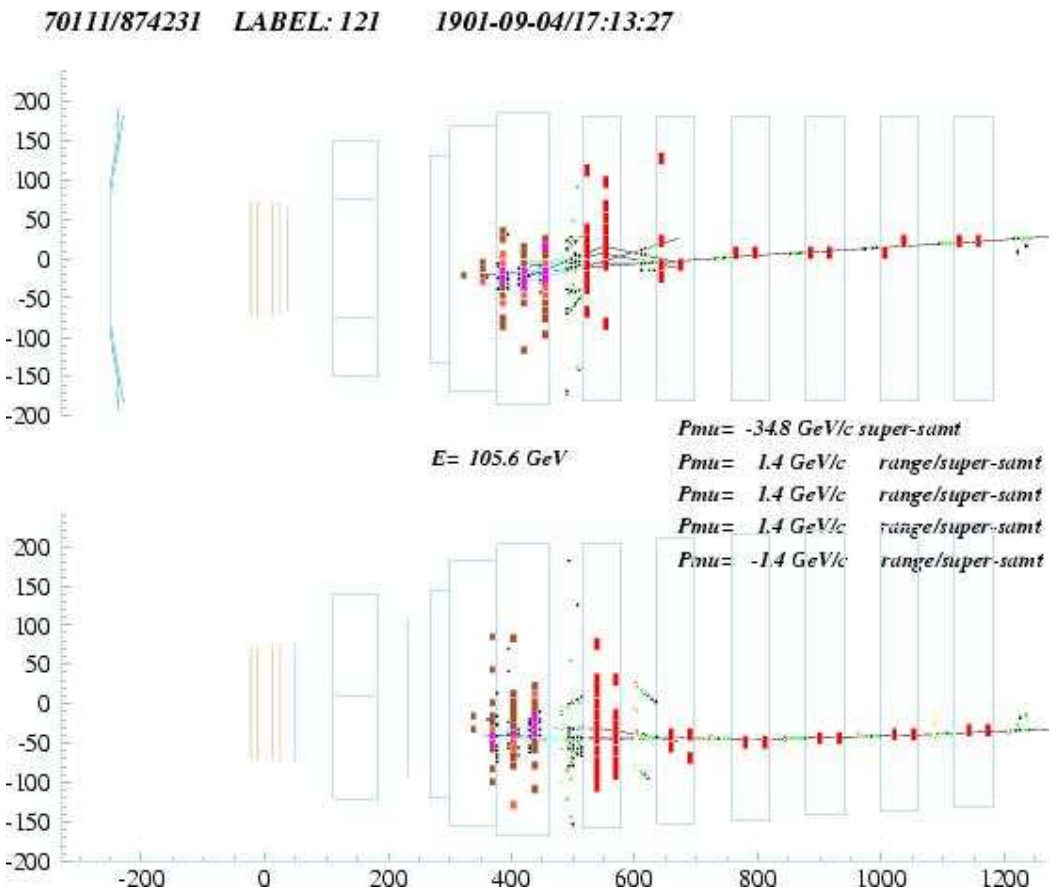

Figure 3.1: An example event reconstructed by the analysis tool. Shower leak is small and event occured in the middle of the calorimeter. 5 μ's have been found.

If there are more than one μ satisfying this criteria, μ with the highest momentum is choosen and the event is labeled as reconstructed. Choosen muon is also called a *good* μ.

The RE, then, is defined as the ratio of number of events reconstructed (N_{recons}) over total number of events (N_{total}) for each bin.

$$RE(x_{vtx}, E_{had}, p_\mu) = \frac{N_{recons}(x_{vtx}, E_{had}, p_\mu)}{N_{total}(x_{vtx}, E_{had}, p_\mu)}$$

Some example plots of the reconstruction efficiency can be seen in the figures 3.3 and 3.4. This function describes the reconstruction efficiency of the detector better than the

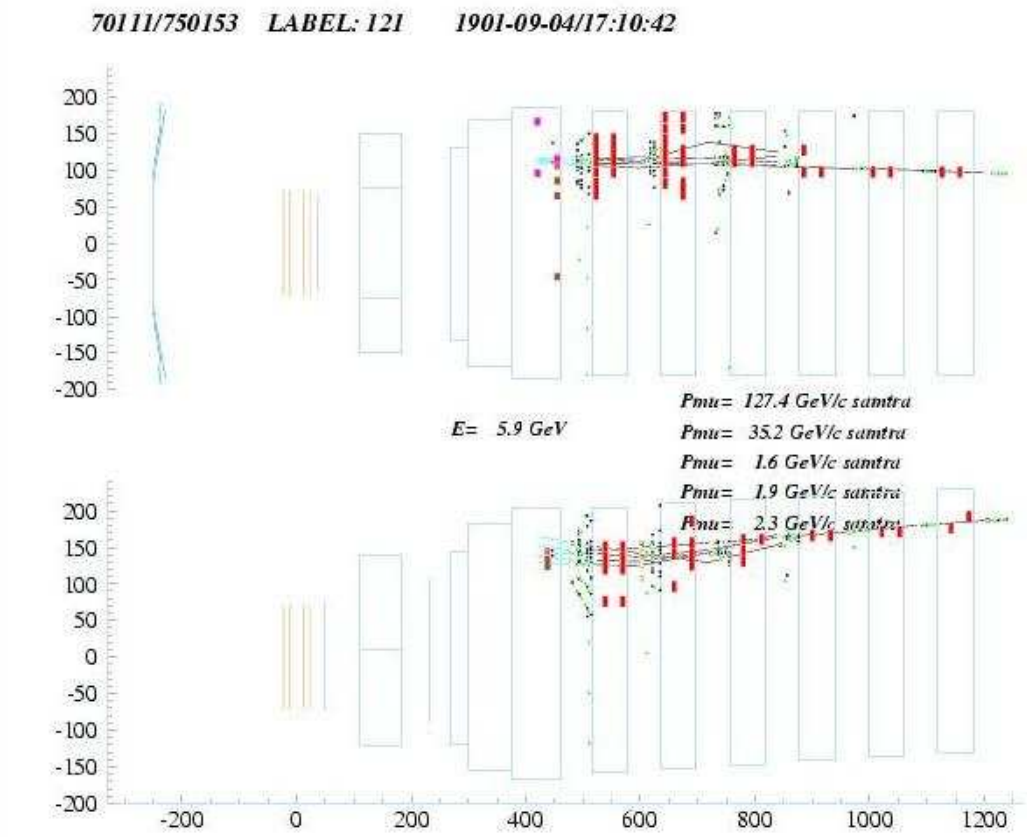

Figure 3.2: A high shower leakage event. There are many hits in the spectrometer which is causing false μ resconstruction and an error in the momentum. 5 μ's have been found.

reconstruction efficiency described in earlier study [4]. The reconstruction efficiency for the third plane with 30-40 GeV E_{had} has been shown in the figure 3.3. The average efficiency is about 99% for $p_\mu > 20$GeV mostly because of the low hadronic activity in spectrometer.

The RE for the 8th calorimeter plane has been shown in figure 3.4. The average efficiency is between 95% to 99% for $p_\mu > 40$GeV. This decrease in the efficiency is due to leakage to the spectrometer. Broken line behavior in the figure 3.4 is because of low statistics with high E_{had} events. In both figures there is a sharp decrease in

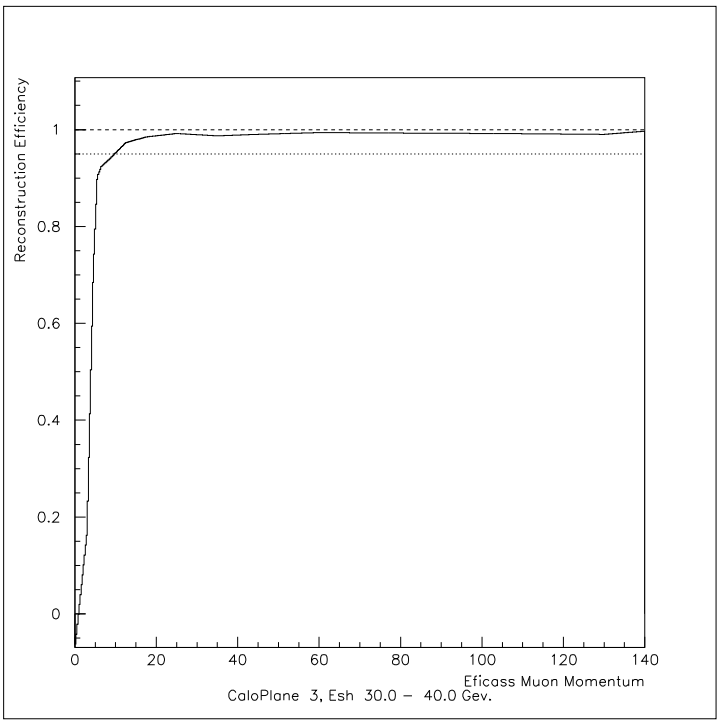

Figure 3.3: Reconstruction efficiency of the detector for the events in third calorimeter plane for low hadronic activity. Efficiency is about 99% for the $p_\mu > 20$GeV.

the efficiency in the low p_μ region. This is because that the low energetic μ can not be able to satisfy the conditions to be labeled as reconstructed. It may stop in the spectrometer or scatter out of it.

3.1.2 Momentum Resolution

Momentum resolution defines how close is the reconstructed momentum to its true value. Momentum of the μ is determined from the curvature of the track. There is also another algorithm that finds the momentum from the range of the track if the μ stops in the spectrometer, but that algorithm is not used in this analysis. Very high momentum μ's leave almost a straight line track that makes curve fitting harder. On the other hand low momentum μ's may have problems with the track reconstruction that leads

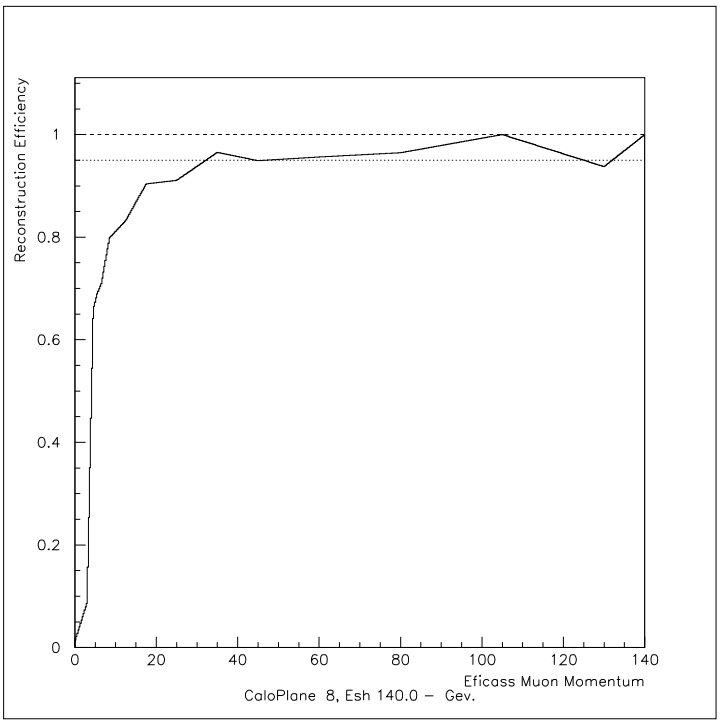

Figure 3.4: Reconstruction efficiency of the detector for the events in third calorimeter plane for low hadronic activity. Efficiency is about 95-97% for the $p_\mu > 40$GeV.

to problems in momentum determination. Also high activity in the spectrometer due to shower leakage degrades the momentum resolution.The definition of the good μ's with respect to the track properties also changes the momentum resolution.

Like the RE, momentum resolution(MR) is also a function of the x_{vtx}, E_{had} and p_μ(MR = MR(x_{vtx}, E_{had}, p_μ)). Also like RE, MR has been binned with respect to these variables. 12 bins in x_{vtx}, 1 bin for each plane, 9 bins in E_{had}, since the shower leakage is not as curicial as it is in the RE, and 14 bins in p_μ. Bins in E_{had} and p_μ are spaced with respect to the event density in the region. Then for each event resolution of the μ calculated by

$$\mathrm{MR} = \frac{p_{\mu_T}}{p_{\mu_R}} - 1$$

where p_{μ_T} is the true momentum of the muon and p_{μ_R} is the reconstructed value.

Figures 3.5 and 3.6 show the resolutions for different cases. In figure 3.5 p_μ is between 20 and 30 GeV and hadronic shower is small. As a result, resolution is a Gaussian distribution with very little non-Gaussian tail. In figure 3.6, on the other hand, $E_{had} \geq$ 90GeV, leading high leakage to the spectrometer, and high p_μ ($60 \leq p_\mu \leq 80$GeV) combination leading significant degradation in the MR.

3.2 Hadronic Shower

Properties of the hadronic shower is another important part of the structure function analysis. To measure the energy of the shower and the vertex plane of the event a Neural Network (NN) based technique has been developed [14, 15]. The NN has been used to perform a pattern recognition on the input signals in both cases. Both NN has two hidden layers, an input layer with 15 input nodes, 14 of which are for the pulse-heights of the planes of the calorimeter and the last one for the sum of the pulse-heights of the 8 scintillator planes. Vertex plane finding NN has an output layer with 25 output nodes, 4 for each EM plane, 20 for each half-plane in HAD1 and HAD2 regions of the calorimeter and the last one for representing spectrometer. The node with highest value has been taken as the vertex plane. The hadronic shower energy NN has a single output node in its output plane representing the shower energy.

3.2.1 Energy Resolution

The hadronic shower energy NN (NNEhad) has been trained and tested with two sets of CC Monte-Carlo (MC) events. The training set contains 84K events (6K for each plane) and test set has 196K events (14K for each plane). Energy resolution also has been parameterized as

$$\frac{\sigma_E}{E} = \frac{0.34 \pm 0.04}{\sqrt{E}} + 0.06 \pm 0.01$$

However, this parameterization is not good enough to be used in the MC. Non-Gaussian tails and the incomplete training of the NN over 50 GeV require the study of the energy resolution of the NN. The resolution of the NN (NNRes) is mostly affected from the

shower leakage, so NNRes is a function of x_{vtx} and E_{had}.

$$\text{NNRes} = \text{NNRes}(x_{vtx}, E_{had})$$

NNRes determined for each plane in 32 bins in E_{had} using the formula

$$\text{NNRes} = \frac{E_{had_{NN}} - E_{had_{True}}}{E_{had_{True}}}$$

NN is most efficient between 15 GeV to 70 GeV. Below 15 GeV NN slightly overestimates the E_{had} and above 70 GeV it underestimates the E_{had}. Figure 3.7 shows an example of the NN resolution in high energy domain. Function shows a non-Gaussian behavior on high energies. Figure 3.8 shows the resolution in low-mid energy region. Dashed lines show that resolution is very good in that region except for some very small non-Gaussian tail.

3.2.2 Event Vertex Reconstruction

The vertex finding NN (NNXvtx) is also trained with the 84K events (6K for each plane) and tested with 196K events (14K for each plane). It can find the true vertex plane with ± 1 plane 99% of the time. But a better study of the parameterizaton in the kinematical domain of this study is required. Vertex plane measurement depends on the calorimeter plane and the shower energy. The vertex finding efficiency of the NN,

$$\text{NNeff}(x_{vtx}, E_{had}) = \frac{X_{vtx_{True}} - X_{vtx_{NN}}}{\#\text{ of events in the bin}},$$

is calculated for each plane for 15 different E_{had} bins. As can be seen from the figures 3.9 and 3.10 efficiency of the NN degrades significantly on the planes at the boundaries of the parts of the calorimeter.

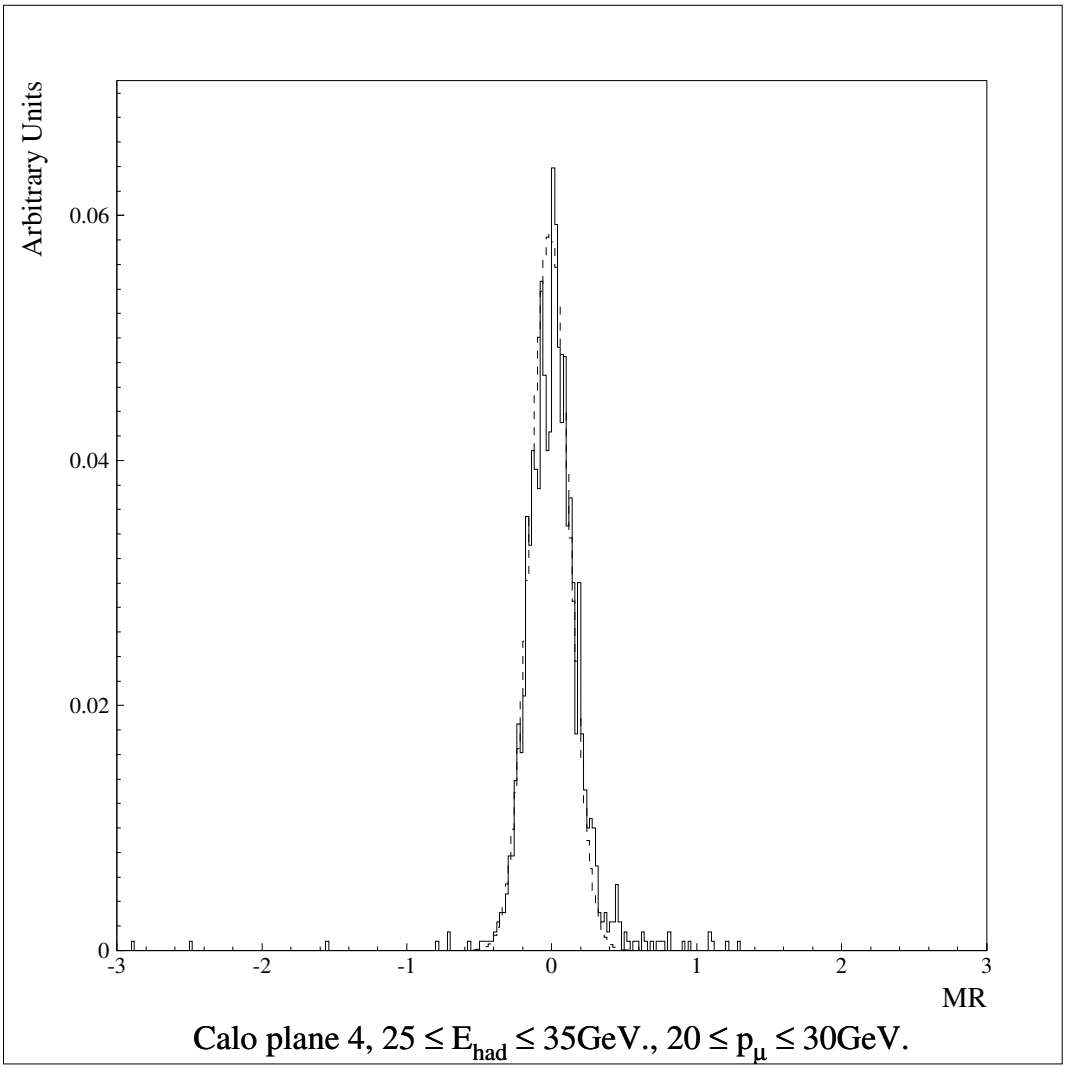

Figure 3.5: Momentum resolution of the detector for the events in the 4th calorimeter plane with the $25 \leq E_{had} \leq 35GeV$ and $20 \leq p_{\mu} \leq 30GeV$. The horizontal axis represents the value of MR. The dashed-line is a Gaussian fit.

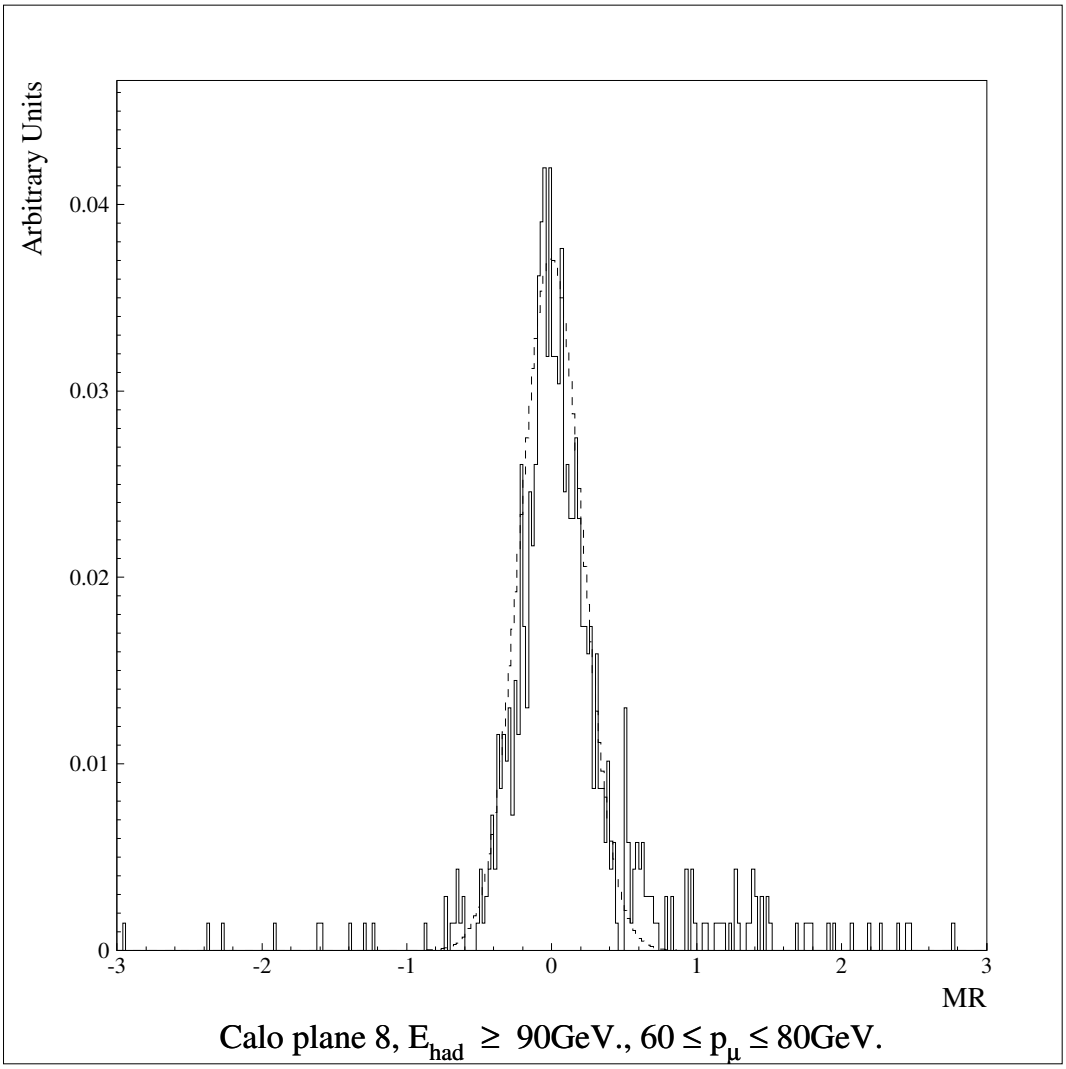

Figure 3.6: Momentum resolution of the detector for the events in the 8th calorimeter plane with the $E_{had} \geq 90$GeV and $60 \leq p_\mu \leq 80GeV$. The horizontal axis represents the value of MR. The dashed-line is a Gaussian fit.

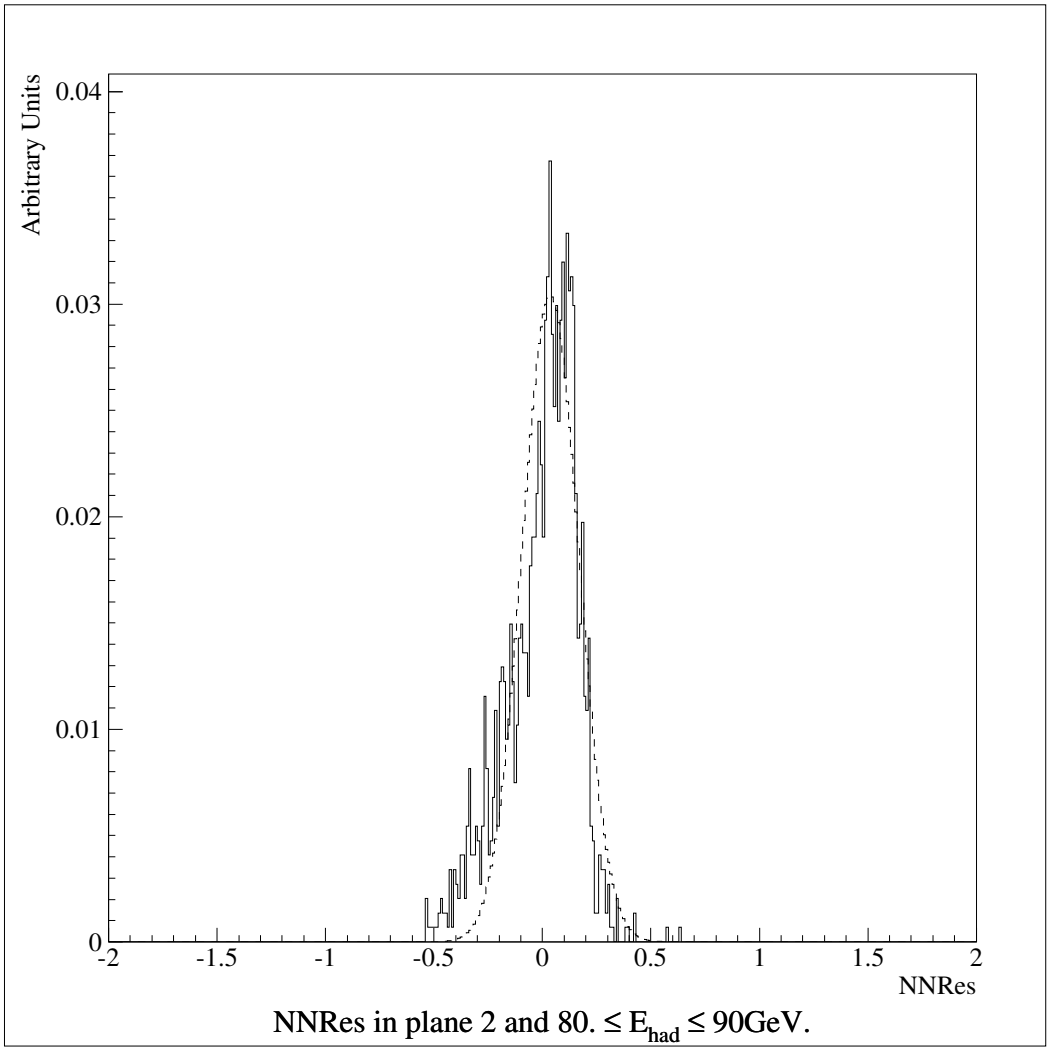

Figure 3.7: Energy resolution of the Neural Network based algorithm at plane 2. Horizontal axis is the value of the NNRes. Dashed lines are the Gaussian fit to the function.

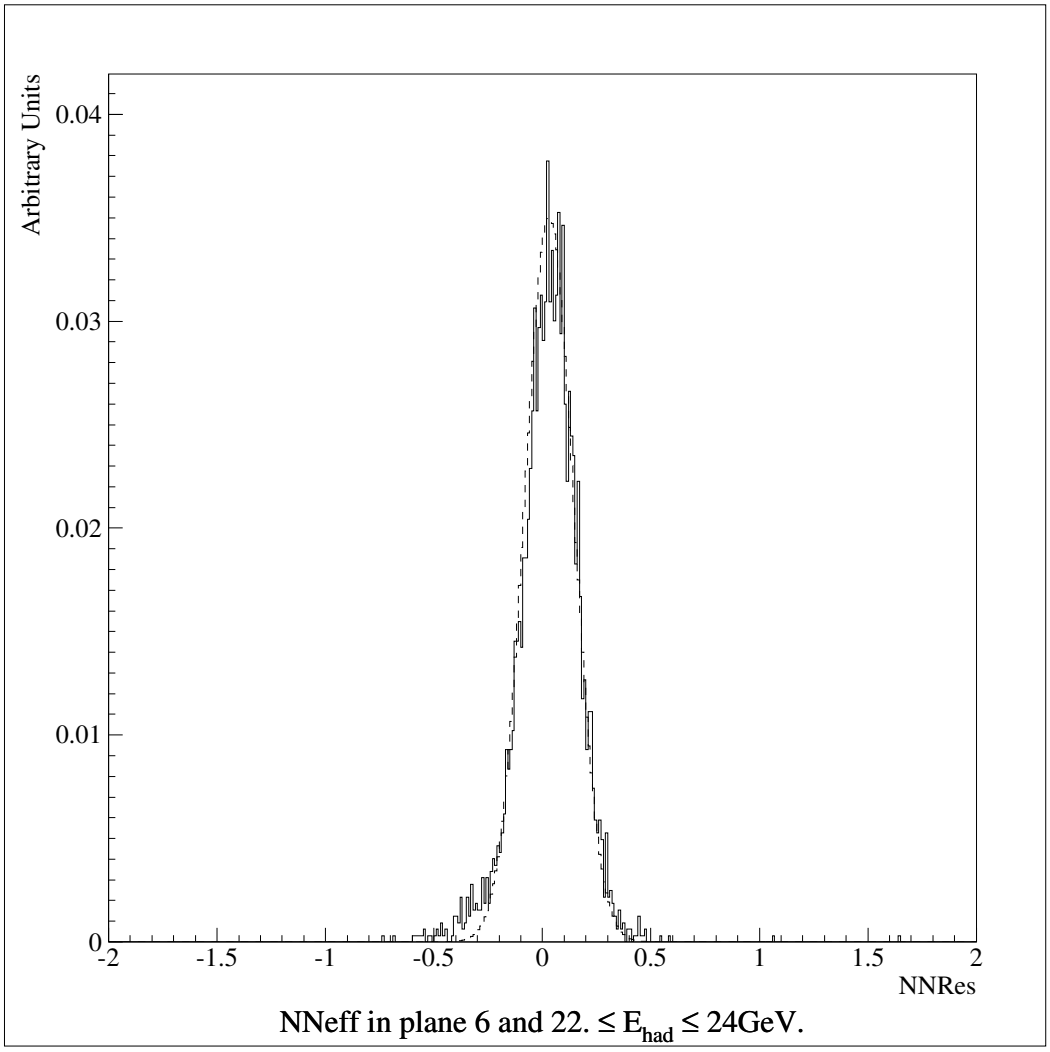

Figure 3.8: Energy resolution of the Neural Network based algorithm at plane 6. Horizontal axis is the value of the NNRes. Dashed lines are the Gaussian fit to the function.

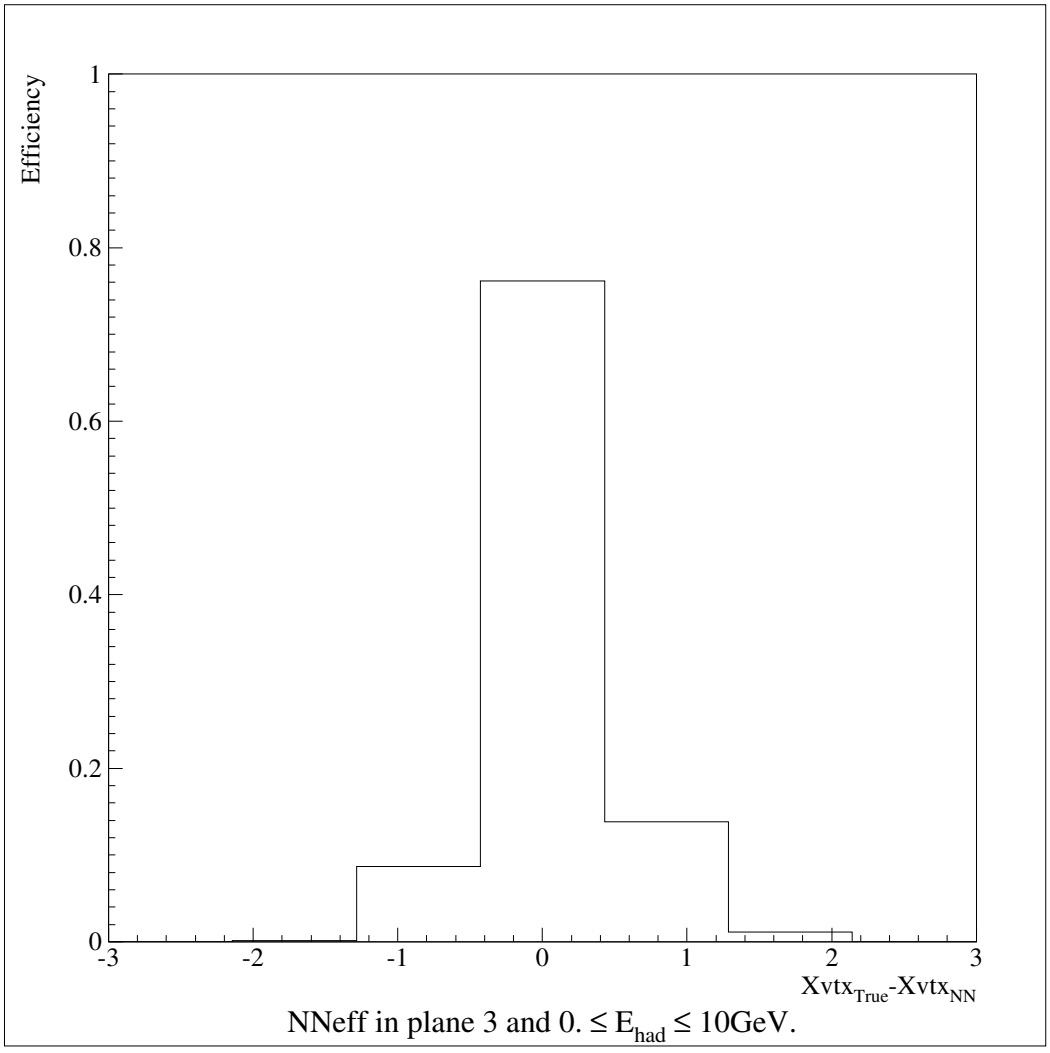

Figure 3.9: Vertex finding efficiency of the Neural Network based algorithm at plane 3. Horizontal axis is the difference between true vertex and the NN found vertex. − sign represents downstream plane.

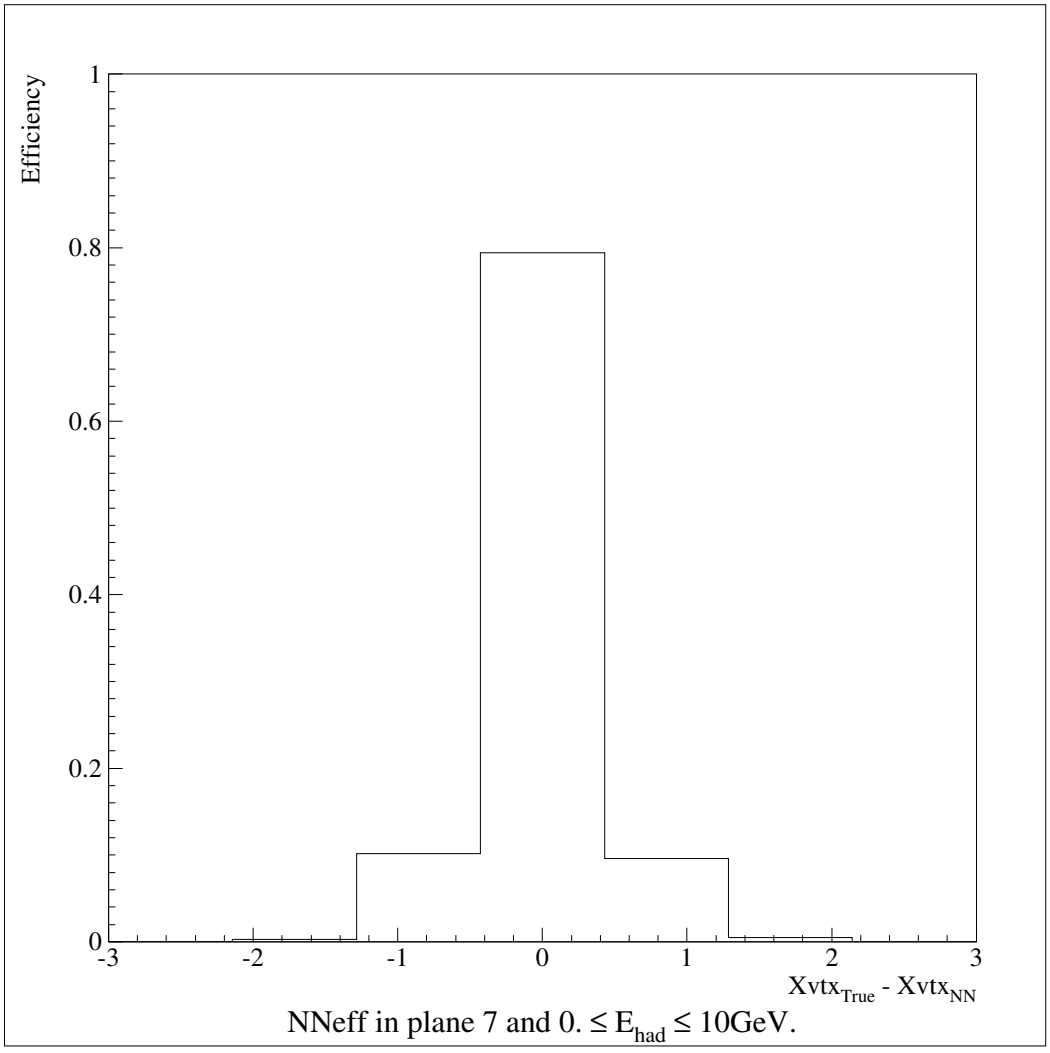

Figure 3.10: Vertex finding efficiency of the Neural Network based algorithm at plane 8. Low hadronic activity degrades efficiency Horizontal axis is the difference between true vertex and the NN found vertex. − sign represents downstream plane.

CHAPTER 4

MONTE-CARLO

CHORUS official Monte-Carlo EFICASS is very slow for creating the sufficient MC statistics for this analysis. In order to overcome this problem a new Monte-Carlo program (called Mickey) has been written. Mickey is a simple hit-and-miss type Monte-Carlo developed by Rolf Oldeman. It is several orders of magnitude faster than the EFICASS. As can be seen from the figure 4.1 Mickey needs 3 parameterizations to create a suitable sample, a beam flux model, a cross-section model and detector response parameterizations.

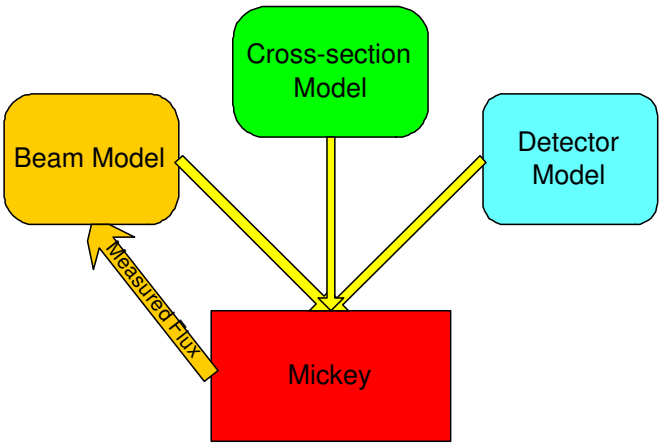

Figure 4.1: Basic diagram about Mickey

Detector response for the Mickey has been determined from the efficiencies found by the study of the EFICASS sample.

The beam model has been determined in two steps. First MC sample generated according to the GBEAM2000 simulation, fitted for parameters p to the function

$$\Phi(E) = \exp(p_1 - \frac{E}{p_2} - \frac{p_3}{E}) + \exp(p_4 - \frac{E}{p_5} - \frac{p_6}{E}) \tag{4.1}$$

which represents flux from pion decay and kaon decay. Then in the second step beam spectra is measured using the first MC sample and another MC sample set is created using the measured spectra, fit to the same function. GBEAM2000 simulation also has been used to determine the radial distribution function $f(E, r)$ of the beam which is normalized to 1 over the radial surface. Figure 4.2 shows the procedure followed in beam flux measurement.

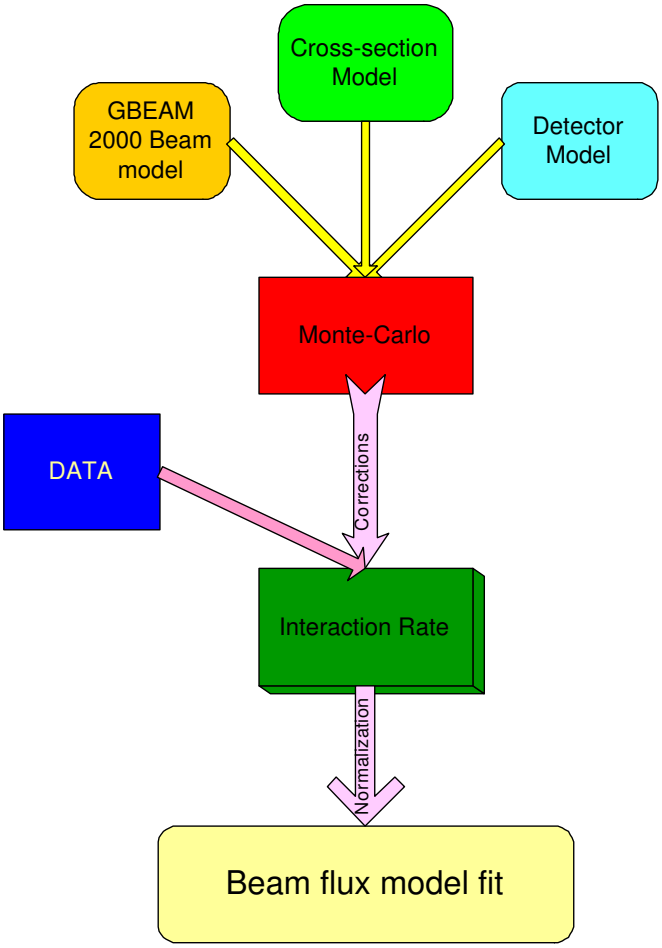

Figure 4.2: Beam flux model measurement procedure

The neutrino–nucleon and anti-neutrino–nucleon differential cross-sections have been

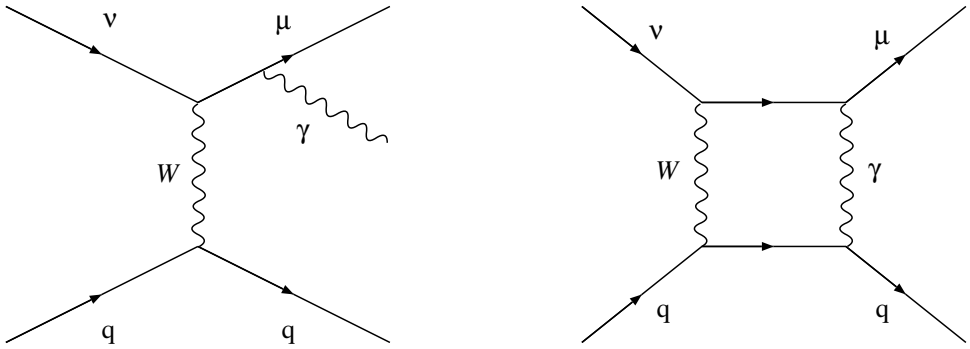

Figure 4.3: Diagrams of the radiative corrections considered in the scheme of Bardin.

calculated using equations

$$2xF_1^{\nu} = 2(d + \overline{u} + s + \overline{c}), \tag{4.2}$$

$$2xF_1^{\overline{\nu}} = 2(\overline{d} + u + \overline{s} + c), \tag{4.3}$$

$$F_2^{\nu,\overline{\nu}} = 2xF_1^{\nu,\overline{\nu}} \frac{1+R}{1+4M_N^2x^2/Q^2}, \tag{4.4}$$

$$xF_3^{\nu} = 2(d - \overline{u} + s - \overline{c}), \tag{4.5}$$

$$xF_3^{\overline{\nu}} = 2(-\overline{d} + u - \overline{s} + c). \tag{4.6}$$

for GRV98 [16] parton distributions. The parameterization of $R(x, Q^2)$ is taken from a fit to the world data [17]:

$$R(x,Q^2) = \frac{0.0635}{\ln(Q^2/0.2^2)}\theta(x,Q^2) + \frac{0.5747}{Q^2} - \frac{0.3534}{Q^4 + 0.3^2}, \tag{4.7}$$

with

$$\theta(x,Q^2) = 1 + 12\frac{Q^2}{Q^2+1} \cdot \frac{0.125^2}{0.125^2 + x^2}, \tag{4.8}$$

where Q^2 is expressed in GeV^2. This parameterization is based on measurements of R with Q^2 larger than 1.0 GeV^2. For lower values of Q^2, R is assumed to be constant.

The effects of the radiative processes to the cross-section have been calculated according to the [18] using the GRV98 parton distribution functions. The figure 4.3 shows the Feynman diagrams of the radiative processes taken into the consideration.

Following the algorithm below, an event has been generated.

- The position of the interaction vertex is generated randomly according to a uniform probability distribution in a fixed volume. This volume corresponds to the fiducial volume used in the analysis, enlarged transversally by 20 cm and longitudinally by one plane, to allow smearing into the fiducial volume.

- The density of the detector at the generated vertex position is compared to a random number, generated uniformly between zero and the maximum density of the calorimeter. If the density is smaller than this number, the event is rejected and the procedure is restarted.

- The neutrino type is generated, with an equal chance to generate a neutrino or an anti-neutrino and the energy of the neutrino is generated according to a uniform distribution between 5 and 300 GeV.

- The beam flux at the generated neutrino energy is compared to a random number generated uniformly between zero and the maximum value of the beam flux. If the flux is smaller than this number, the event is rejected and the procedure is restarted.

- The radial vertex function $f(E, r)$ is compared to a random number generated uniformly between zero and the maximum value of the radial function. If the radial function is smaller than this number, the event is rejected and the procedure is restarted.

- The kinematic variables x and y are generated uniformly between 0 and 1.

- The differential cross-section is compared to a random number generated uniformly between zero and the maximum value of the differential cross-section. If the differential cross-section is smaller than this number, the event is rejected and the procedure is restarted.

The generated event then passed through the calorimeter and spectrometer simulation to create the data set to be used in analysis. Muon propagation through the calorimeter and spectrometer has been done considering energy loss, multiple scattering and

magnetic bending. The simulation is composed of the tracking the muon in calorimeter and spectrometer and the calculation of the resolutions of the p_μ and the E_{had}.

Energy loss of the muon has been calculated plane-by-plane using the Bethe-Bloch equation:

$$-\left.\frac{dE}{dx}\right|_{ion} = K\frac{Z}{A}\frac{1}{\beta^2}\left[\frac{1}{2}\ln\frac{2m_e c^2\beta^2\gamma^2 T_{max}}{I^2} - \beta^2 - \frac{\delta}{2}\right], \tag{4.9}$$

where $K = \frac{N_A e^4}{4\pi\epsilon_0^2 m_e c^2} = 0.307$ MeVg^{-1}cm^2, Z and A the atomic number and the atomic mass of the traversed medium, m_e the electron mass, T_{max} the maximum transferable energy to an electron, I the mean excitation energy of the atom and $\delta/2$ a correction for the density effect. The mean excitation energy is taken from Ref [19], which calculates 286 eV for iron and 823 eV for lead.

The multiple scattering of the μ is taken into the consideration with respect to the following equation

$$\theta_0 = \frac{13.6\,\text{mrad}}{p_\mu/\text{GeV}}\sqrt{x/x_0}, \tag{4.10}$$

where x is the thickness of the plane and x_0 the radiation length of the traversed material. Following Ref [20], the spread of θ_0 has been increased by a factor $[1 + 0.038\ln(x/x_0)]$ where x is now the thickness of the whole calorimeter or spectrometer, and the multiple scattering angle in lead is increased by another 8%, and in iron by 3%.

Bending of the muon in the spectrometer is taken into account considering constant 1.7 Tesla magnetic field.

For the muon reconstruction efficiency of the detector the RE function described in section 3.1.1 has been used.

The momentum resolution of the muon in the spectormeter has been done according to the MR function described in the section 3.1.2.

The hadronic shower resolution in the calorimeter calculated by the NNRes function described in the section 3.2.1.

Event vertex has been determined by the NNeff function described in the section 3.2.2.

The direction resolution of the muon has been described with the parameterization $[0.8 + 15\,\mathrm{GeV}/p_\mu]$mrad for each projection. The direction resolution of the muon spectrometer has been degraded by a factor 5 for 15% of the events to take Non-Gaussian tails in the direction resolution which have been observed in the simulations.

4.1 Efficiency of the Parameterizations

Some tests have been done to see the accuracy of the parameterizations described in the sections 3.1 and 3.2. Tests have been done with EFICASS generated MC sample. MC truth information is fed into the appropriate smearing function and compared with the reconstructed values of the EFICASS values. Figure 4.4 shows the result of the smearing on low and mid-energy regions. It can clearly be seen that smearing function performs very well. The ratio of the MR function over EFICASS reconstructed has

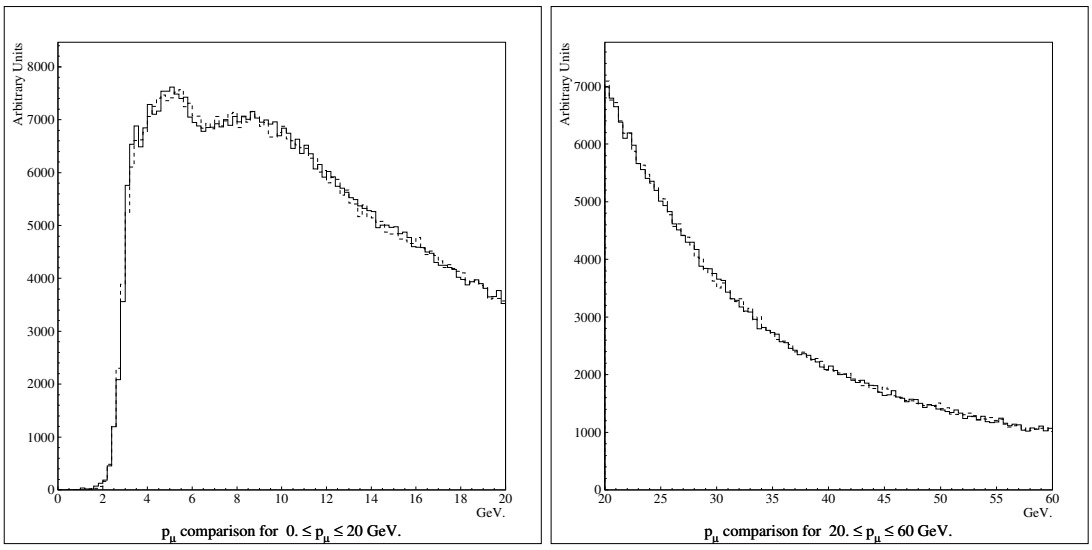

Figure 4.4: Comparison of p_μ in two different regions. Left figure shows the low-energy region. Right figure shows mid-energy region. Solid lines are for EFICASS values, dashed lines are for the values smeared with MR function.

been given in figure 4.5. The ratio figures shows that p_μ is represented with better than 95% efficiency in the region $5 \leq p_\mu \leq 100$GeV.

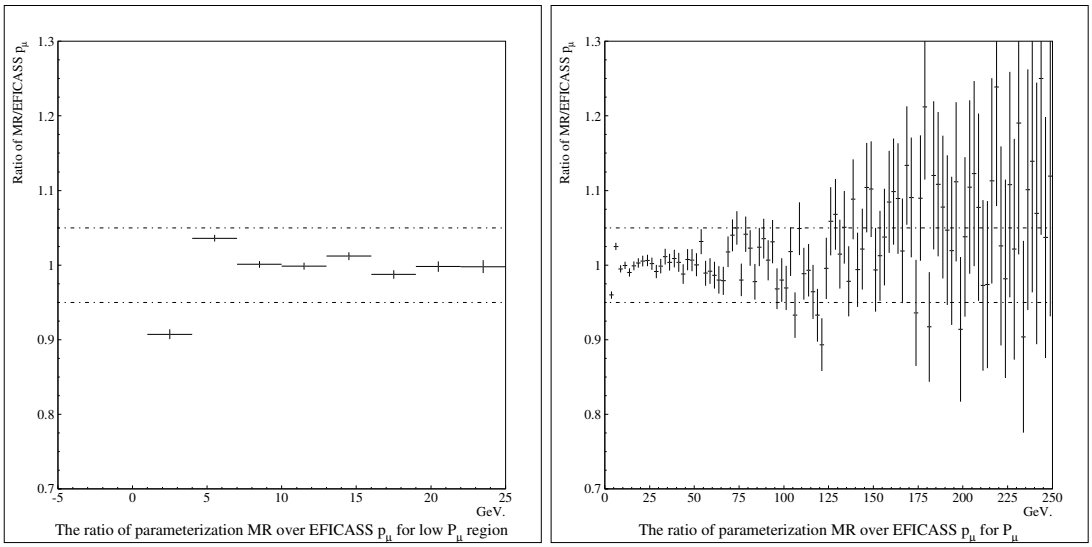

Figure 4.5: The ratio of the MR function over EFICASS reconstructed value for p_μ. Figure on the left is for low-energy region. Figure on the right is for full energy region. Dashed lines marks the 5% region.

The efficiency of the NNRes is given in the figure 4.6. According to the figure 4.6, NNRes function is also in a very good agreement with EFICASS smeared values. The ratio of the two histograms has been given in figure 4.7. Except from the boundaries of the histogram, NNRes simulates EFICASS smeared values with better than 97.5% accuracy in low-energy region and 95% accuracy in full energy region. The figure 4.8 shows that NNeff function also simulates EFICASS smearing accurately.

4.2 Efficiency of Monte-Carlo

To check the assumptions in the Mickey, similarities between the Mickey and data have been examined. The comparisons of the main obsevables p_μ, E_{had} and θ_μ have been

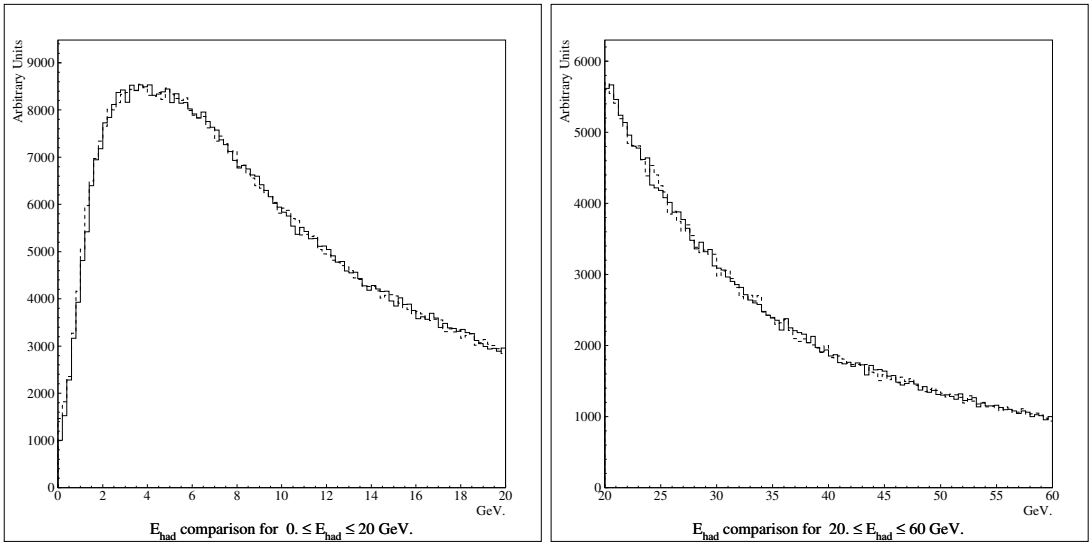

Figure 4.6: Comparison of E_{had} in two different regions. Left figure shows the low-energy region. Right figure shows mid-energy region. Solid lines are for EFICASS values, dashed lines are for the values smeared with MR function.

given in figures 4.9, 4.10 and 4.11 respectively. The figures show that the assumptions in Mickey is accurate enough.

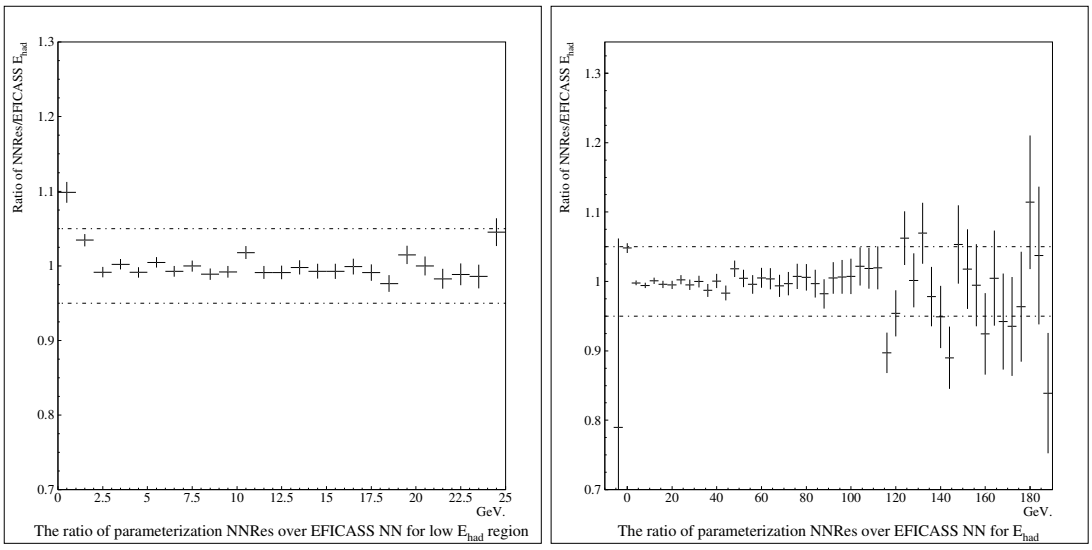

Figure 4.7: The ratio of the NNRes function over EFICASS reconstructed value for E_{had}. Figure on the left is for low-energy region. Figure on the right is for full energy region. Dashed lines marks the 5% region.

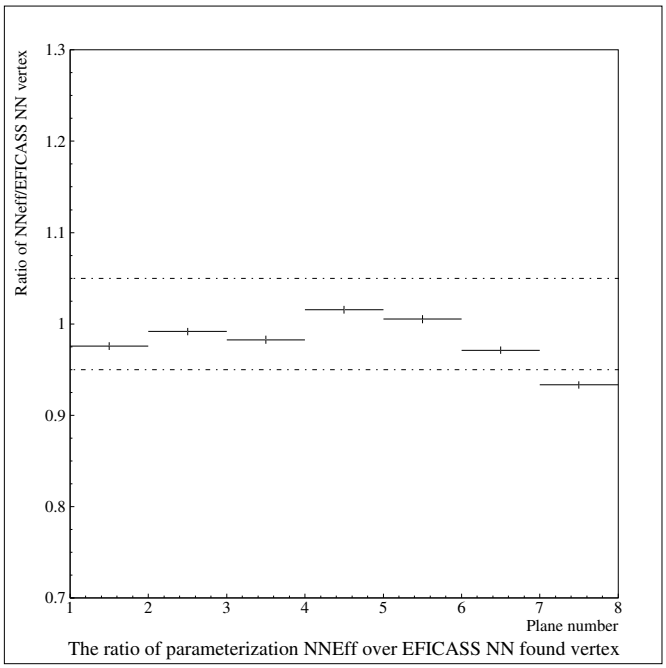

Figure 4.8: The ratio of the NNeff function over EFICASS reconstructed value for the event vertex. Dashed lines mark the 5% region.

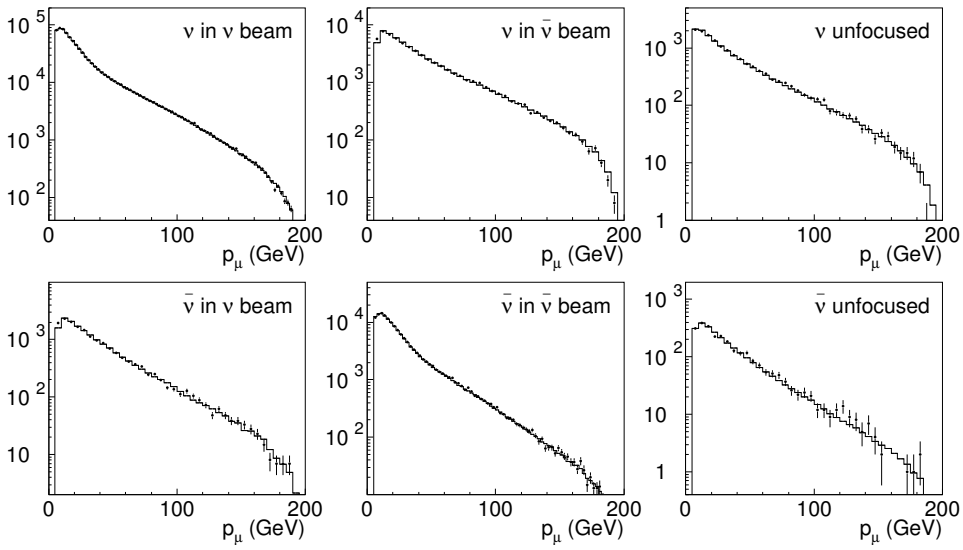

Figure 4.9: Comparison between data (points) and MC (histogram) of the muon momentum distributions of neutrino and anti-neutrino events in the three beam modes.

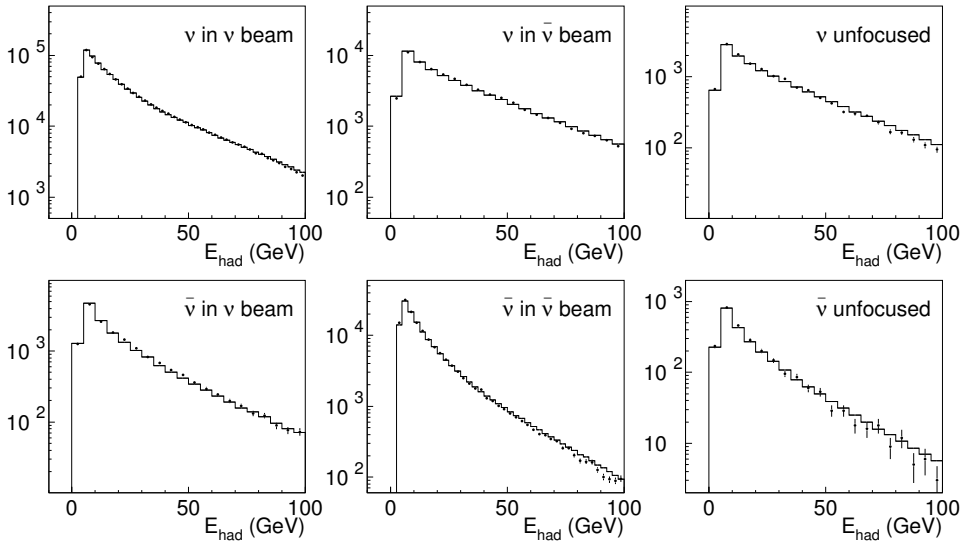

Figure 4.10: Comparison between data (points) and MC (histogram) of the hadronic energy distributions of neutrino and anti-neutrino events in the three beam modes.

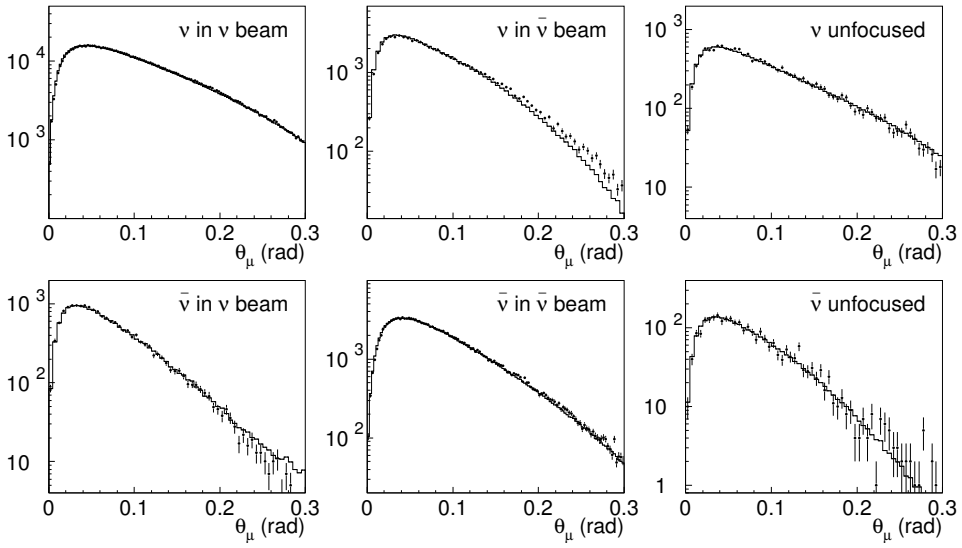

Figure 4.11: Comparison between data (points) and MC (histogram) of the muon angle distributions with respect to the central beam-line of neutrino and anti-neutrino events in the three beam modes.

CHAPTER 5

DATA ANALYSIS

The data has been used for two measurements, beam flux measurement and cross-section measurement. The data for the ν, $\bar{\nu}$ and unfocused beam modes have been used for beam flux measurement. On the other hand only the main components of the ν and $\bar{\nu}$ beam modes have been used for cross-section measurement. The structure function analysis is based on the cross-section measurement.

5.1 Beam Flux Measurement

The neutrino cross-section is approximately proportional to the neutrino energy E, the energy spectrum of neutrino interactions is directly related to the energy weighted beam spectrum.

The normalization is chosen such that the energy weighted beam flux corresponds to the rate of interactions on an isoscalar target with surface density of 1 ton m^{-2} [4]. The interaction rate $\Phi(E)$ is then related to the unweighted neutrino flux $\phi(E)$ in the following way:

$$\Phi(E) = N_A \sigma_0^{\nu,\overline{\nu}N} E\phi(E), \tag{5.1}$$

where N_A is Avogadro's number and σ_0 is the ratio of total neutrino-nucleon cross-section and the neutrino energy. Its values are taken from Ref [3]:

$$\sigma_0^{\nu N} = 0.677 \cdot 10^{-38}\mathrm{cm}^2\mathrm{GeV}^{-1}, \tag{5.2}$$

$$\sigma_0^{\overline{\nu}N} = 0.500 \cdot \sigma_0^{\nu N}. \tag{5.3}$$

The interaction rate is determined from the number of events in bins of different energy $N(E_i)$, corrected for detector acceptance and resolution, and normalized to the bin size ΔE_i, the surface density ρ, and number of protons on target N_{pot}:

$$\Phi(E) = \frac{N(E_i)}{N_{pot}\Delta E_i \rho}. \tag{5.4}$$

Table 5.1: Event numbers obtained for the beam flux and cross-section analysis.

	ν beam		$\overline{\nu}$ beam		unfocused	
run selection	3,631,976		1,031,741		92,765	
beam on	3,616,621		1,020,460		91,483	
no read-out error	3,581,646		1,017,134		91,303	
horn and reflector on	3,579,599		1,013,845		91,303	
no overlay muon	3,538,163		998,227		90,367	
reconstructed muon	3,105,332		859,309		75,250	
x_{vtx} in plane 2-7	1,857,352		523,609		44,928	
$-90 \leq y_{vtx}, z^*_{vtx} \leq 90$ cm	1,252,289		335,927		24,477	
	ν	$\overline{\nu}$	ν	$\overline{\nu}$	ν	$\overline{\nu}$
right sign muon	1,224,051	37,638	83,769	252,158	20,044	4,433
$p_\mu \geq 5(6)$ GeV	1,161,238	26,888	80,695	243,317	19,039	4,338
$4 \leq E_{had} \leq 100$ GeV	898,522	26,379	64,538	147,410	15,051	2,627
$\theta_\mu \leq 300$ mrad	882,132	26,060	64,348	146,650	14,834	2,625
$10 \leq E_\nu \leq 200$ GeV	870,252	24,316	62,005	145,816	14,440	2,582

The table 5.1 shows the number of events used for the beam flux and cross-section and measurement.

5.1.1 Corrections

To obtain the interaction rate $\Phi(E)$, the raw number of events in each bin, $N_{raw}(E_i)$, is corrected for the cuts, the muon reconstruction inefficiency and the detector resolution. In addition, corrections are applied for the non-isoscalarity of the target material, and for bin-centering.

The corrections for the cuts, the muon reconstruction inefficiency, and the detector resolution are calculated using a MC sample, by evaluating, for each bin, the ratio of the number of generated events (MC^G) to the number of reconstructed events (MC^R). This ratio is composed of three parts:

$$\frac{N_{cor}(E_i)}{N_{raw}(E_i)} = \frac{MC^G}{MC^R} = \frac{MC^G_{no\,cuts}}{MC^G_{cuts}} \cdot \frac{MC^G_{cuts}}{MC^G_{cuts,muon}} \cdot \frac{MC^G_{cuts,muon}}{MC^R_{cuts,muon}}. \tag{5.5}$$

The $\frac{MC^G_{no\,cuts}}{MC^G_{cuts}}$ is the ratio between the number of MC events before and after applying the cuts on the true values of the muon momentum, the hadronic energy and the

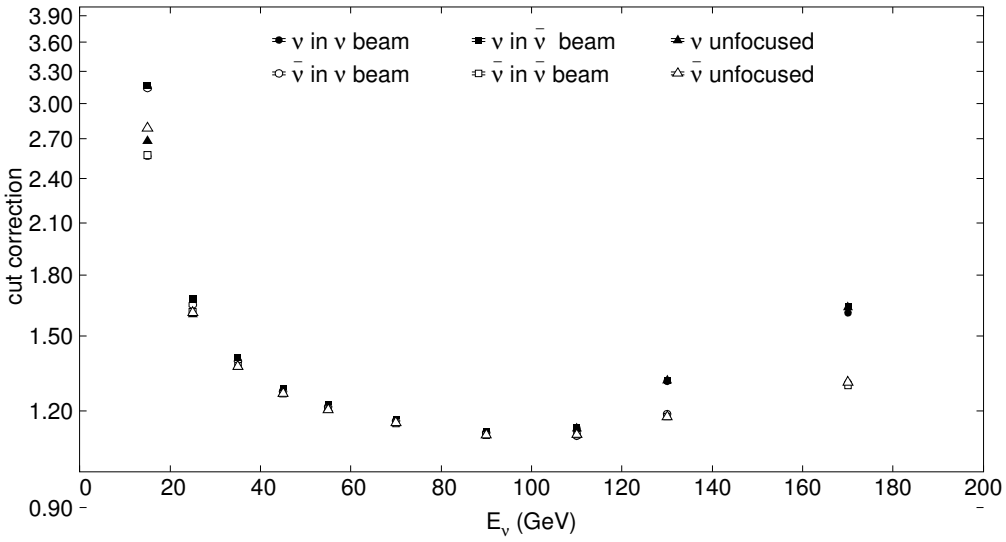

Figure 5.1: Correction factors for the kinematic cuts as a function of the neutrino energy.

muon angle. This correction factor is shown in Figure 5.1 as a function of the neutrino energy.

The $\frac{MC^G_{cuts}}{MC^G_{cuts,muon}}$ is the ratio between all events that satisfy the cuts on true values to those that also have a reconstructed muon. This correction factor is shown in Figure 5.2 as a function of the neutrino energy. A large fraction of the low energy muons that are defocused by the spectrometer magnets leave the detector before traversing all magnets. Also only use of curve fitting algorithms significantly reduces the amount of reconstructed events. Hence, the correction factor is the largest for the contamination components at low neutrino energy.

The $\frac{MC^G_{cuts,muon}}{MC^R_{cuts,muon}}$ takes into account the detector resolution. This correction is the ratio between the number of MC events with the cuts and the binning evaluated using the true values to the number of events with the same cuts and binning evaluated using the smeared values. The correction values are shown in Figure 5.3 as a function of the neutrino energy. It is generally below 5% for beam type muons. For contamination

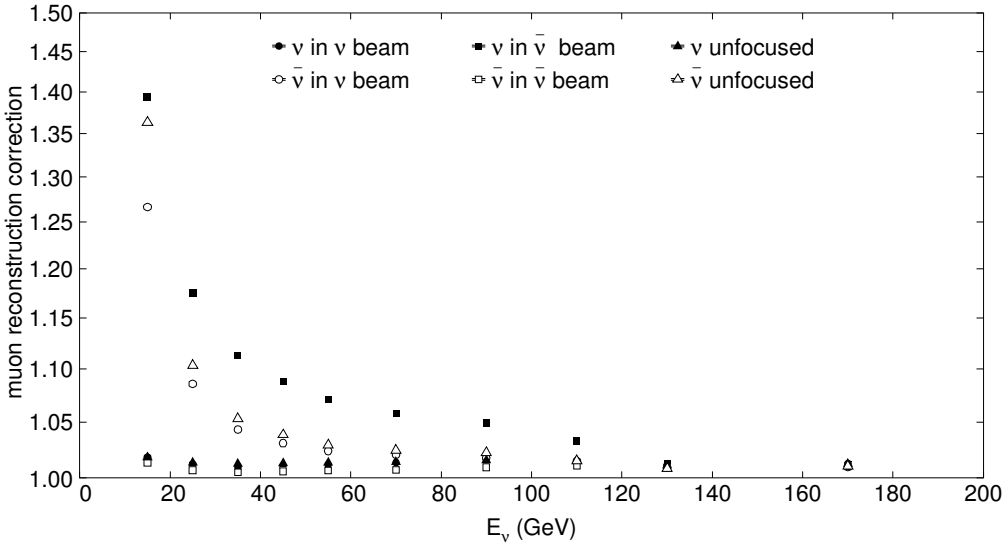

Figure 5.2: Correction factors for muon reconstruction inefficiency as a function of the neutrino energy.

muons it ranges from about 10% to 30% at high neutrino energy.

Isoscalarity and bin-center corrections are applied according to reference [4], are shown in the figures 5.4 and 5.5

After all the corrections applied, resulting beam spectra for ν, $\bar{\nu}$ and unfocused modes with GBEAM simulation and fits to the function 4.1 has been given in figures 5.6 and 5.7. The ratio of the GBEAM and measured spectra for interaction rate and average energy has been given in figure 5.8

5.2 Cross-section

The differential cross-section is determined for only the focused components of the beam modes for the events

- without hardware errors, *i.e.* no problem in the run, beam is on, focusing is working, no errors in read-out etc.

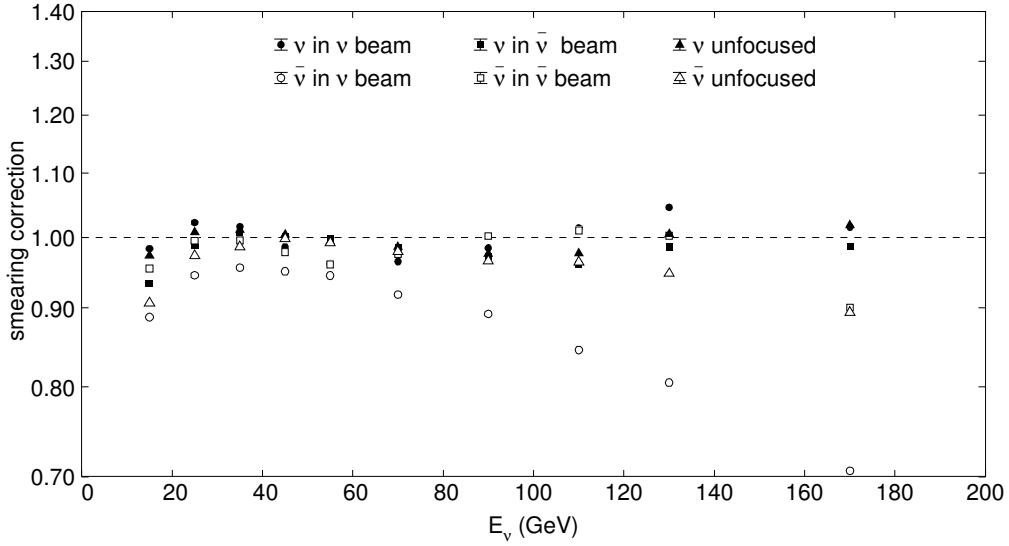

Figure 5.3: Correction factors for smearing as a function of the neutrino energy.

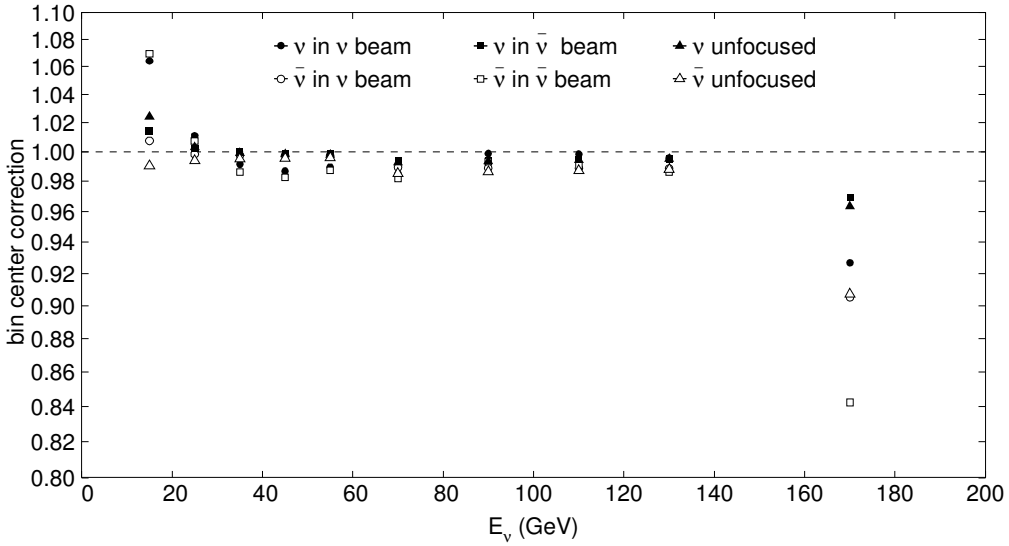

Figure 5.4: Correction factors for the bin-centering as a function of the neutrino energy.

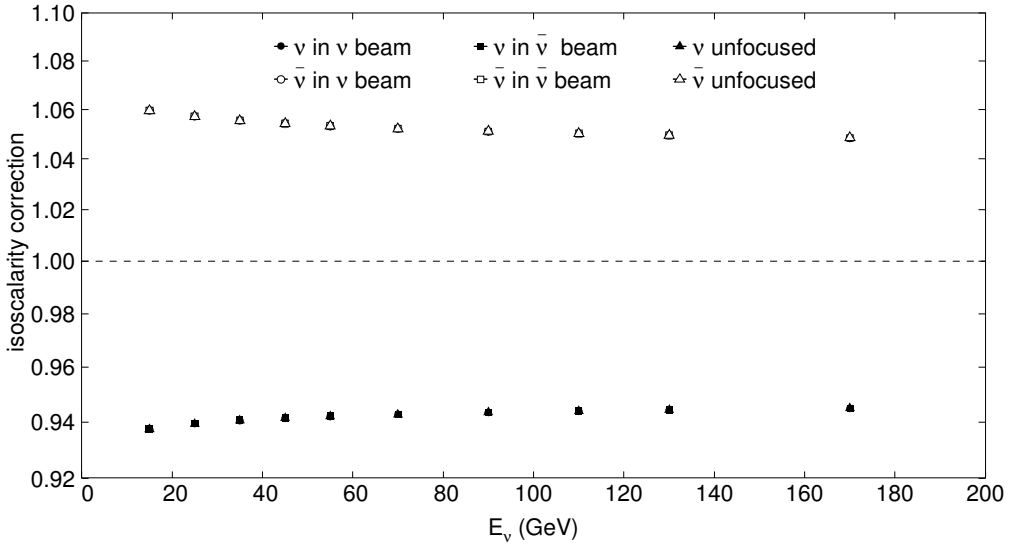

Figure 5.5: Correction factors for the non-isoscalarity of the target as a function of the neutrino energy.

- with at least one muon reconstructed using curve-fitting algoritms with the correct sign, $p_\mu \geq 5$GeV, satisfying the requirements of at least 5 magnet and 7 scintillator hits in both transverse directions,
- event vertex determined as in the fuidical volume of 2^{nd} to 7^{th} planes in beam direction and $-90 \leq y_{vtx}, z_{vtx} \leq 90\,cm$,
- with $4 \leq E_{had} \leq 100\,\text{GeV}$
- with $\theta_\mu \leq 300\,\text{mrad}$
- and $10 \leq E_\nu \leq 200\,\text{GeV}$.

The events satisfying above criterias have been binned in a 3-dimensional histogram $N(E_i, x_j, y_k)$. Then the $N(E_i, x_j, y_k)$ is expected to be proportional to the

$$N(E_i, x_j, y_k) \propto \int_{E_i^{min}}^{E_i^{max}} dE \int_{x_j^{min}}^{x_j^{max}} dx \int_{y_k^{min}}^{y_k^{max}} dy \frac{1}{E} \frac{d^2\sigma}{dxdy}(E, x, y) \cdot \Phi(E), \qquad (5.6)$$

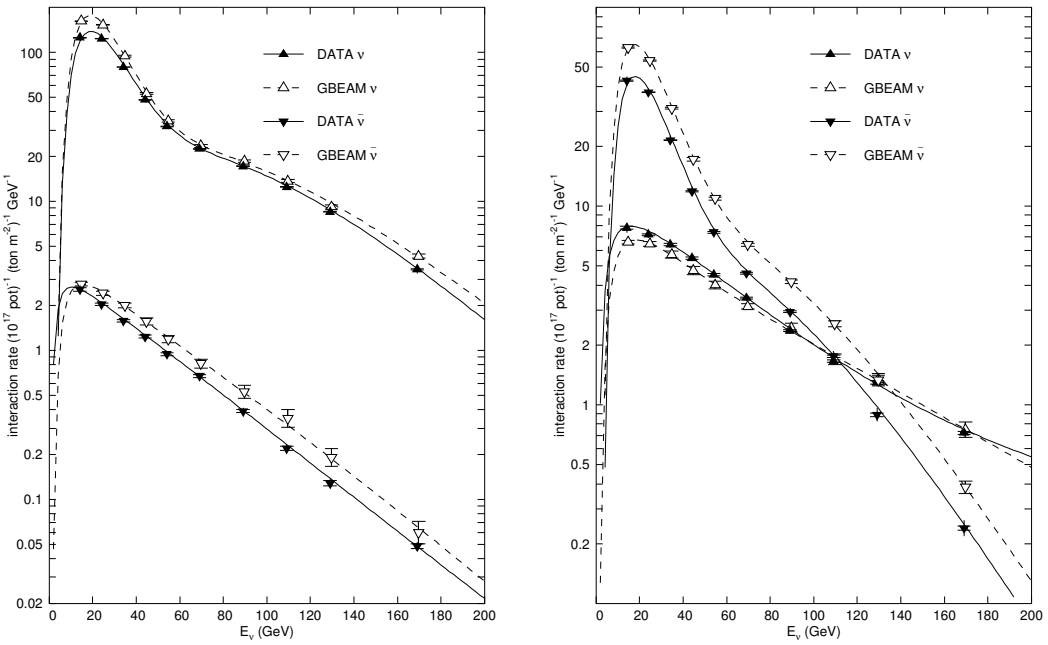

Figure 5.6: Measured and simulated beam spectra. Neutrino beam mode is on the left. Anti-neutrino beam mode is on the right.

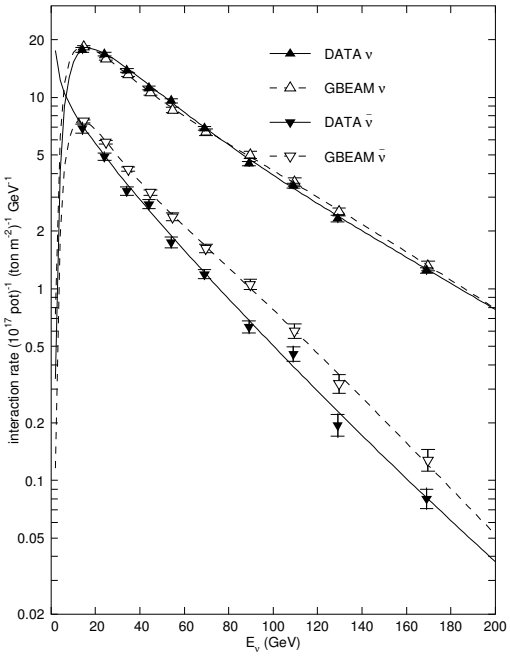

Figure 5.7: Measured and simulated beam spectra in unfocused beam mode.

where $\Phi(E)$ is the energy weighted beam spectrum. The neutrino flux and energy spectrum are not known with sufficient precision to measure the absolute cross-section. Therefore, the data are normalized to the total cross-section $\sigma_{tot}(E)$. For this, the data are also binned in a 1-dimensional histogram $N(E_i)$. The expected number of events in an energy-bin is:

$$N(E_i) \propto \int_{E_i^{min}}^{E_i^{max}} dE \frac{\sigma_{tot}(E)}{E} \cdot \Phi(E). \tag{5.7}$$

The differential cross-section is then determined by the ratio of events $N(E_i, x_j, y_k)$ to the total number of neutrino interactions in the same energy bin:

$$\frac{1}{E}\frac{d^2\sigma}{dxdy} = \frac{\sigma_{tot}}{E}\frac{N(E_i, x_j, y_k)}{N(E_i)\Delta x_j \Delta y_k}, \tag{5.8}$$

where Δx_j and Δy_j are the sizes of the bins in x and y respectively. The quantities $N(E_i, x_j, y_k)$ and $N(E_i)$ are corrected for resolution smearing and for the variation of the cross-section and beam flux within the bins.

Tables 5.2, 5.3 and 5.4 show the bin boundaries and the corresponding number of events in that bin for E, y, x.

The bins in the kinematical domain that is determined by the cuts on p_μ, θ_μ, and E_{had} have been shown in the figure 5.9.

5.2.1 Corrections

Like beam-flux, corrections for smearing effects, acceptance and cuts have been found using MC sample by

$$\frac{N_{cor}(E_i, x_j, y_k)}{N_{raw}(E_i, x_j, y_k)} = \frac{MC^G(E_i, x_j, y_k)}{MC^R(E_i, x_j, y_k)}, \tag{5.9}$$

where $MC^G(E_i, x_j, y_k)$ is the number of events generated in the bin and $MC^R(E_i, x_j, y_k)$ is the number of events reconstructed in the bin. Also bin-center corrections are applied according to [4]

$$\frac{N_{cen}(E_i, x_j, y_k)}{N_{cor}(E_i, x_j, y_k)} = \frac{\Phi(\langle E_i \rangle) \frac{1}{\langle E_i \rangle} \frac{d^2\sigma}{dxdy}(\langle E_i \rangle, \langle x_j \rangle, \langle y_k \rangle)}{\frac{1}{\Delta E_i \Delta x_j \Delta y_k} \int_{E_i^{min}}^{E_i^{max}} dE \int_{x_j^{min}}^{x_j^{max}} dx \int_{y_k^{min}}^{y_k^{max}} dy \; \Phi(E) \frac{1}{E} \frac{d^2\sigma}{dxdy}(E, x, y)}. \tag{5.10}$$

However after the corrections, measured and calculated differential cross-sections differ significantly. That difference might be attributed to unreliability of the parton distribution functions that has been used at low Q^2 and assumptions that has been made in model. This problem has been overcome by applying a phenomenological correction to the cross-section.

$$\rho(x, Q^2) = 0.93342 - 0.8203 \left(1 - \frac{x}{0.3468}\right) \cdot \frac{1}{1 + \frac{Q^2}{9.9310x}}. \tag{5.11}$$

Correction has been determined by fitting the function to the ratio of measured and calculated differential cross-section. The ratio of the measured and uncorrected cross-section and the correction function has been given in figure 5.10

After all corrections are applied, measured cross-sections have been presented in figure 5.11. Solid lines in the figure represent the cross-section model used in the MC. There is an agreement between measured values and theoretical values.

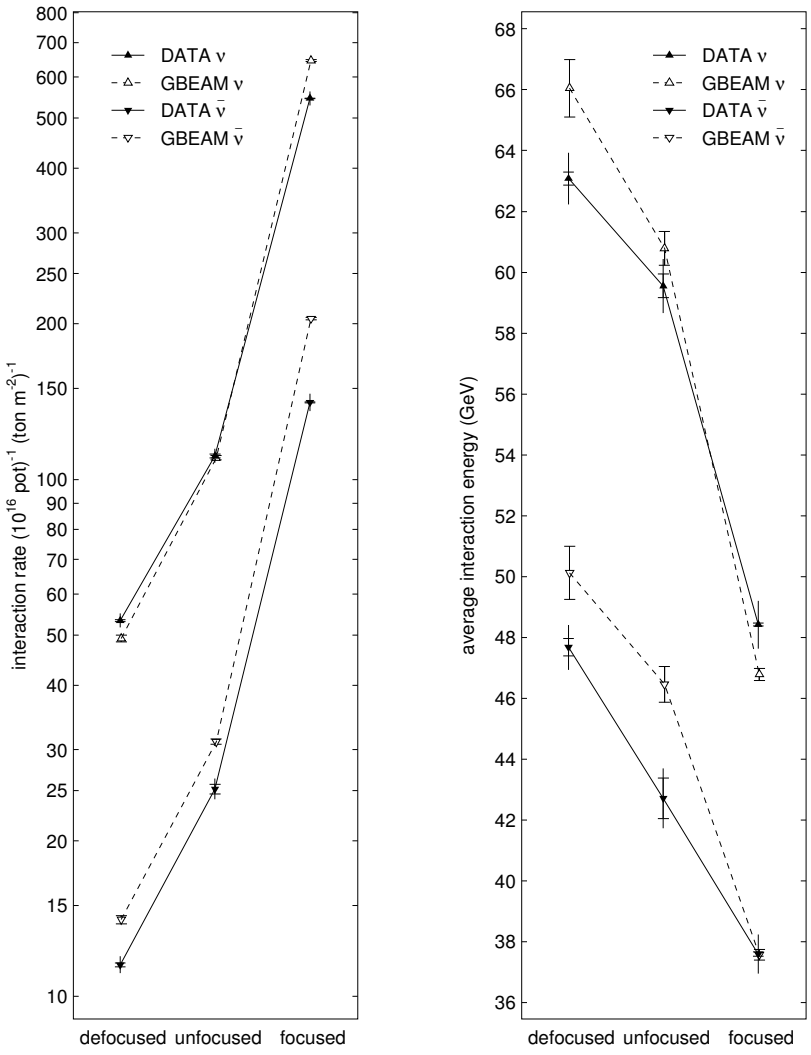

Figure 5.8: Comparison of integrated beam flux (left) and the average energy (right) between measurement and GBEAM.

Table 5.2: Binning in E.

E-range (GeV)	ν events	$\overline{\nu}$ events
10-20	0	0
20-30	127,184	25,557
30-40	107,737	20,800
40-50	75,561	12,318
50-60	52,766	7,694
60-80	75,091	9,620
80-100	64,119	7,574
100-120	40,099	4,220
120-140	23,072	1,996
140-200	21,482	1,657

Table 5.3: Binning in x.

x-range	ν events	$\overline{\nu}$ events
0.01-0.03	24,607	5,693
0.03-0.06	45,044	9,867
0.06-0.10	65,993	12,715
0.10-0.15	81,117	13,930
0.15-0.20	75,604	11,638
0.20-0.25	66,816	9,425
0.25-0.30	57,463	7,496
0.30-0.40	80,317	9,888
0.40-0.50	48,631	5,830
0.50-0.60	26,881	3,149
0.60-0.70	14,638	1,805

Table 5.4: Binning in y.

y-range	ν events	$\overline{\nu}$ events
0.05-0.15	22923	3,730
0.15-0.25	73447	15,984
0.25-0.35	101291	21,016
0.35-0.45	98381	16,901
0.45-0.55	92801	13,463
0.55-0.65	90256	10,395
0.65-0.75	75648	7,549
0.75-0.85	32364	2,398

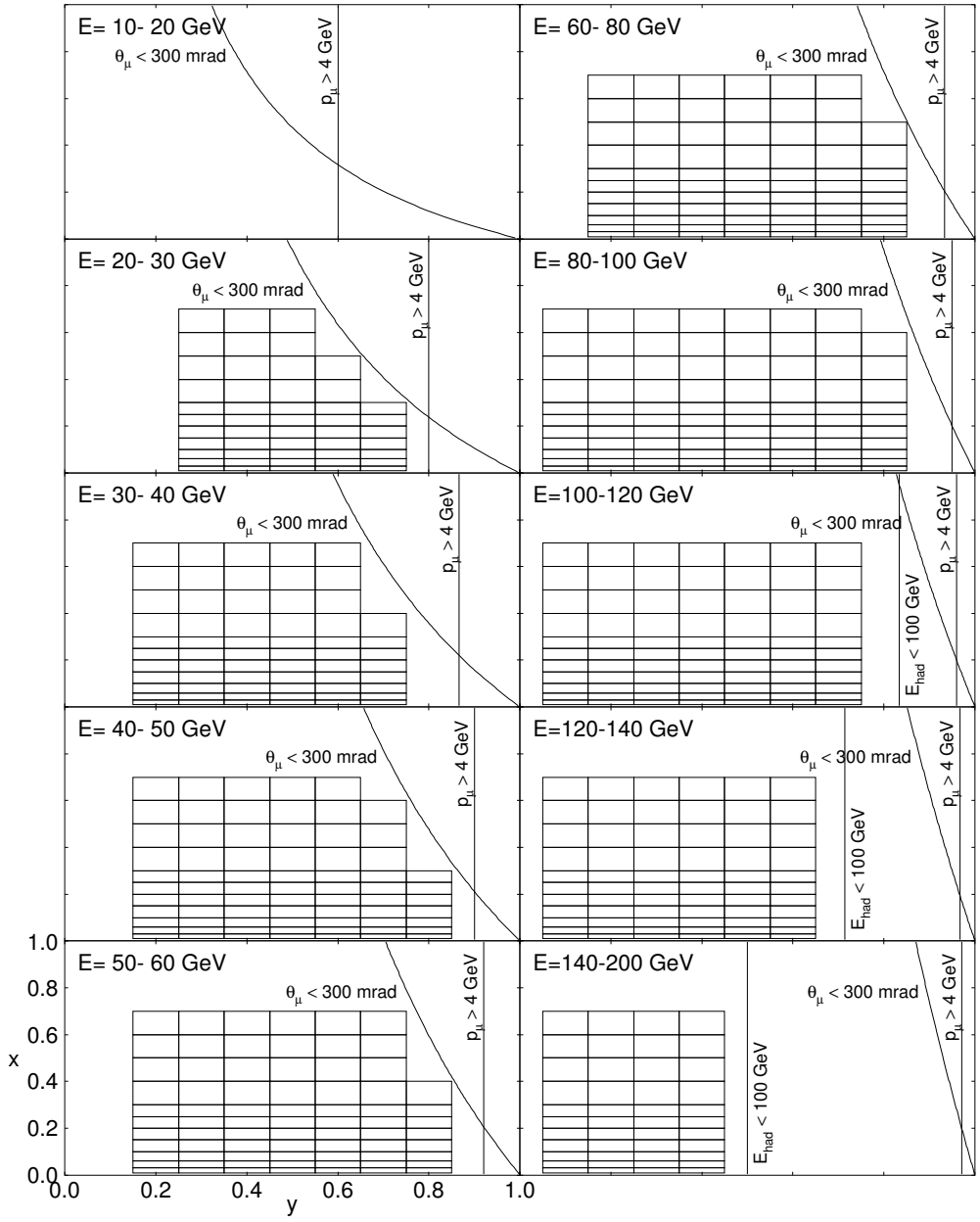

Figure 5.9: Selected bins for the differential cross-section measurement. Indicated are the three cuts that limit the kinematical domain.

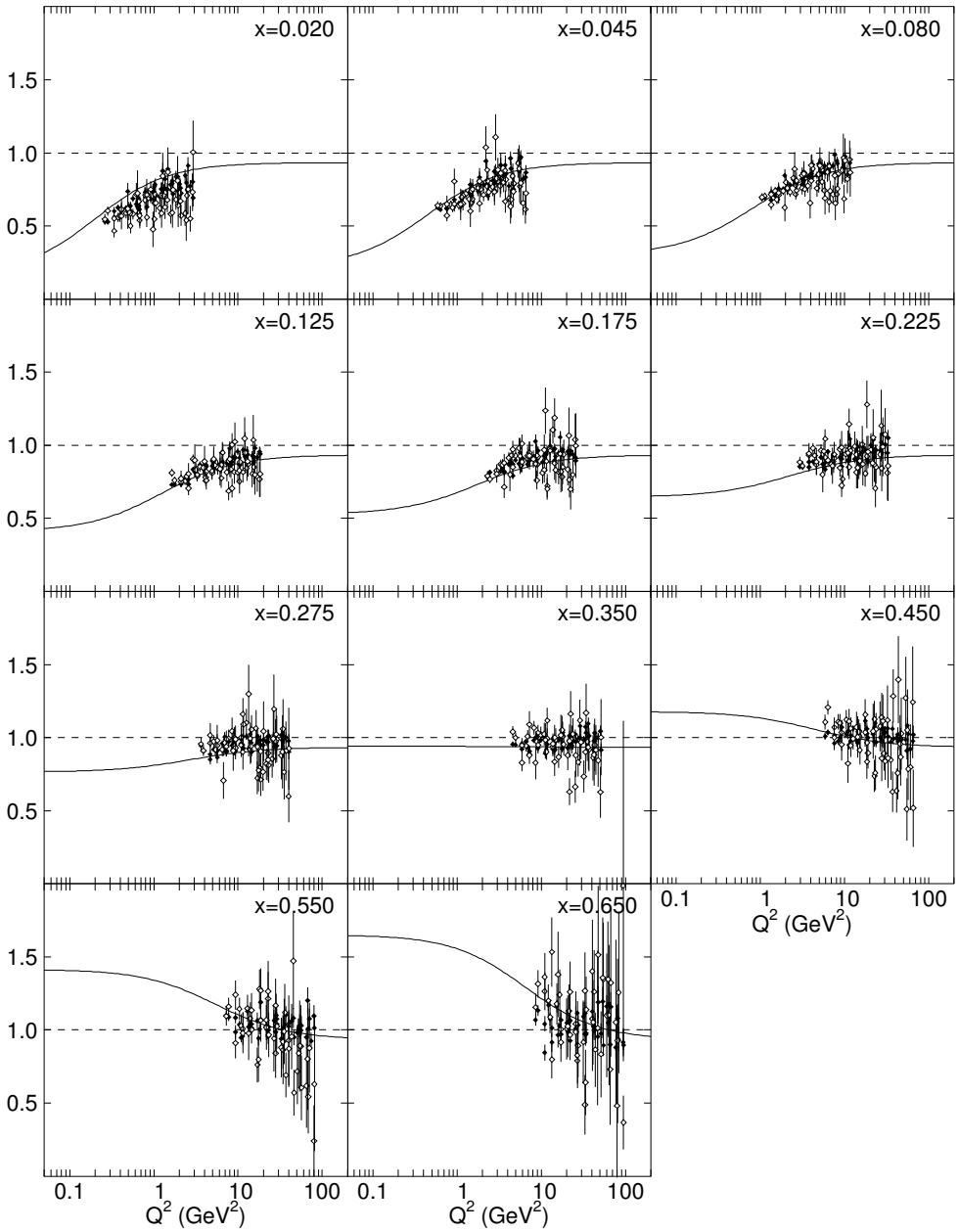

Figure 5.10: Ratio between the measured differential cross-section and that calculated with the model. The solid symbols refer to neutrino data, the open symbols to anti-neutrino data. The curve is the parameterization of Equation 5.11.

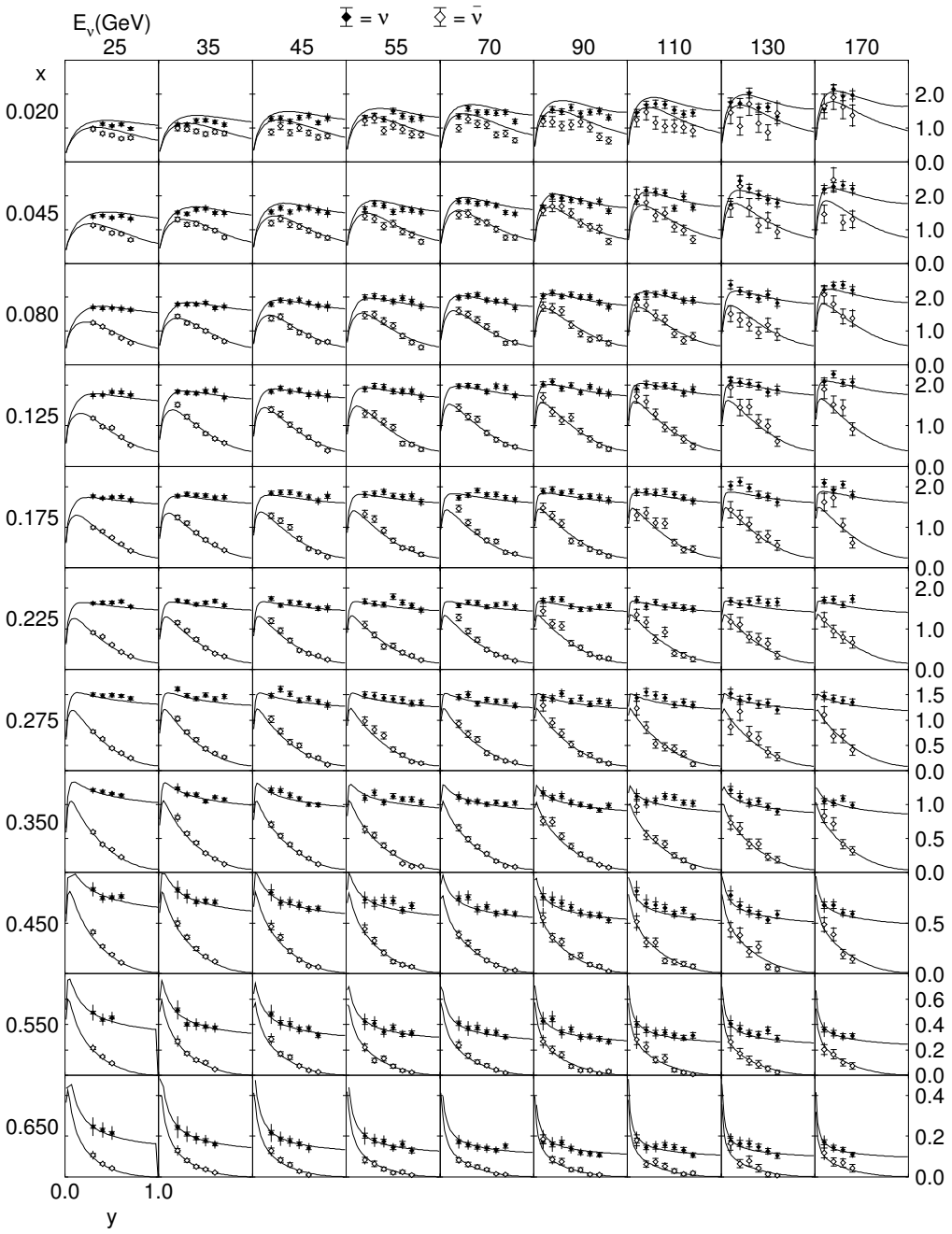

Figure 5.11: Measured (anti-)neutrino-nucleon differential cross-sections as a function of y. The corresponding values of x are indicated on the left, the corresponding values of E on the top. The scale, in $10^{-38}\,\mathrm{cm}^2\mathrm{GeV}^{-1}$, is indicated on the right. The curves show the differential cross-section model used for the calculation of the corrections applied to the data.

CHAPTER 6

STRUCTURE FUNCTION EXTRACTION

To extract the structure functions, measured cross-sections are binned in $Q^2 = 2M_N Exy$ and x, and are corrected for isoscalarity and bin-centering. Also they have been corrected for the radiative effects but not for the charm-quark suppression. Figure 6.1 shows the measured differential cross-sections in Q^2 and x bins. Radiative correction factors applied have been given in figure 6.2.

Structure function extraction has been done by making 3 different types of fits, 6-parameter, 3-parameter and 2-parameter, to the measured differential cross-section. Procedure described in reference [4] has been used in the fits. Contributions of the structure functions to the differential cross-section have been given in figure 6.3

In 6-parameter fit $2xF_1^\nu$, $2xF_1^{\overline{\nu}}$, F_2^ν, $F_2^{\overline{\nu}}$, xF_3^ν and $xF_3^{\overline{\nu}}$ is fit to the measured differential cross-section values in a bin using equation 1.3 if it has at least 4 measurements in different y value, one being $y \geq 0.5$, in that bin. An example bin for 6-parameter fit has been given in figure 6.4. Figures 6.5, 6.6 and 6.7 shows the results of the fit for $2xF_1$, F_2 and xF_3.

In 3-parameter fit, using the relations $2xF_1^\nu = 2xF_1^{\overline{\nu}}$ and $F_2^\nu = F_2^{\overline{\nu}}$, 6 parameters have been reduced to the 4 parameters, namely average of $2xF_1$, F_2 and xF_3 for neutrino and anti-neutrino and $\Delta xF_3 = xF_3^\nu - xF_3^{\overline{\nu}}$. Then it is further reduced to the 3 parameters by constraining the ΔxF_3 to the strange quark distribution and attributing a 20% systematic uncertainty. Then the 3-parameter has been applied for the differential cross-section bins with at least 2 measurements, one of which has $y \geq 0.4$. An example fit in a bin is given in figure 6.8. Result of the fit has been given in figure 6.9.

The results of the 3-parameter fit can be used in calculation of Callan-Gross relation R

$$R = \left(1 + \frac{4M_N^2 x^2}{Q^2}\right) \frac{F_2}{2xF_1} - 1. \tag{6.1}$$

the statistical uncertainty can be determined by using:

$$(\delta R)^2 = \left(1 + \frac{4M_N^2 x^2}{Q^2}\right)^2 \left[\left(\frac{\delta(F_2)}{2xF_1}\right)^2 + \left(\frac{F_2 \delta(2xF_1)}{(2xF_1)^2}\right)^2 - \rho \frac{F_2}{(2xF_1)^3} \delta(F_2)\delta(2xF_1)\right] \tag{6.2}$$

ρ being the correlation between $2xF_1$ and F_2. The result of R has been given in figure 6.10.

The 3 parameters have been reduced to the 2 parameters by the use of the world parameterization of R [17]. A 20% uncertainty is attributed to the R as a systematic error. Then for all the differential cross-section bins with at least 2 measurements, 2-parameter fit is applied. Result of the fit for a bin is given in 6.11. The fitted values of the F_2 and xF_3 have been given in figure 6.12

6.1 Systematical Uncertainties

Several systematical uncertainties for beam flux, cross-section measurements and structure function extraction have been taken into account. The summary of the uncertainties are given in table 6.1.

The hadronic energy scale and offset, muon momentum scale and offset uncertainties are attributed to the calibration of the detector.

Hadronic energy resolution uncertainty represents the uncertainty in the parameterization of the E_{had} found by NN. 2.5% is approximately the value seen in figure 4.7. It has been calculated by enlarging the E_{had} resolution by 2.5% and evaluating its effect on cross-section and structure functions.

The reconstruction inefficiency uncertainty is attributed to the efficiency of the RE function described in chapter 4. It has been calculated by improving the reconstruction efficiency by 5%.

The next four systematic effects incorporate the uncertainties of the total neutrino-nucleon and anti-neutrino-nucleon cross-section. The 2.1% uncertainty on the total neutrino-nucleon cross-section and the 1.4% uncertainty on the anti-neutrino to neutrino cross-section ratio are taken from Ref [3]. In addition, possible non-linearities of

Table 6.1: Overview of the variations applied to evaluate systematic uncertainties.

Error source	**Variation**
Hadronic energy scale	5%
Hadronic energy offset	150 MeV
Hadronic energy resolution	2.5%
Muon momentum scale	2.5%
Muon momentum offset	150 MeV/c
Reconstruction inefficiency	$\pm$5%
Total ν-nucleon cross-section	2.1%
Ratio of $\bar{\nu}$-nucleon and ν-nucleon cross-section	1.4%
Non-linearity of the ν-nucleon cross-section	1%/100 GeV
Non-linearity of the $\bar{\nu}$-nucleon to ν-nucleon cross-section ratio	0.5%/100 GeV
Acceptance corrections	GRV94/GRV98
Radiative corrections	CCFR/GRV98
Phenomenological corrections	on/off
Callan–Gross violation	$R \pm 20\%$
Strange sea	$\Delta xF_3 \pm 20\%$

the cross-sections are taken into account by attributing uncertainties of 1% per 100 GeV for the neutrino cross-section and 0.5% per 100 GeV for the ratio of anti-neutrino and neutrino cross-section [4].

Acceptance corrections uncertainty are to check the input model dependence of the analysis. It has been calculated by changing input parton distribution functions from GRV98 to GRV94 set and re-evaluating cross-section and structure functions.

Radiative corrections uncertainty shows the dependence of the analysis to the type radiative corrections applied to the structure functions. It has been evaluated by using radiative corrections from CCFR instead of the corrections generated by GRV98 pdf.

Phenomenolgical corrections uncertainty is to see the effects of the phenomenological corrections, applied to make the calculated cross-sections to fit to the world average, on the analysis. It is evaluated by removing the multiplicative correction factor.

Callan–Gross violation uncertainty is motivated from the difference between the R calculated from 3-parameter fit and the SLACR90 parameterization. It is calculated for the 2-parameter fit only.

Strange sea is motivated from the assumption that the ΔxF_3 is proportional to the

strange quark distribution in 3-parameter fit.

There is also another uncertainty; the BCT calibration which is only used in beam flux measurement. A 2% uncertainty is attributed to represent uncertainty in the calibration of the beam-current transformers, which is a measure of the protons on target.

The effects of the systematics on the F_2 and xF_3 have been given in figures 6.13 and 6.14.

Main source of error for F_2 is the uncertainty in the hadronic shower energy. Uncertainty in the p_μ is also effective as much as 5% in low x and up to about 10% for high x. Errors from the phenomenological corrections become effective for high x.

The xF_3 is highly effected from the uncertainty in p_μ for both high x and low x. Other significant contributors for the error are uncertainty in E_{had} and like in the case of F_2, the phenomenological correction factor at high x.

6.2 Comparison with Other Experiments

The results for the F_2 and xF_3 have been compared to the earlier neutrino experiments, CCFR [21] and CDHSW [22]. Unlike this analysis or the CDHSW, CCFR results have been corrected for the charm production suppression. The comparisons of the F_2 and xF_3 have been given in figures 6.15 and 6.16 respectively. The figures show an agreement with the CCFR data.

The appendices A and B contain the tables of numerical values of the F_2 and xF_3 found by the 2-parameter fit and effects of each systematical shift.

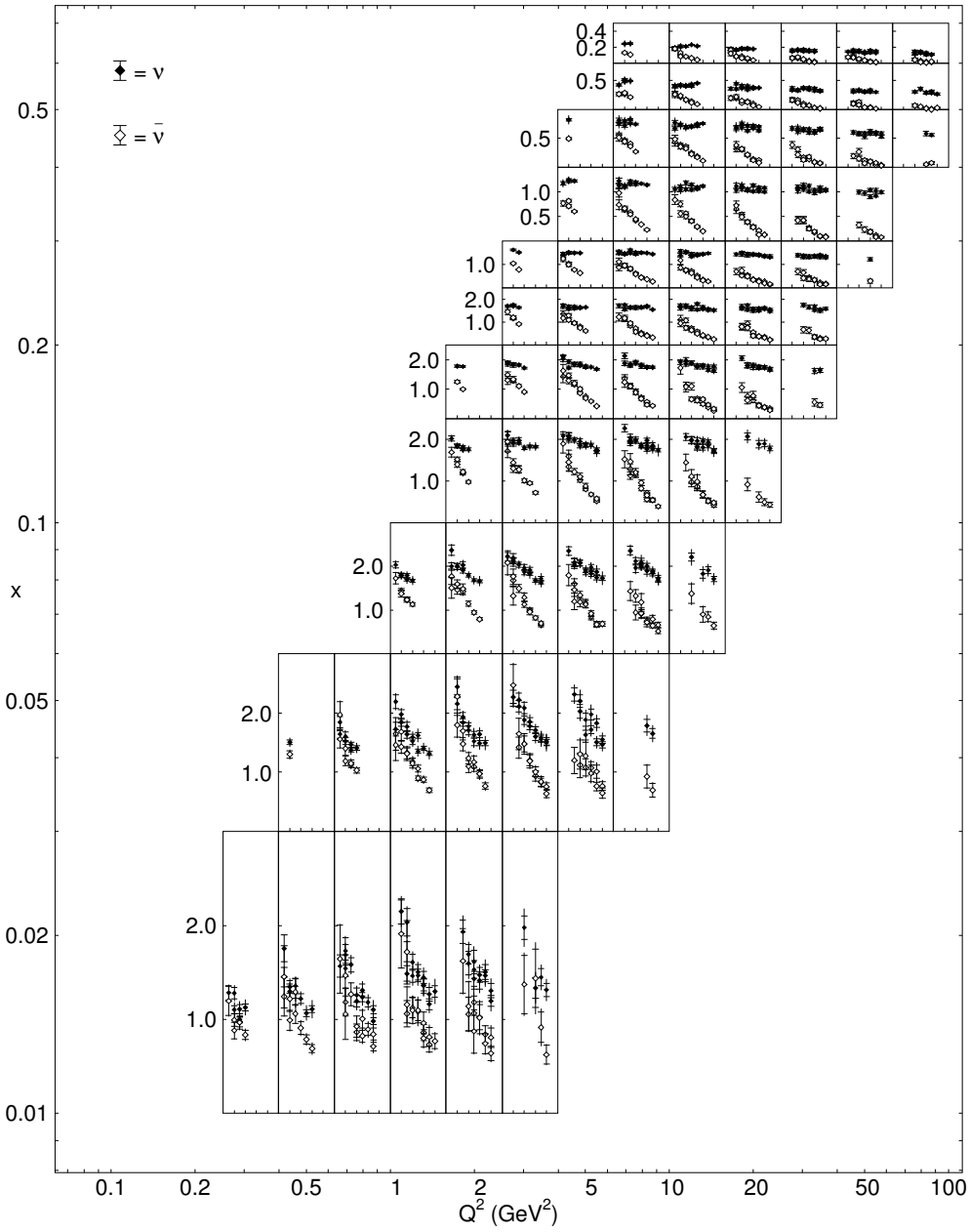

Figure 6.1: Binning in x and Q^2 used for the structure function extraction. Shown inside each bin are the differential cross-section measurements as a function of y. The scale, in $10^{-38}\text{cm}^2\text{GeV}^{-1}$, is indicated on the left-most bin.

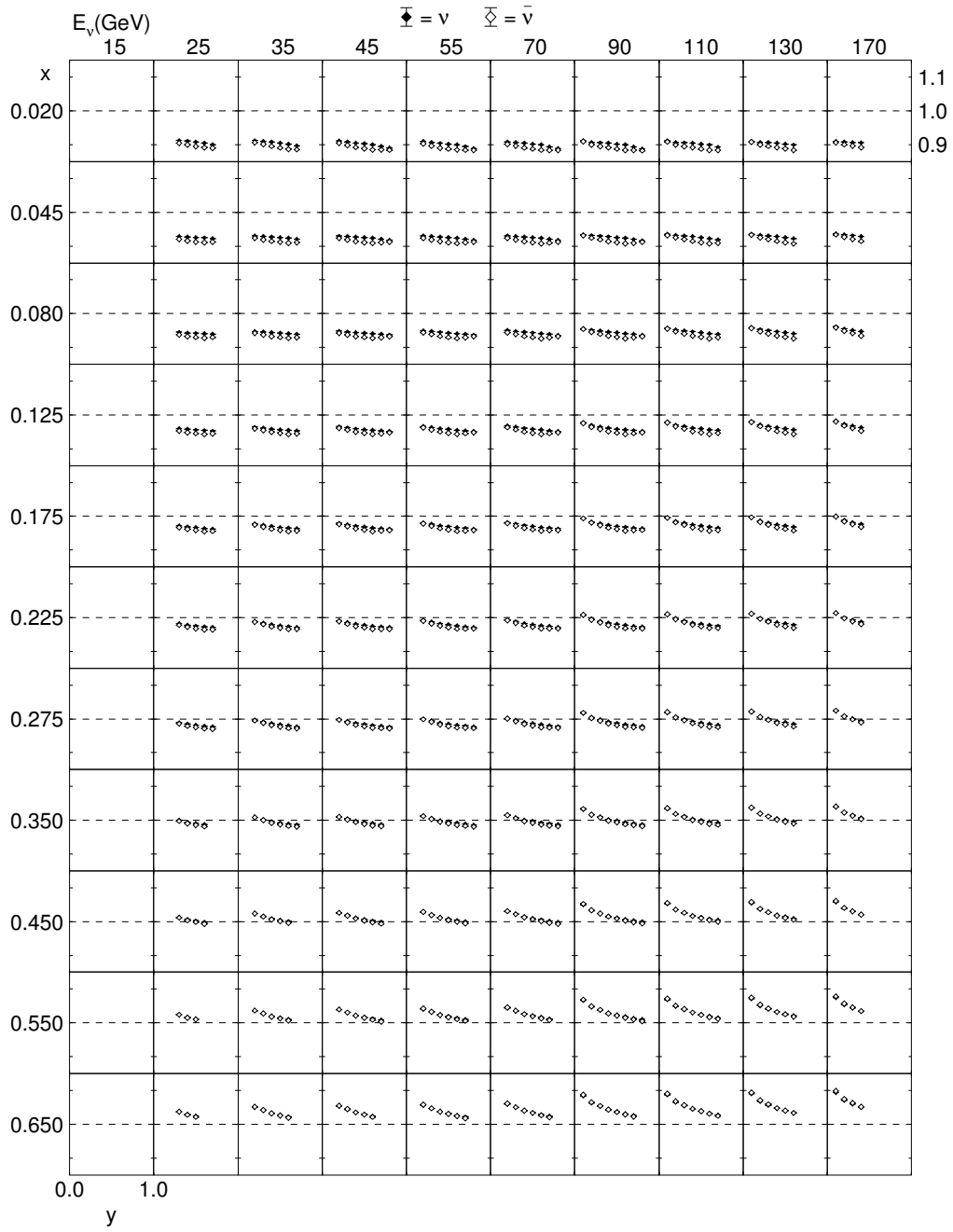

Figure 6.2: Correction factors applied to the differential cross-section to correct for radiative effects. Each plot represents the correction factor as a function of y. The corresponding value of x is indicated on the left, the corresponding value of E on the top. The scale is indicated on the right.

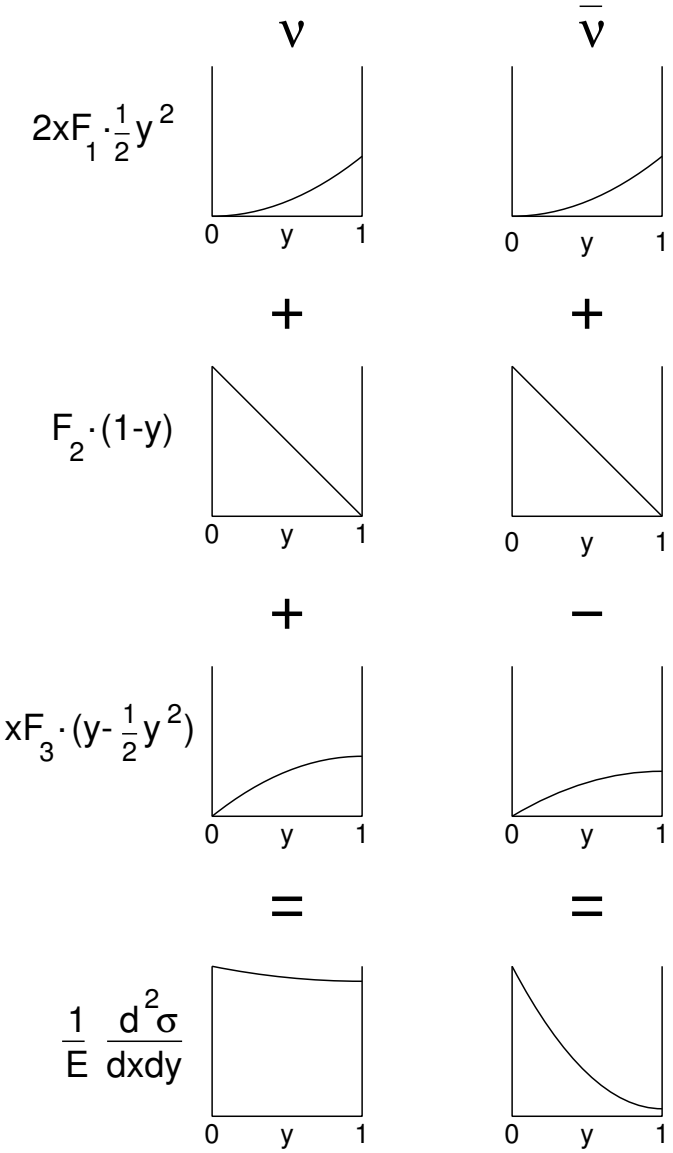

Figure 6.3: Illustration of the contributions from the three structure functions $2xF_1$, F_2, and xF_3 to the differential cross-section (see Equation 1.3).

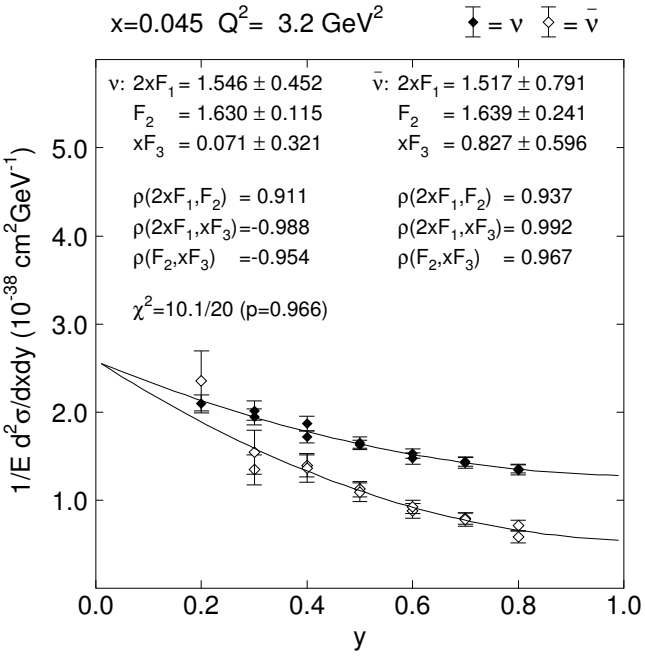

Figure 6.4: An example bin for 6-parameter fit.

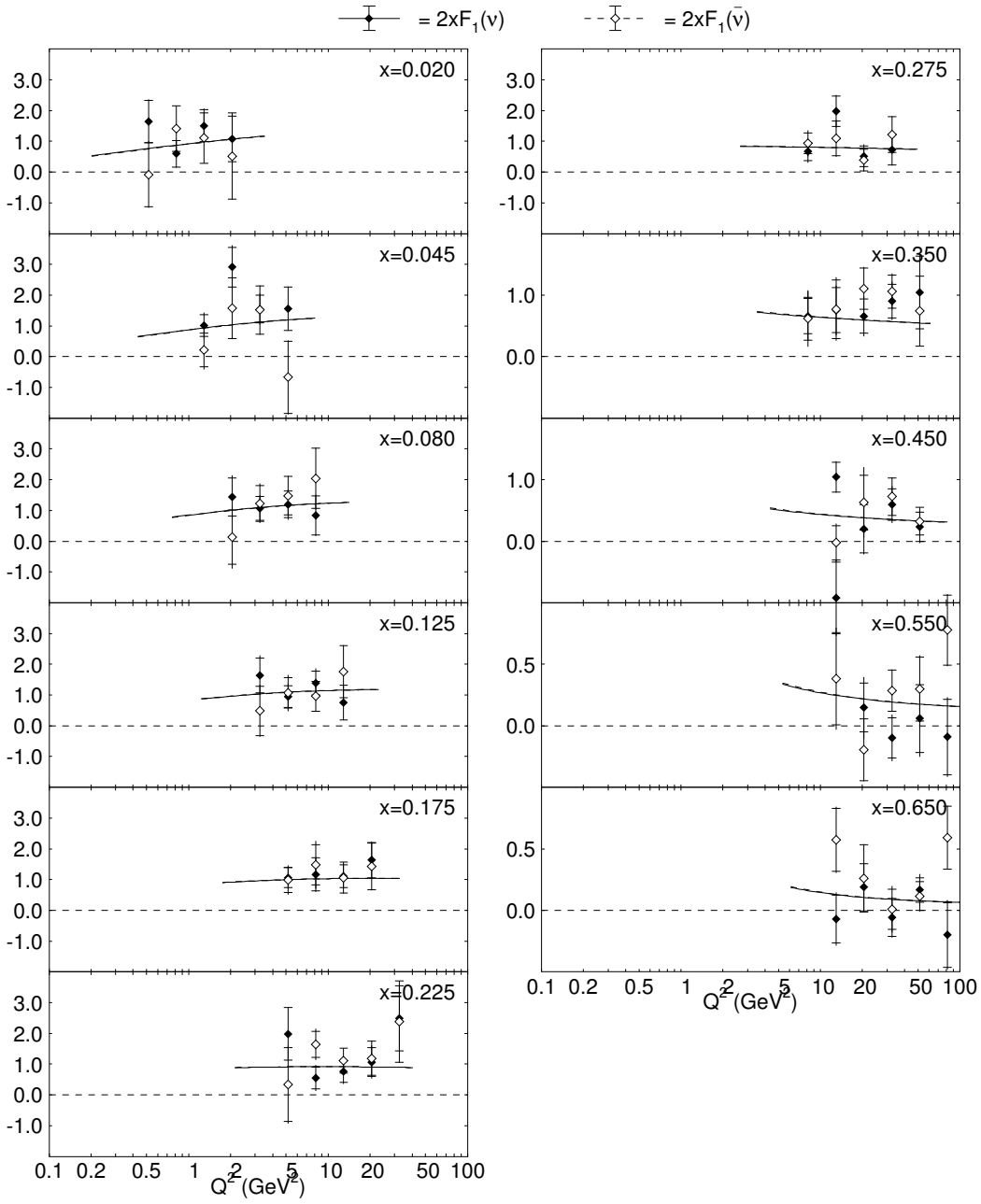

Figure 6.5: The values of $2xF_1$, obtained from the six-parameter fit. The curves show the structure functions of the model.

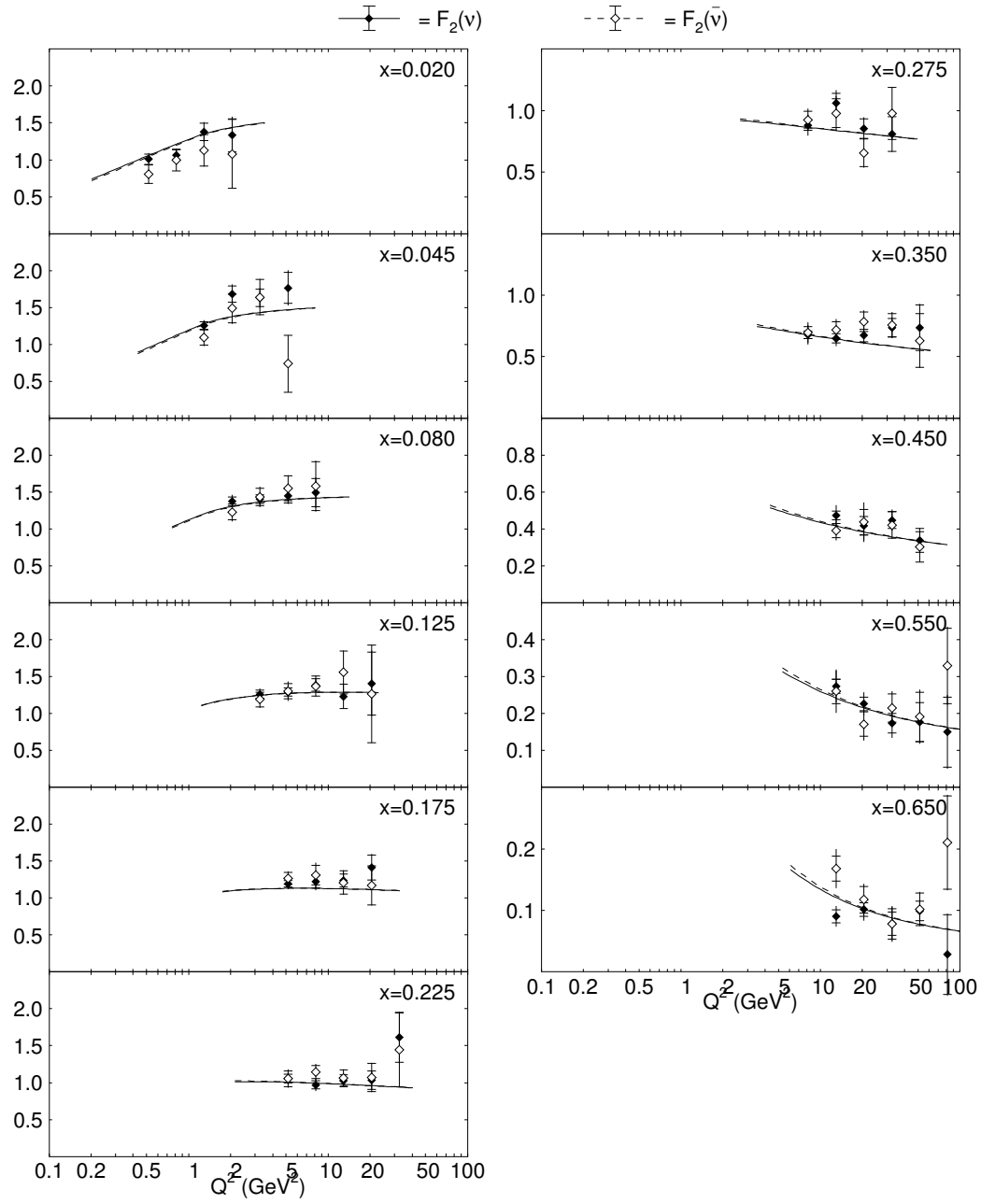

Figure 6.6: The values of F_2, obtained from the six-parameter fit. The curves show the structure functions of the model.

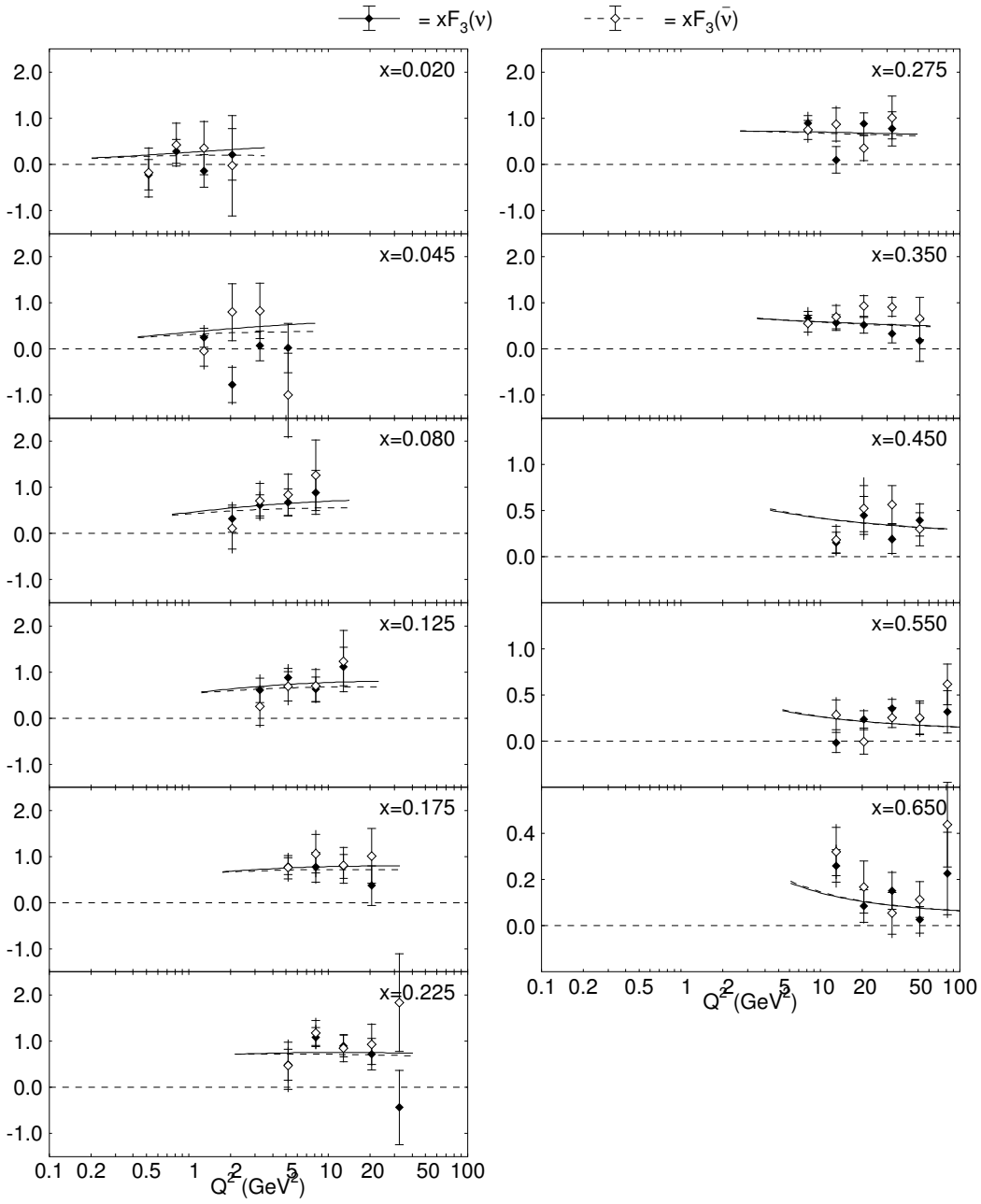

Figure 6.7: The values of xF_3, obtained from the six-parameter fit. The curves show the structure functions of the model.

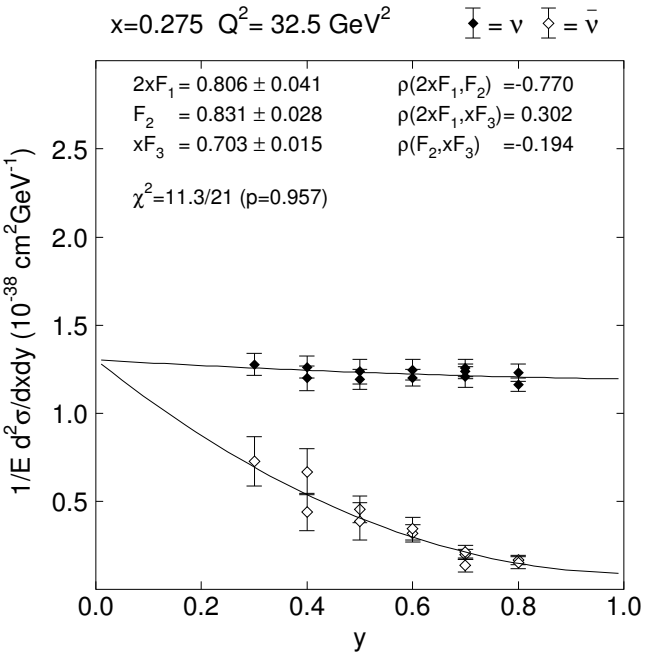

Figure 6.8: Example of the 3-parameter structure function fit to the differential cross-section. Errors are statistical only.

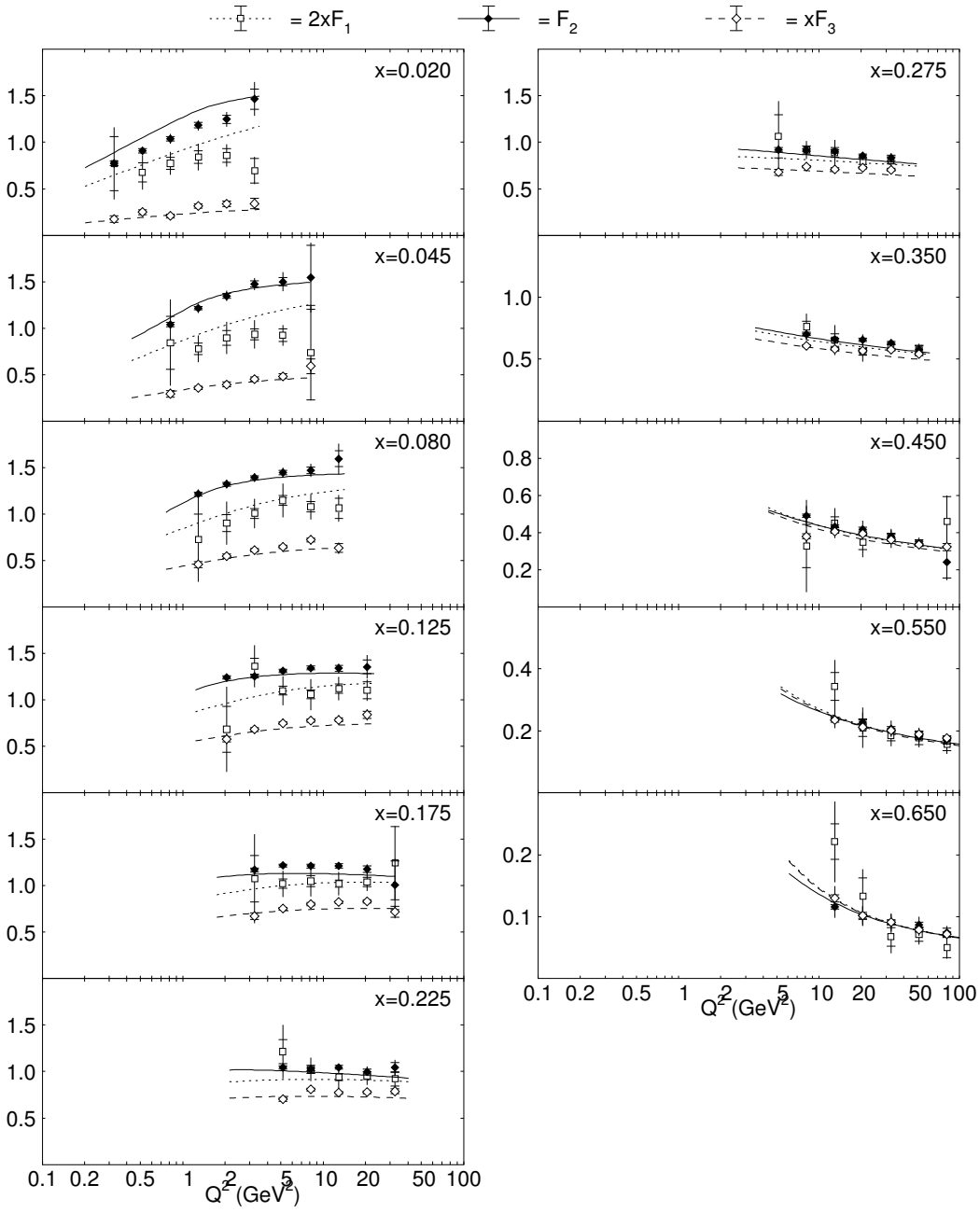

Figure 6.9: The values of $2xF_1$, F_2 and xF_3, obtained from the three-parameter fit. The curves show the structure functions of the model.

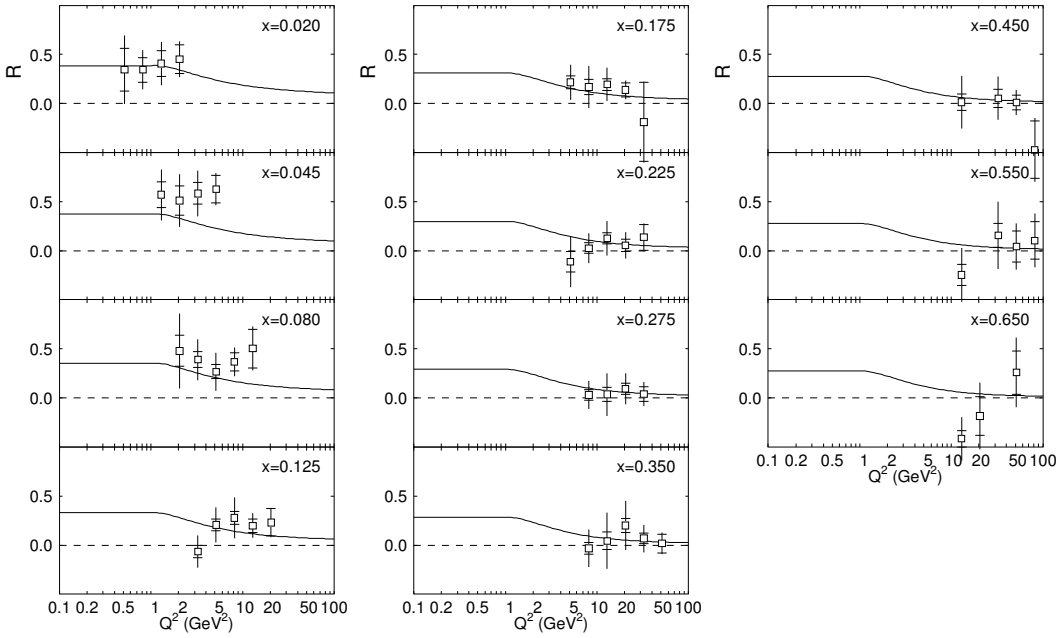

Figure 6.10: The values of $R = \sigma_L/\sigma_T$, obtained from the three-parameter fit. The curve shows the parameterization of the world data.

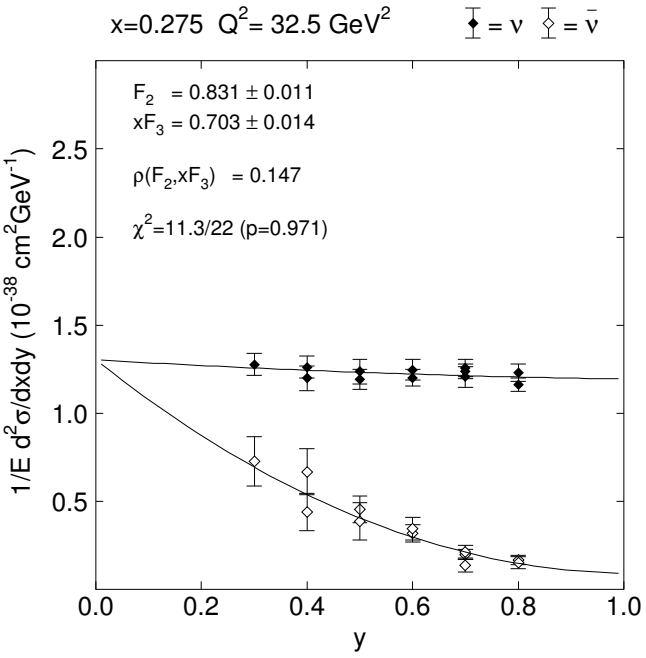

Figure 6.11: Example of the 2-parameter structure function fit to the differential cross-section. Errors are statistical only.

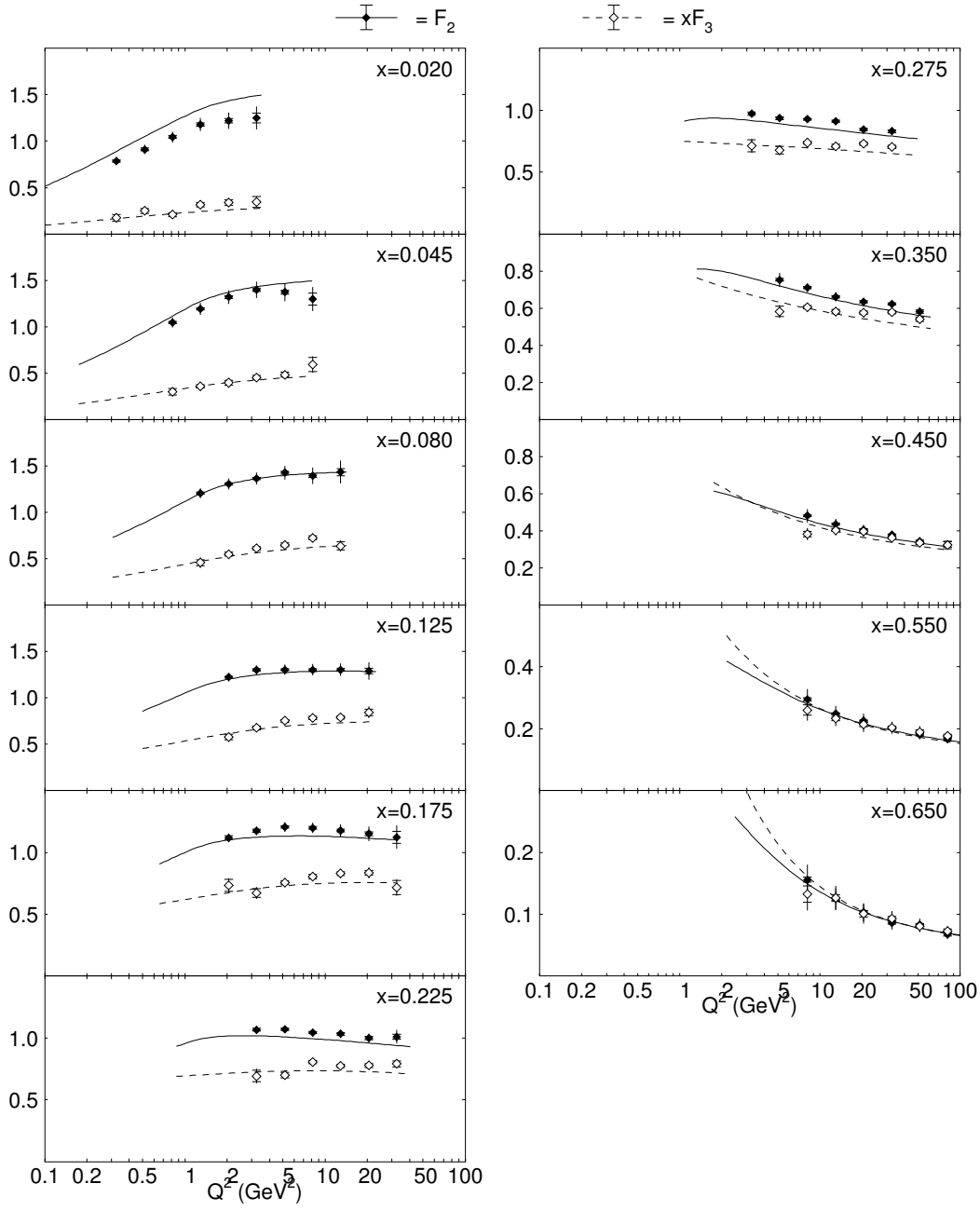

Figure 6.12: Values of F_2 and xF_3, obtained from the two-parameter fit. The curves show the structure functions of the model.

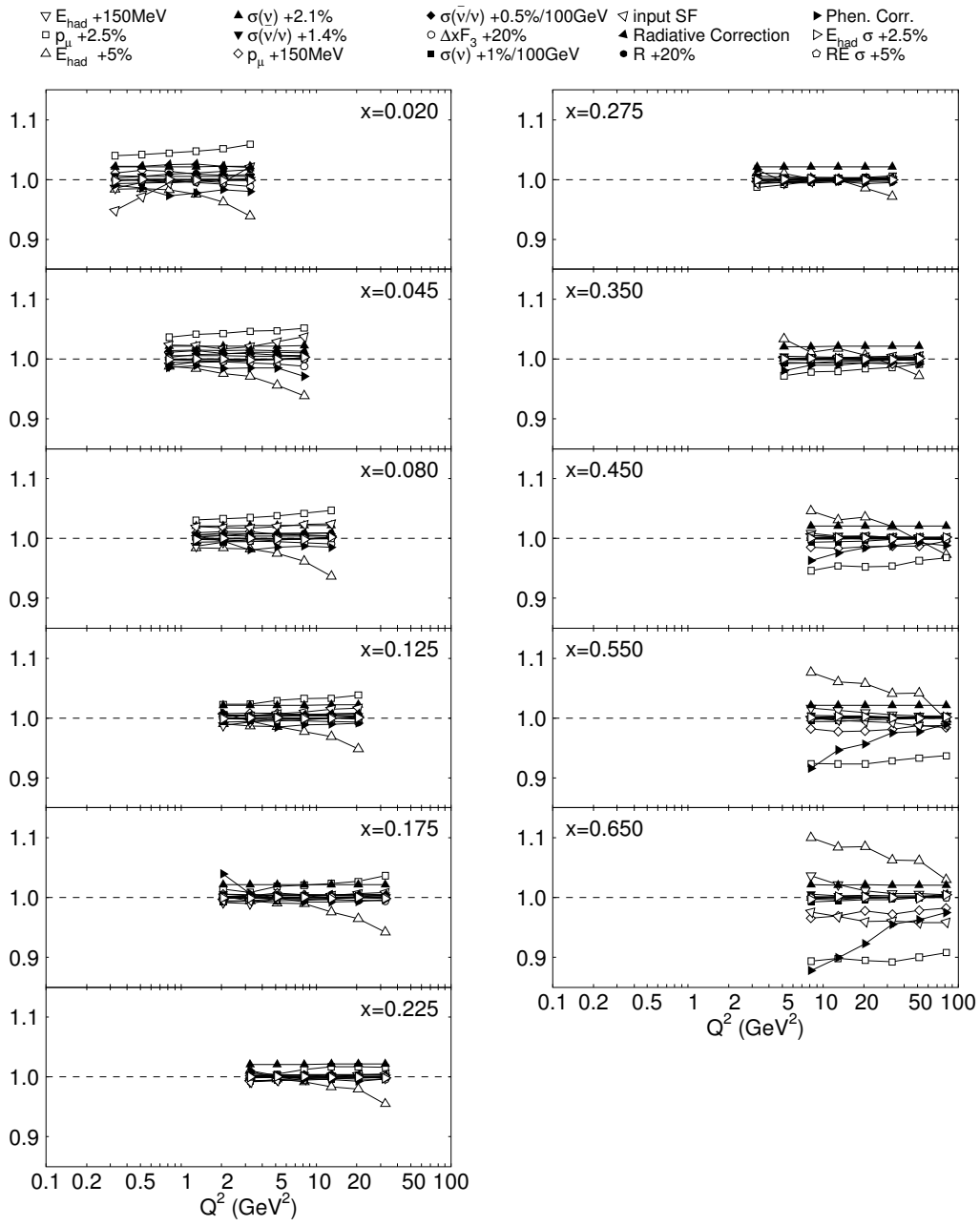

Figure 6.13: Relative effect on F_2 of the fifteen evaluated systematic uncertainties.

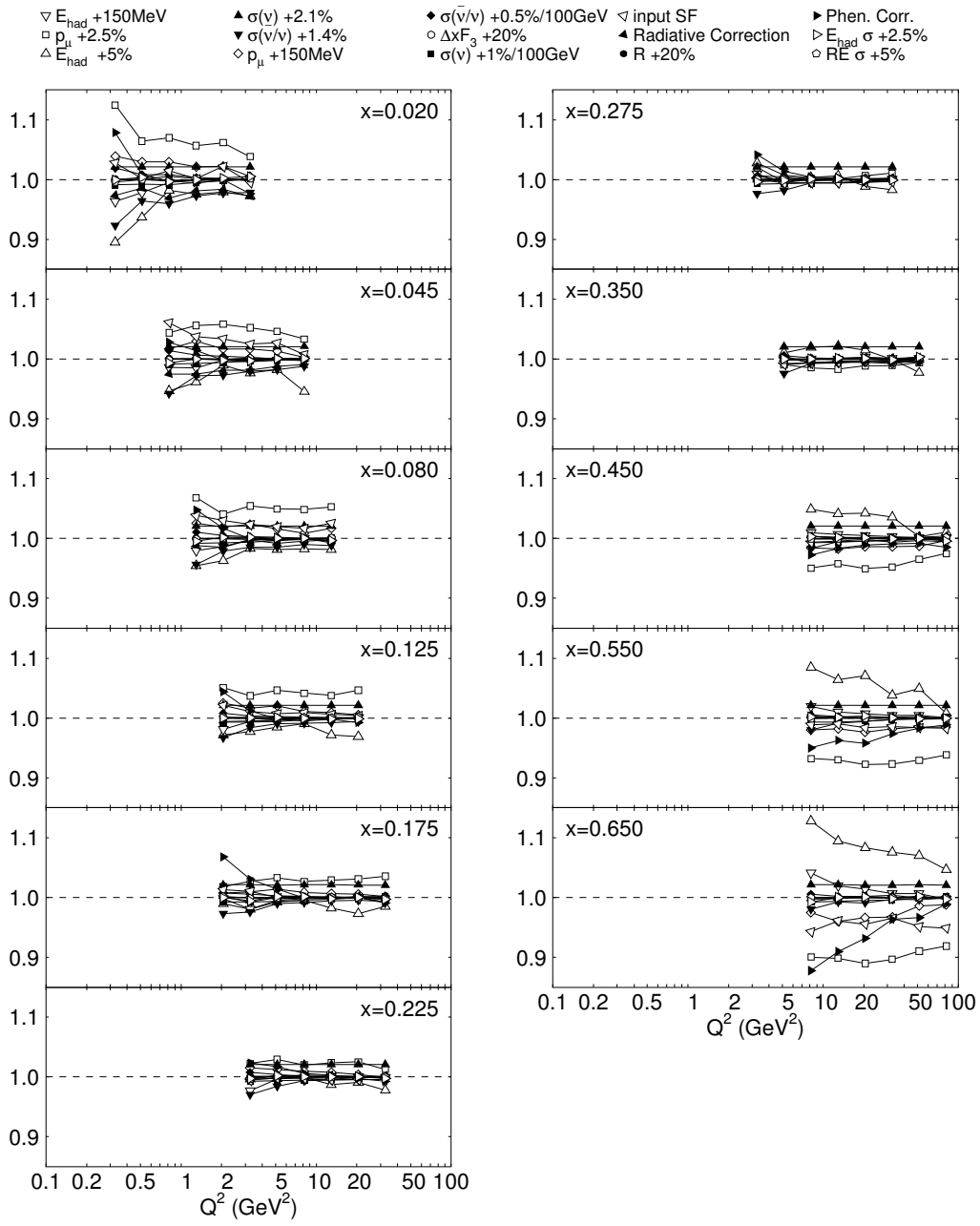

Figure 6.14: Relative effect on xF_3 of the fifteen evaluated systematic uncertainties.

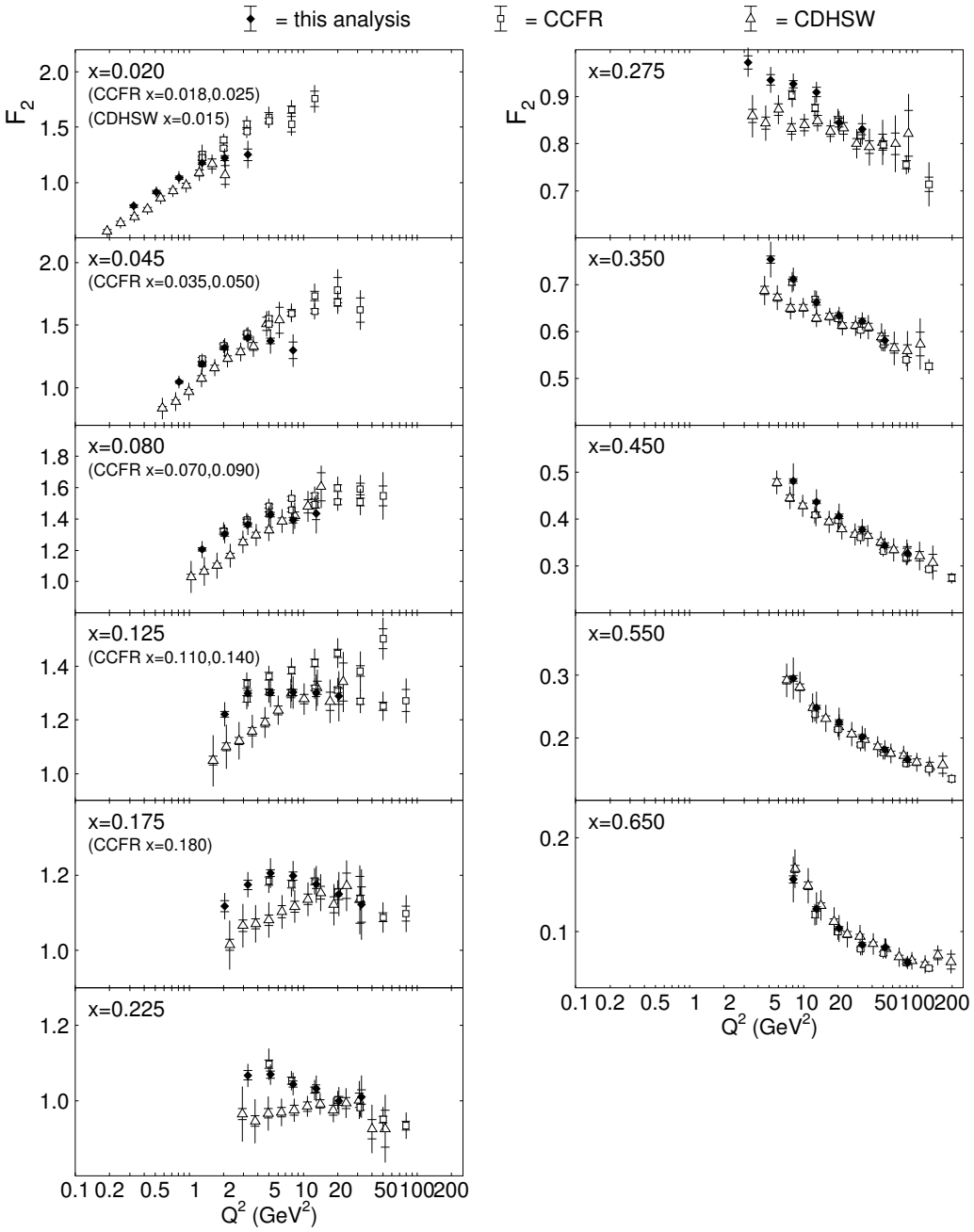

Figure 6.15: Comparison between the isoscalar structure function $F_2^{\nu N}$ from this analysis and the results from the CCFR and CDHSW experiments.

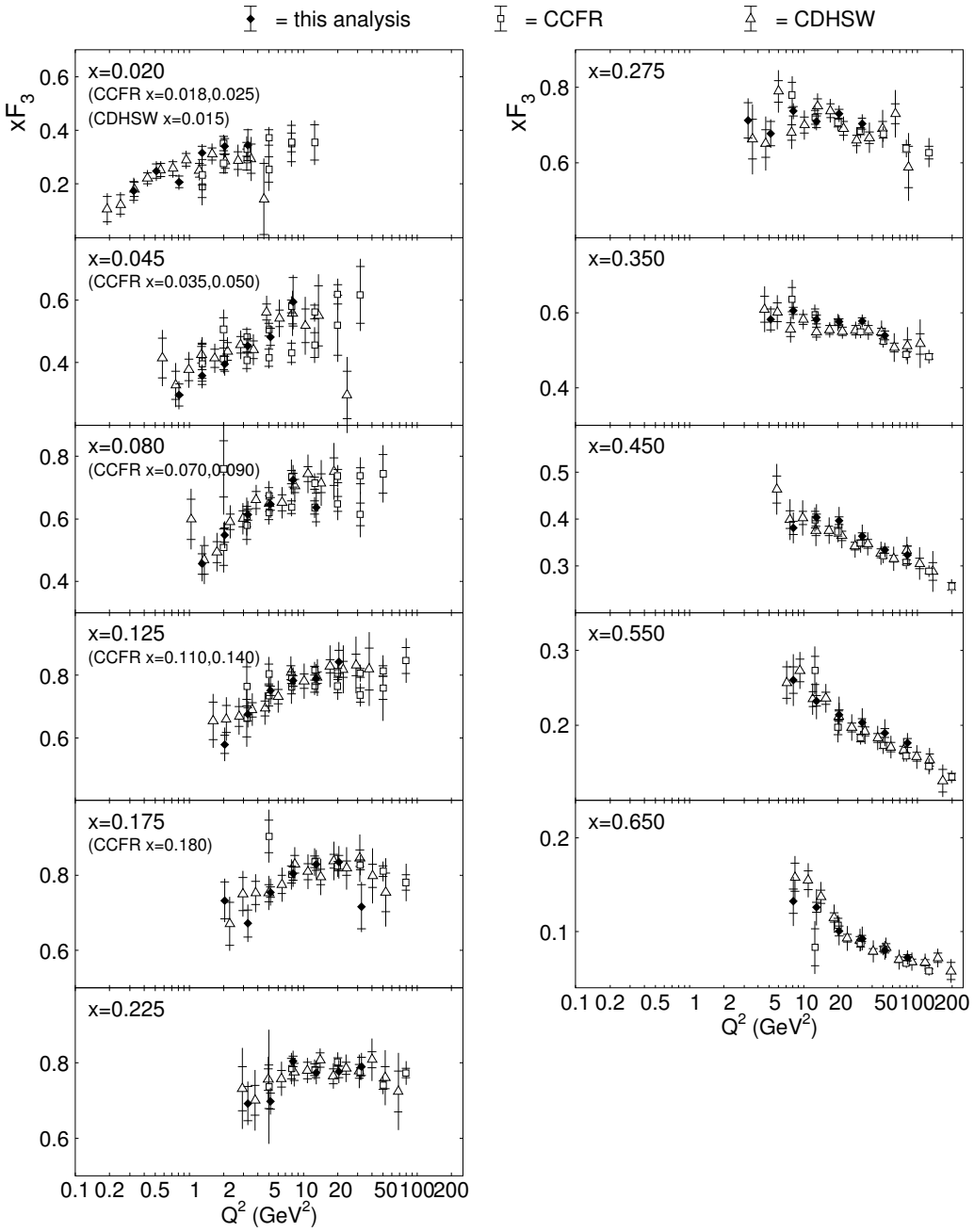

Figure 6.16: Comparison between the isoscalar structure function $xF_3^{\nu N}$ from this analysis and the results from the CCFR and CDHSW experiments.

CHAPTER 7

CONCLUSION

In this analysis, 1998 run of the CHORUS experiment is used. The detector with high resolution calorimeter and large acceptance of the muon spectrometer are suitable for measuring the beam flux for (anti-)neutrino beams. A detailed simulation of beam spectra gives a good estimate of the energy spectra. A high statistics measurement of (anti-)neutrino-lead nucleon differential cross-sections are obtained as a function of the neutrino energy, Bjorken variables x and y in the range of $0.01 \leq x \leq 0.7$, $0.05 \leq y \leq 0.95$, $10 \leq E_\nu \leq 200$GeV.

The measured cross-sections are used to extract the structure functions $2xF_1^\nu$, $2xF_1^{\overline{\nu}}$, F_2^ν, $F_2^{\overline{\nu}}$, xF_3^ν and $xF_3^{\overline{\nu}}$ by a six parameter fit. Using the relations $2xF_1^\nu = 2xF_1^{\overline{\nu}}$, $F_2^\nu = F_2^{\overline{\nu}}$ and constraining the $\Delta xF_3 = xF_3^\nu - xF_3^{\overline{\nu}}$ to the strange quark distribution 6 parameters are reduced to the 3 parameters, the averages of $2xF_1$ and F_2, and xF_3. Results of the 3-parameter fit is used in calculation of Callan-Gross relation R. Finally using the SLACR90 parameterization 2-parameter fit is done.

The results on R is in agreement with the SLACR90 parameterization. The measurement of F_2 agrees with CCFR, CDHSW and the preliminary NuTeV [23] results. Measurement of xF_3 favors the CCFR measurements over the CDHSW measurements, as does the preliminary NuTeV results.

REFERENCES

[1] The Super-Kamiokande Collaboration. Evidence for oscillation of athmospheric neutrinos. *Physical Review Letters*, 1998.

[2] Francis Halzen and Alan D. Martin. *QUARKS AND LEPTONS: An Introductory Course in Modern Physics.* John Wiley & Sons, 1984.

[3] Michael H.Shaevitz Janet M. Conrad and Tim Bolton. Precision measurements with high energy neutrino beams. *Review Modern Physics*, 1998.

[4] Rudolf Gerhard Christiaan Oldeman. *Measurement of differential cross-sections and structure functions in neutrino and anti-neutrino scattering on lead.* PhD thesis, NIKHEF, 2000.

[5] E. Eskut et al. The chorus experiment to search for $\nu_\mu \rightarrow \nu_\tau$ oscillation. *Nucl. Instrum. Meth.*, A401:7, 1997.

[6] Rolf Oldeman. Study of charged current deep inelastic events in the chorus calorimeter. CHORUS internal note 97020.

[7] G. Acquistapace et al. The west area neutrino facility for chorus and nomad experiments: 1994 - 1997 operation. CERN-ECP-95-014.

[8] I. Tsukerman. Mc generators in chorus. *Nucl. Phys. Proc. Suppl.*, 112:177–182, 2002. hep-ph/0202260.

[9] A. Fassò, A. Feerari, P.R.Sala, and J.Ranft. Fluka: Status and prospective for hadronic applications.

[10] NOMAD Collaboration. The nomad experiment at the cern sps. *Nucl. Instrum. Meth.*, A 404:96–128, 1998.

[11] S. Sorrentino. Gbeam, the neutrino beam simulation. CHORUS internal note 98005.

[12] P. Zucchelli and I.I. Tsukerman. Jetta: Physics and manual. CHORUS internal note 2000007.

[13] Geant — detector description and simulation tool. CERN program library long writeup W5013.

[14] A.G Cocco, M. Messina, and R. Santorelli. Vertex measurement in the calorimeter by neural network technique. CHORUS internal note 2000020.

[15] A.G Cocco, M. Messina, and R. Santorelli. Shower energy measurements for calorimeter neutrino cc events using a neural network. CHORUS internal note 2000019.

[16] M. Glück, E. Reya, and A. Vogt. Dynamical parton distributions revisited. *Eur. Phys. J.*, C5:461–470, 1998.

[17] L. W. Whitlow, Stephen Rock, A. Bodek, E. M. Riordan, and S. Dasu. A precise extraction of r = sigma-l / sigma-t from a global analysis of the slac deep inelastic e p and e d scattering cross-sections. *Phys. Lett.*, B250:193–198, 1990.

[18] D. Yu. Bardin and V. A. Dokuchaeva. On the radiative corrections to the neutrino deep inelastic scattering. JINR-E2-86-260.

[19] R. M. Sternheimer, M. J. Berger, and S. M. Seltzer. Density effect for the ionization loss of charged particles in various substances. *At. Data Nucl. Data Tabl.*, 30:261, 1984.

[20] Gerald R. Lynch and Orin I. Dahl. Approximations to multiple coulomb scattering. *Nucl. Instrum. Meth.*, B58:6–10, 1991.

[21] W. G. Seligman et al. Improved determination of α_s from neutrino nucleon scattering. *Phys. Rev. Lett.*, 79:1213, 1997.

[22] J.P.Berge et al. A measurement of differential cross-sections and nucleon structure functions in charged current neutrino interactions on iron. *Z. Phys.*, C49:187–224, 1991.

[23] D.Naples, NuTeV Collaboration, et al. Nutev cross section and structure function measurements. *arXiv:hep-ex/0307005*, 2005.

[24] H. Plothow-Besch. Pdflib: Proton, pion and photon parton density functions, parton density functions of the nucleus and α_s calculations. User's Manual -Version 8.04, W5051 PDFLIB, 2000.04.17, CERN-PPE.

APPENDIX A

F_2 TABLE

This appendix contains the numerical values of the F_2 found by 2-parameter fit. Table A.1 contains the explanations of the labels of the columns.

Table A.1: Explanation of the labels.

Label	**Explanation**	**Variation**
x	Central value of Bjorken-x	—
Q^2	Central value of Q^2 (GeV^2)	—
F_2	Extracted value of the Structure Function F_2	—
σ_{stat}	Statistical Uncertainty	—
σ_{syst}	Systematical Uncertainty	—
sh 1	Hadronic energy scale	5%
sh 2	Hadronic energy offset	150 MeV
sh 3	Muon momentum scale	2.5%
sh 4	Muon momentum offset	150 MeV/c
sh 5	Total ν-nucleon cross-section	2.1%
sh 6	Ratio of $\bar{\nu}$-nucleon and ν-nucleon cross-section	1.4%
sh 7	Non-linearity of the ν-nucleon cross-section	1%/100 GeV
sh 8	Non-linearity of the $\bar{\nu}$-nucleon to ν-nucleon cross-section ratio	0.5%/100 GeV
sh 9	Strange sea	$\Delta xF_3 \pm 20\%$
sh 10	Callan–Gross violation	$R \pm 20\%$
sh 11	Acceptance corrections	GRV94/GRV98
sh 12	Radiative corrections	CCFR/GRV98
sh 13	Reconstruction inefficiency	$\pm 5\%$
sh 14	Phenomenological corrections	on/off
sh 15	Hadronic energy resolution	2.5%

Table A.2: F_2 table found by 2-parameter fit.

x	Q^2	F_2	σ_{stat}	σ_{syst}	sh 1	sh 2	sh 3	sh 4	sh 5	sh 6	sh 7	sh 8
0.020	0.325	0.7855	0.0122	0.0607	-0.0130	-0.0111	0.0313	0.0089	0.0165	0.0047	-0.0051	-0.0011
0.020	0.515	0.9116	0.0140	0.0598	-0.0135	-0.0046	0.0382	0.0141	0.0193	0.0048	-0.0051	-0.0010
0.020	0.816	1.0449	0.0148	0.0696	-0.0180	-0.0027	0.0463	0.0140	0.0223	0.0058	-0.0048	-0.0011
0.020	1.293	1.1789	0.0178	0.0813	-0.0286	-0.0008	0.0559	0.0102	0.0253	0.0063	-0.0034	-0.0008
0.020	2.052	1.2201	0.0238	0.0921	-0.0459	-0.0016	0.0629	0.0092	0.0266	0.0063	-0.0005	-0.0003
0.020	3.250	1.2505	0.0516	0.1218	-0.0765	-0.0009	0.0738	0.0105	0.0278	0.0066	0.0022	0.0001
0.045	0.816	1.0459	0.0123	0.0592	-0.0122	-0.0117	0.0380	0.0122	0.0221	0.0060	-0.0062	-0.0014
0.045	1.293	1.1908	0.0113	0.0720	-0.0191	-0.0054	0.0494	0.0171	0.0254	0.0062	-0.0067	-0.0014
0.045	2.052	1.3191	0.0154	0.0819	-0.0324	-0.0032	0.0563	0.0127	0.0283	0.0069	-0.0057	-0.0012
0.045	3.250	1.3983	0.0173	0.0951	-0.0402	-0.0004	0.0648	0.0136	0.0303	0.0069	-0.0035	-0.0008
0.045	5.146	1.3728	0.0221	0.1076	-0.0599	0.0000	0.0648	0.0093	0.0301	0.0069	0.0001	-0.0001
0.045	8.155	1.2974	0.0658	0.1276	-0.0800	-0.0008	0.0671	0.0068	0.0289	0.0060	0.0024	0.0003
0.080	1.293	1.2053	0.0112	0.0596	-0.0192	-0.0158	0.0371	0.0115	0.0255	0.0069	-0.0078	-0.0017
0.080	2.052	1.3039	0.0122	0.0646	-0.0209	-0.0077	0.0430	0.0148	0.0277	0.0063	-0.0073	-0.0014
0.080	3.250	1.3630	0.0118	0.0743	-0.0243	-0.0026	0.0475	0.0158	0.0292	0.0060	-0.0066	-0.0012
0.080	5.146	1.4266	0.0137	0.0828	-0.0350	-0.0008	0.0543	0.0104	0.0307	0.0063	-0.0041	-0.0008
0.080	8.155	1.3939	0.0173	0.0953	-0.0534	-0.0006	0.0587	0.0087	0.0303	0.0057	-0.0009	-0.0003
0.080	12.925	1.4333	0.0386	0.1264	-0.0904	-0.0004	0.0674	0.0061	0.0314	0.0062	0.0027	0.0002
0.125	2.052	1.2218	0.0102	0.0462	-0.0117	-0.0149	0.0279	0.0082	0.0258	0.0066	-0.0080	-0.0016
0.125	3.250	1.2995	0.0109	0.0489	-0.0177	-0.0089	0.0304	0.0099	0.0276	0.0057	-0.0071	-0.0012
0.125	5.146	1.3024	0.0102	0.0580	-0.0186	-0.0012	0.0380	0.0111	0.0278	0.0050	-0.0063	-0.0010
0.125	8.155	1.3028	0.0115	0.0637	-0.0297	-0.0019	0.0420	0.0073	0.0280	0.0048	-0.0040	-0.0006
0.125	12.925	1.3013	0.0146	0.0715	-0.0406	0.0004	0.0430	0.0057	0.0282	0.0046	-0.0008	-0.0002
0.125	20.520	1.2884	0.0302	0.0923	-0.0666	-0.0023	0.0495	0.0047	0.0280	0.0041	0.0026	0.0002
0.175	2.052	1.1185	0.0147	0.0552	0.0021	-0.0095	0.0160	0.0061	0.0235	0.0061	-0.0079	-0.0016
0.175	3.250	1.1752	0.0124	0.0331	-0.0063	-0.0120	0.0101	0.0032	0.0248	0.0058	-0.0063	-0.0012
0.175	5.146	1.2061	0.0087	0.0389	-0.0110	-0.0024	0.0226	0.0092	0.0256	0.0046	-0.0069	-0.0010

Table A.3: F_2 table (continued).

x	Q^2	F_2	σ_{stat}	σ_{syst}	sh 1	sh 2	sh 3	sh 4	sh 5	sh 6	sh 7	sh 8
0.175	8.155	1.1984	0.0111	0.0401	-0.0124	-0.0005	0.0244	0.0052	0.0255	0.0044	-0.0052	-0.0007
0.175	12.925	1.1767	0.0116	0.0492	-0.0284	-0.0002	0.0274	0.0045	0.0252	0.0036	-0.0030	-0.0004
0.175	20.520	1.1504	0.0143	0.0589	-0.0409	-0.0001	0.0306	0.0030	0.0248	0.0033	0.0002	0.0000
0.175	32.500	1.1226	0.0473	0.0822	-0.0654	0.0001	0.0410	0.0000	0.0243	0.0039	0.0020	0.0002
0.225	3.250	1.0670	0.0126	0.0319	0.0115	-0.0091	0.0021	0.0022	0.0224	0.0057	-0.0066	-0.0013
0.225	5.146	1.0695	0.0094	0.0264	-0.0041	-0.0051	0.0050	0.0019	0.0226	0.0047	-0.0062	-0.0011
0.225	8.155	1.0440	0.0086	0.0291	-0.0083	-0.0009	0.0134	0.0036	0.0221	0.0033	-0.0055	-0.0007
0.225	12.925	1.0323	0.0100	0.0341	-0.0168	-0.0001	0.0176	0.0030	0.0220	0.0031	-0.0035	-0.0004
0.225	20.520	0.9997	0.0118	0.0358	-0.0205	-0.0005	0.0170	0.0009	0.0214	0.0026	-0.0013	-0.0002
0.225	32.500	1.0098	0.0193	0.0538	-0.0455	-0.0015	0.0161	-0.0026	0.0217	0.0026	0.0013	0.0001
0.275	3.250	0.9735	0.0143	0.0326	0.0105	-0.0019	-0.0126	-0.0015	0.0204	0.0052	-0.0069	-0.0013
0.275	5.146	0.9363	0.0113	0.0254	0.0096	-0.0053	-0.0077	-0.0019	0.0197	0.0041	-0.0050	-0.0009
0.275	8.155	0.9275	0.0076	0.0217	0.0017	-0.0005	-0.0032	-0.0028	0.0196	0.0030	-0.0052	-0.0006
0.275	12.925	0.9102	0.0097	0.0205	-0.0001	0.0002	-0.0013	-0.0016	0.0193	0.0028	-0.0039	-0.0005
0.275	20.520	0.8453	0.0096	0.0231	-0.0118	0.0012	0.0031	-0.0003	0.0180	0.0019	-0.0021	-0.0002
0.275	32.500	0.8310	0.0114	0.0307	-0.0236	0.0002	0.0049	-0.0012	0.0177	0.0017	0.0002	0.0000
0.350	5.146	0.7531	0.0077	0.0403	0.0256	0.0003	-0.0211	-0.0053	0.0158	0.0039	-0.0045	-0.0009
0.350	8.155	0.7110	0.0049	0.0252	0.0083	0.0004	-0.0155	-0.0047	0.0149	0.0025	-0.0043	-0.0006
0.350	12.925	0.6620	0.0060	0.0245	0.0119	0.0009	-0.0136	-0.0040	0.0140	0.0021	-0.0026	-0.0004
0.350	20.520	0.6338	0.0057	0.0188	0.0041	0.0014	-0.0104	-0.0040	0.0134	0.0014	-0.0021	-0.0002
0.350	32.500	0.6219	0.0063	0.0183	-0.0055	0.0004	-0.0086	-0.0051	0.0132	0.0011	-0.0009	-0.0001
0.350	51.455	0.5809	0.0095	0.0220	-0.0160	-0.0001	-0.0051	-0.0025	0.0123	0.0009	0.0008	0.0000
0.450	8.155	0.4811	0.0049	0.0408	0.0221	0.0044	-0.0259	-0.0071	0.0101	0.0022	-0.0029	-0.0005
0.450	12.925	0.4363	0.0040	0.0291	0.0137	0.0019	-0.0199	-0.0071	0.0092	0.0013	-0.0023	-0.0003
0.450	20.520	0.4060	0.0049	0.0271	0.0145	0.0015	-0.0192	-0.0055	0.0085	0.0011	-0.0016	-0.0002
0.450	32.500	0.3779	0.0050	0.0217	0.0074	0.0010	-0.0174	-0.0048	0.0080	0.0008	-0.0007	-0.0001
0.450	51.455	0.3438	0.0051	0.0156	-0.0011	0.0004	-0.0127	-0.0044	0.0073	0.0005	0.0001	0.0000

Table A.4: F_2 table (continued).

x	Q^2	F_2	σ_{stat}	σ_{syst}	sh 1	sh 2	sh 3	sh 4	sh 5	sh 6	sh 7	sh 8
0.450	81.550	0.3264	0.0152	0.0159	-0.0088	-0.0006	-0.0105	-0.0014	0.0069	0.0005	0.0006	0.0001
0.550	8.155	0.2949	0.0047	0.0415	0.0224	0.0049	-0.0225	-0.0054	0.0062	0.0014	-0.0017	-0.0003
0.550	12.925	0.2484	0.0031	0.0289	0.0149	0.0031	-0.0191	-0.0056	0.0052	0.0009	-0.0014	-0.0002
0.550	20.520	0.2253	0.0034	0.0249	0.0130	0.0020	-0.0173	-0.0050	0.0047	0.0007	-0.0008	-0.0001
0.550	32.500	0.2015	0.0032	0.0184	0.0083	0.0010	-0.0144	-0.0039	0.0042	0.0004	-0.0005	0.0000
0.550	51.455	0.1811	0.0039	0.0157	0.0075	0.0007	-0.0121	-0.0022	0.0038	0.0003	0.0000	0.0000
0.550	81.550	0.1658	0.0046	0.0117	-0.0004	0.0005	-0.0105	-0.0027	0.0035	0.0002	0.0002	0.0000
0.650	8.155	0.1558	0.0038	0.0311	0.0155	0.0057	-0.0166	-0.0054	0.0033	0.0008	-0.0011	-0.0002
0.650	12.925	0.1244	0.0022	0.0217	0.0104	0.0027	-0.0127	-0.0038	0.0026	0.0004	-0.0007	-0.0001
0.650	20.520	0.1035	0.0021	0.0170	0.0088	0.0012	-0.0109	-0.0023	0.0022	0.0004	-0.0004	-0.0001
0.650	32.500	0.0863	0.0019	0.0123	0.0054	0.0006	-0.0093	-0.0024	0.0018	0.0002	-0.0003	0.0000
0.650	51.455	0.0830	0.0020	0.0111	0.0051	0.0005	-0.0083	-0.0018	0.0017	0.0002	0.0000	0.0000
0.650	81.550	0.0673	0.0023	0.0075	0.0020	0.0003	-0.0062	-0.0012	0.0014	0.0001	0.0001	0.0000

Table A.5: F_2 table (continued).

x	Q^2	F_2	σ_{stat}	σ_{syst}	sh 9	sh 10	sh 11	sh 12	sh 13	sh 14	sh 15
0.020	0.325	0.7855	0.0122	0.0607	-0.0005	0.0018	-0.0408	0.0171	-0.0001	-0.0073	-0.0017
0.020	0.515	0.9116	0.0140	0.0598	-0.0013	0.0052	-0.0259	0.0204	0.0000	-0.0132	0.0006
0.020	0.816	1.0449	0.0148	0.0696	-0.0031	0.0097	-0.0061	0.0263	-0.0004	-0.0281	0.0004
0.020	1.293	1.1789	0.0178	0.0813	-0.0055	0.0124	-0.0027	0.0310	0.0003	-0.0267	-0.0009
0.020	2.052	1.2201	0.0238	0.0921	-0.0096	0.0171	-0.0056	0.0272	0.0004	-0.0206	-0.0018
0.020	3.250	1.2505	0.0516	0.1218	-0.0143	0.0207	0.0264	0.0252	-0.0013	-0.0253	-0.0019
0.045	0.816	1.0459	0.0123	0.0592	-0.0013	0.0025	0.0246	0.0149	0.0005	-0.0148	-0.0013
0.045	1.293	1.1908	0.0113	0.0720	-0.0036	0.0092	0.0272	0.0180	-0.0001	-0.0131	0.0001
0.045	2.052	1.3191	0.0154	0.0819	-0.0055	0.0108	0.0223	0.0188	0.0001	-0.0208	0.0000
0.045	3.250	1.3983	0.0173	0.0951	-0.0088	0.0155	0.0291	0.0214	0.0003	-0.0208	-0.0019
0.045	5.146	1.3728	0.0221	0.1076	-0.0121	0.0160	0.0392	0.0195	-0.0006	-0.0208	-0.0009
0.045	8.155	1.2974	0.0658	0.1276	-0.0156	0.0135	0.0483	0.0170	0.0006	-0.0374	0.0039
0.080	1.293	1.2053	0.0112	0.0596	-0.0014	0.0027	0.0238	0.0077	0.0000	0.0048	-0.0020
0.080	2.052	1.3039	0.0122	0.0646	-0.0031	0.0070	0.0230	0.0113	0.0001	-0.0057	0.0006
0.080	3.250	1.3630	0.0118	0.0743	-0.0055	0.0108	0.0234	0.0107	0.0001	-0.0260	0.0008
0.080	5.146	1.4266	0.0137	0.0828	-0.0073	0.0105	0.0287	0.0125	-0.0001	-0.0206	-0.0012
0.080	8.155	1.3939	0.0173	0.0953	-0.0102	0.0120	0.0325	0.0127	0.0001	-0.0172	-0.0022
0.080	12.925	1.4333	0.0386	0.1264	-0.0126	0.0127	0.0349	0.0135	0.0004	-0.0215	0.0038
0.125	2.052	1.2218	0.0102	0.0462	-0.0012	0.0026	0.0055	0.0044	0.0005	0.0098	-0.0015
0.125	3.250	1.2995	0.0109	0.0489	-0.0027	0.0055	0.0048	0.0046	0.0001	-0.0067	0.0006
0.125	5.146	1.3024	0.0102	0.0580	-0.0046	0.0081	0.0095	0.0055	0.0002	-0.0202	0.0004
0.125	8.155	1.3028	0.0115	0.0637	-0.0060	0.0075	0.0131	0.0073	-0.0001	-0.0145	-0.0013
0.125	12.925	1.3013	0.0146	0.0715	-0.0079	0.0082	0.0193	0.0089	-0.0001	-0.0136	-0.0010
0.125	20.520	1.2884	0.0302	0.0923	-0.0093	0.0080	0.0210	0.0099	-0.0006	-0.0107	0.0007
0.175	2.052	1.1185	0.0147	0.0552	-0.0005	0.0017	-0.0060	0.0013	0.0004	0.0443	-0.0006
0.175	3.250	1.1752	0.0124	0.0331	-0.0010	0.0021	-0.0063	0.0015	0.0004	0.0077	-0.0015
0.175	5.146	1.2061	0.0087	0.0389	-0.0026	0.0057	-0.0023	0.0043	-0.0002	-0.0012	0.0008

Table A.6: F_2 table (continued).

x	Q^2	F_2	σ_{stat}	σ_{syst}	sh 9	sh 10	sh 11	sh 12	sh 13	sh 14	sh 15
0.175	8.155	1.1984	0.0111	0.0401	-0.0035	0.0050	0.0011	0.0040	0.0001	-0.0090	0.0009
0.175	12.925	1.1767	0.0116	0.0492	-0.0048	0.0057	0.0048	0.0046	0.0002	-0.0090	-0.0018
0.175	20.520	1.1504	0.0143	0.0589	-0.0058	0.0054	0.0076	0.0062	-0.0001	-0.0079	0.0004
0.175	32.500	1.1226	0.0473	0.0822	-0.0065	0.0044	0.0090	0.0053	0.0000	-0.0045	-0.0019
0.225	3.250	1.0670	0.0126	0.0319	-0.0004	0.0012	-0.0091	0.0002	0.0004	0.0114	0.0002
0.225	5.146	1.0695	0.0094	0.0264	-0.0011	0.0023	-0.0065	0.0011	0.0007	0.0019	0.0007
0.225	8.155	1.0440	0.0086	0.0291	-0.0021	0.0041	-0.0038	0.0008	0.0000	-0.0039	0.0009
0.225	12.925	1.0323	0.0100	0.0341	-0.0029	0.0040	-0.0003	0.0029	-0.0002	-0.0046	-0.0008
0.225	20.520	0.9997	0.0118	0.0358	-0.0036	0.0037	0.0043	0.0032	-0.0003	-0.0068	-0.0004
0.225	32.500	1.0098	0.0193	0.0538	-0.0041	0.0034	0.0048	0.0030	0.0001	-0.0031	-0.0020
0.275	3.250	0.9735	0.0143	0.0326	0.0000	0.0013	-0.0056	-0.0019	-0.0004	0.0161	-0.0008
0.275	5.146	0.9363	0.0113	0.0254	-0.0004	0.0012	-0.0040	0.0007	-0.0001	-0.0035	0.0005
0.275	8.155	0.9275	0.0076	0.0217	-0.0011	0.0030	-0.0028	0.0008	0.0004	-0.0027	0.0011
0.275	12.925	0.9102	0.0097	0.0205	-0.0016	0.0025	0.0000	0.0019	0.0000	-0.0028	0.0001
0.275	20.520	0.8453	0.0096	0.0231	-0.0022	0.0027	0.0013	0.0022	-0.0001	-0.0055	-0.0005
0.275	32.500	0.8310	0.0114	0.0307	-0.0026	0.0024	0.0034	0.0025	0.0006	-0.0038	-0.0004
0.350	5.146	0.7531	0.0077	0.0403	0.0001	0.0006	0.0006	-0.0007	0.0003	-0.0144	0.0002
0.350	8.155	0.7110	0.0049	0.0252	-0.0003	0.0015	0.0010	-0.0005	-0.0003	-0.0073	0.0008
0.350	12.925	0.6620	0.0060	0.0245	-0.0005	0.0011	0.0013	0.0009	0.0001	-0.0066	0.0007
0.350	20.520	0.6338	0.0057	0.0188	-0.0009	0.0014	0.0023	0.0003	0.0002	-0.0042	-0.0001
0.350	32.500	0.6219	0.0063	0.0183	-0.0012	0.0015	0.0030	0.0008	-0.0002	-0.0037	-0.0006
0.350	51.455	0.5809	0.0095	0.0220	-0.0013	0.0012	0.0031	0.0022	-0.0001	-0.0049	0.0006
0.450	8.155	0.4811	0.0049	0.0408	0.0001	0.0004	0.0025	-0.0004	0.0001	-0.0176	0.0003
0.450	12.925	0.4363	0.0040	0.0291	0.0000	0.0007	0.0011	-0.0004	0.0001	-0.0106	0.0007
0.450	20.520	0.4060	0.0049	0.0271	-0.0001	0.0006	0.0015	0.0003	0.0002	-0.0065	0.0007
0.450	32.500	0.3779	0.0050	0.0217	-0.0003	0.0006	0.0009	0.0006	-0.0001	-0.0046	-0.0002
0.450	51.455	0.3438	0.0051	0.0156	-0.0004	0.0006	0.0009	0.0007	0.0003	-0.0026	0.0003

Table A.7: F_2 table (continued).

x	Q^2	F_2	σ_{stat}	σ_{syst}	sh 9	sh 10	sh 11	sh 12	sh 13	sh 14	sh 15
0.450	81.550	0.3264	0.0152	0.0159	-0.0004	0.0005	0.0008	-0.0001	-0.0004	-0.0038	0.0006
0.550	8.155	0.2949	0.0047	0.0415	0.0002	0.0002	0.0000	-0.0008	0.0000	-0.0248	0.0003
0.550	12.925	0.2484	0.0031	0.0289	0.0001	0.0003	-0.0009	0.0002	0.0002	-0.0133	0.0008
0.550	20.520	0.2253	0.0034	0.0249	0.0001	0.0003	-0.0013	-0.0001	0.0001	-0.0098	0.0005
0.550	32.500	0.2015	0.0032	0.0184	0.0000	0.0003	-0.0015	0.0001	0.0001	-0.0050	0.0000
0.550	51.455	0.1811	0.0039	0.0157	0.0000	0.0002	-0.0024	0.0004	0.0000	-0.0042	-0.0001
0.550	81.550	0.1658	0.0046	0.0117	-0.0001	0.0002	-0.0020	0.0003	0.0000	-0.0018	0.0003
0.650	8.155	0.1558	0.0038	0.0311	0.0002	0.0001	-0.0038	-0.0004	0.0000	-0.0190	-0.0005
0.650	12.925	0.1244	0.0022	0.0217	0.0001	0.0001	-0.0040	-0.0005	0.0000	-0.0125	0.0002
0.650	20.520	0.1035	0.0021	0.0170	0.0001	0.0001	-0.0042	-0.0001	-0.0001	-0.0080	0.0001
0.650	32.500	0.0863	0.0019	0.0123	0.0000	0.0001	-0.0034	0.0000	0.0000	-0.0039	0.0000
0.650	51.455	0.0830	0.0020	0.0111	0.0000	0.0001	-0.0035	0.0001	0.0001	-0.0031	-0.0001
0.650	81.550	0.0673	0.0023	0.0075	0.0000	0.0001	-0.0028	0.0004	0.0000	-0.0017	0.0003

APPENDIX B

xF_3 TABLE

This appendix contains the numerical values of the xF_3 found by 2-parameter fit. Table B.1 contains the explanations of the labels of the columns.

Table B.1: Explanation of the labels.

Label	**Explanation**	**Variation**
x	Central value of Bjorken-x	—
Q^2	Central value of Q^2 (GeV^2)	—
F_2	Extracted value of the Structure Function F_2	—
σ_{stat}	Statistical Uncertainty	—
σ_{syst}	Systematical Uncertainty	—
sh 1	Hadronic energy scale	5%
sh 2	Hadronic energy offset	150 MeV
sh 3	Muon momentum scale	2.5%
sh 4	Muon momentum offset	150 MeV/c
sh 5	Total ν-nucleon cross-section	2.1%
sh 6	Ratio of $\bar{\nu}$-nucleon and ν-nucleon cross-section	1.4%
sh 7	Non-linearity of the ν-nucleon cross-section	1%/100 GeV
sh 8	Non-linearity of the $\bar{\nu}$-nucleon to ν-nucleon cross-section ratio	0.5%/100 GeV
sh 9	Strange sea	$\Delta xF_3 \pm 20\%$
sh 10	Callan–Gross violation	$R \pm 20\%$
sh 11	Acceptance corrections	GRV94/GRV98
sh 12	Radiative corrections	CCFR/GRV98
sh 13	Reconstruction inefficiency	$\pm 5\%$
sh 14	Phenomenological corrections	on/off
sh 15	Hadronic energy resolution	2.5%

Table B.2: xF_3 table found by 2-parameter fit

x	Q^2	xF_3	σ_{stat}	σ_{syst}	sh 1	sh 2	sh 3	sh 4	sh 5	sh 6	sh 7	sh 8
0.020	0.325	0.1744	0.0353	0.0365	-0.0183	-0.0064	0.0217	0.0068	0.0037	-0.0134	-0.0015	0.0033
0.020	0.515	0.2482	0.0263	0.0268	-0.0157	-0.0055	0.0159	0.0074	0.0052	-0.0089	-0.0020	0.0021
0.020	0.816	0.2076	0.0220	0.0203	-0.0037	-0.0010	0.0145	0.0061	0.0044	-0.0084	-0.0018	0.0017
0.020	1.293	0.3155	0.0251	0.0242	-0.0076	-0.0002	0.0179	0.0067	0.0066	-0.0087	-0.0016	0.0011
0.020	2.052	0.3398	0.0291	0.0274	-0.0072	-0.0008	0.0210	0.0076	0.0071	-0.0078	-0.0008	0.0004
0.020	3.250	0.3448	0.0580	0.0234	-0.0095	0.0004	0.0132	0.0018	0.0072	-0.0076	0.0002	-0.0001
0.045	0.816	0.2962	0.0352	0.0356	-0.0157	-0.0042	0.0130	0.0050	0.0062	-0.0172	-0.0025	0.0041
0.045	1.293	0.3591	0.0184	0.0347	-0.0139	-0.0053	0.0201	0.0108	0.0075	-0.0099	-0.0027	0.0024
0.045	2.052	0.3957	0.0240	0.0320	-0.0041	-0.0008	0.0231	0.0067	0.0083	-0.0107	-0.0022	0.0020
0.045	3.250	0.4539	0.0229	0.0335	-0.0104	-0.0021	0.0238	0.0076	0.0095	-0.0092	-0.0018	0.0012
0.045	5.146	0.4823	0.0270	0.0315	-0.0085	-0.0008	0.0223	0.0065	0.0101	-0.0084	-0.0009	0.0002
0.045	8.155	0.5941	0.0778	0.0414	-0.0324	-0.0003	0.0199	0.0015	0.0125	-0.0072	0.0010	-0.0004
0.080	1.293	0.4562	0.0323	0.0543	-0.0208	-0.0091	0.0311	0.0115	0.0096	-0.0197	-0.0035	0.0049
0.080	2.052	0.5495	0.0229	0.0422	-0.0203	-0.0075	0.0223	0.0102	0.0115	-0.0117	-0.0039	0.0028
0.080	3.250	0.6133	0.0178	0.0436	-0.0099	-0.0010	0.0335	0.0144	0.0129	-0.0090	-0.0037	0.0020
0.080	5.146	0.6478	0.0200	0.0419	-0.0120	-0.0020	0.0321	0.0102	0.0136	-0.0092	-0.0025	0.0013
0.080	8.155	0.7249	0.0220	0.0433	-0.0126	0.0004	0.0351	0.0064	0.0152	-0.0073	-0.0010	0.0004
0.080	12.925	0.6371	0.0460	0.0441	-0.0116	-0.0048	0.0338	0.0108	0.0134	-0.0076	0.0004	-0.0002
0.125	2.052	0.5793	0.0295	0.0531	-0.0166	-0.0111	0.0293	0.0142	0.0122	-0.0191	-0.0042	0.0048
0.125	3.250	0.6755	0.0211	0.0386	-0.0155	-0.0043	0.0250	0.0114	0.0142	-0.0107	-0.0046	0.0025
0.125	5.146	0.7509	0.0154	0.0440	-0.0117	-0.0018	0.0348	0.0149	0.0157	-0.0075	-0.0043	0.0016
0.125	8.155	0.7823	0.0166	0.0396	-0.0076	-0.0003	0.0324	0.0083	0.0164	-0.0070	-0.0028	0.0010
0.125	12.925	0.7897	0.0189	0.0423	-0.0227	-0.0010	0.0297	0.0073	0.0165	-0.0059	-0.0008	0.0004
0.125	20.520	0.8431	0.0367	0.0515	-0.0266	0.0008	0.0391	0.0042	0.0177	-0.0050	0.0008	-0.0002
0.175	2.052	0.7335	0.0487	0.0594	-0.0079	-0.0012	0.0129	0.0055	0.0154	-0.0201	-0.0053	0.0052
0.175	3.250	0.6721	0.0356	0.0416	-0.0134	-0.0129	0.0183	0.0061	0.0141	-0.0164	-0.0049	0.0038
0.175	5.146	0.7554	0.0145	0.0349	-0.0057	-0.0036	0.0248	0.0107	0.0158	-0.0076	-0.0048	0.0018

Table B.3: xF_3 table (continued).

x	Q^2	xF_3	σ_{stat}	σ_{syst}	sh 1	sh 2	sh 3	sh 4	sh 5	sh 6	sh 7	sh 8
0.175	8.155	0.8047	0.0175	0.0297	-0.0038	-0.0014	0.0215	0.0071	0.0169	-0.0068	-0.0039	0.0013
0.175	12.925	0.8298	0.0158	0.0341	-0.0144	-0.0017	0.0242	0.0054	0.0174	-0.0048	-0.0024	0.0007
0.175	20.520	0.8352	0.0182	0.0391	-0.0226	-0.0001	0.0258	0.0050	0.0175	-0.0042	-0.0004	0.0001
0.175	32.500	0.7165	0.0584	0.0331	-0.0110	-0.0051	0.0253	0.0010	0.0150	-0.0049	0.0014	-0.0003
0.225	3.250	0.6923	0.0458	0.0399	-0.0025	-0.0163	0.0154	0.0103	0.0146	-0.0208	-0.0048	0.0052
0.225	5.146	0.6982	0.0215	0.0316	-0.0018	-0.0022	0.0204	0.0084	0.0147	-0.0108	-0.0046	0.0026
0.225	8.155	0.8044	0.0133	0.0263	-0.0009	-0.0002	0.0162	0.0078	0.0169	-0.0049	-0.0046	0.0011
0.225	12.925	0.7749	0.0142	0.0281	-0.0098	0.0001	0.0186	0.0060	0.0162	-0.0042	-0.0030	0.0007
0.225	20.520	0.7768	0.0154	0.0271	-0.0068	0.0001	0.0195	0.0031	0.0163	-0.0033	-0.0013	0.0003
0.225	32.500	0.7911	0.0241	0.0275	-0.0178	-0.0009	0.0100	-0.0002	0.0166	-0.0032	0.0006	-0.0001
0.275	3.250	0.7128	0.0473	0.0461	0.0201	0.0068	0.0144	-0.0021	0.0150	-0.0170	-0.0052	0.0044
0.275	5.146	0.6773	0.0325	0.0228	0.0046	-0.0031	-0.0025	0.0026	0.0142	-0.0120	-0.0044	0.0028
0.275	8.155	0.7368	0.0126	0.0179	0.0024	0.0000	0.0015	-0.0013	0.0155	-0.0046	-0.0045	0.0011
0.275	12.925	0.7091	0.0154	0.0173	0.0045	-0.0010	0.0013	0.0001	0.0149	-0.0044	-0.0033	0.0009
0.275	20.520	0.7297	0.0127	0.0190	-0.0082	0.0011	0.0049	0.0013	0.0153	-0.0022	-0.0021	0.0003
0.275	32.500	0.7034	0.0144	0.0209	-0.0123	0.0005	0.0074	0.0014	0.0147	-0.0021	-0.0001	0.0001
0.350	5.146	0.5820	0.0282	0.0219	0.0060	-0.0013	-0.0056	0.0027	0.0122	-0.0140	-0.0041	0.0033
0.350	8.155	0.6051	0.0097	0.0215	0.0117	0.0001	-0.0089	-0.0039	0.0127	-0.0047	-0.0040	0.0012
0.350	12.925	0.5819	0.0114	0.0211	0.0123	0.0003	-0.0098	-0.0030	0.0122	-0.0039	-0.0028	0.0008
0.350	20.520	0.5753	0.0083	0.0171	0.0084	0.0017	-0.0065	-0.0034	0.0121	-0.0020	-0.0020	0.0003
0.350	32.500	0.5781	0.0080	0.0149	-0.0007	0.0005	-0.0063	-0.0043	0.0121	-0.0012	-0.0009	0.0001
0.350	51.455	0.5391	0.0118	0.0174	-0.0123	0.0005	-0.0030	-0.0008	0.0113	-0.0011	0.0006	0.0000
0.450	8.155	0.3814	0.0141	0.0315	0.0187	0.0037	-0.0189	-0.0061	0.0080	-0.0063	-0.0026	0.0015
0.450	12.925	0.4037	0.0074	0.0276	0.0167	0.0029	-0.0171	-0.0070	0.0085	-0.0023	-0.0024	0.0005
0.450	20.520	0.3962	0.0085	0.0284	0.0168	0.0019	-0.0200	-0.0053	0.0083	-0.0018	-0.0017	0.0003
0.450	32.500	0.3630	0.0076	0.0239	0.0130	0.0010	-0.0173	-0.0051	0.0076	-0.0011	-0.0008	0.0001
0.450	51.455	0.3338	0.0063	0.0145	0.0009	0.0004	-0.0116	-0.0042	0.0070	-0.0005	0.0000	0.0000

Table B.4: xF_3 table (continued).

x	Q^2	xF_3	σ_{stat}	σ_{syst}	sh 1	sh 2	sh 3	sh 4	sh 5	sh 6	sh 7	sh 8
0.450	81.550	0.3234	0.0193	0.0124	0.0034	0.0004	-0.0081	-0.0011	0.0068	-0.0006	0.0005	-0.0001
0.550	8.155	0.2604	0.0174	0.0330	0.0220	0.0050	-0.0177	-0.0052	0.0055	-0.0053	-0.0018	0.0013
0.550	12.925	0.2327	0.0072	0.0249	0.0149	0.0023	-0.0163	-0.0042	0.0049	-0.0020	-0.0015	0.0005
0.550	20.520	0.2138	0.0066	0.0255	0.0151	0.0016	-0.0166	-0.0050	0.0045	-0.0012	-0.0010	0.0002
0.550	32.500	0.2038	0.0049	0.0194	0.0077	0.0009	-0.0157	-0.0037	0.0043	-0.0005	-0.0006	0.0001
0.550	51.455	0.1898	0.0057	0.0176	0.0093	0.0008	-0.0134	-0.0029	0.0040	-0.0004	-0.0001	0.0000
0.550	81.550	0.1767	0.0058	0.0125	0.0015	0.0001	-0.0109	-0.0027	0.0037	-0.0002	0.0002	0.0000
0.650	8.155	0.1325	0.0129	0.0289	0.0169	0.0054	-0.0132	-0.0033	0.0028	-0.0026	-0.0010	0.0007
0.650	12.925	0.1262	0.0054	0.0224	0.0119	0.0025	-0.0128	-0.0051	0.0027	-0.0009	-0.0008	0.0002
0.650	20.520	0.1008	0.0054	0.0168	0.0084	0.0014	-0.0111	-0.0034	0.0021	-0.0009	-0.0005	0.0002
0.650	32.500	0.0928	0.0033	0.0133	0.0070	0.0006	-0.0096	-0.0030	0.0019	-0.0003	-0.0004	0.0000
0.650	51.455	0.0803	0.0031	0.0105	0.0056	0.0005	-0.0072	-0.0011	0.0017	-0.0003	-0.0001	0.0000
0.650	81.550	0.0725	0.0033	0.0080	0.0034	-0.0002	-0.0059	-0.0009	0.0015	-0.0001	0.0001	0.0000

Table B.5: xF_3 table (continued).

x	Q^2	xF_3	σ_{stat}	σ_{syst}	sh 9	sh 10	sh 11	sh 12	sh 13	sh 14	sh 15
0.020	0.325	0.1744	0.0353	0.0365	0.0000	0.0002	0.0049	-0.0046	-0.0007	0.0137	-0.0001
0.020	0.515	0.2482	0.0263	0.0268	0.0000	0.0002	0.0003	-0.0036	-0.0001	0.0020	0.0009
0.020	0.816	0.2076	0.0220	0.0203	-0.0002	0.0012	0.0030	-0.0064	-0.0005	-0.0005	-0.0007
0.020	1.293	0.3155	0.0251	0.0242	-0.0001	0.0006	0.0004	-0.0059	-0.0006	-0.0018	-0.0001
0.020	2.052	0.3398	0.0291	0.0274	-0.0001	0.0001	0.0074	-0.0055	0.0002	0.0000	0.0008
0.020	3.250	0.3448	0.0580	0.0234	0.0000	-0.0008	-0.0017	-0.0098	0.0007	-0.0082	0.0017
0.045	0.816	0.2962	0.0352	0.0356	0.0000	0.0003	0.0181	-0.0074	-0.0004	0.0083	-0.0019
0.045	1.293	0.3591	0.0184	0.0347	0.0000	0.0000	0.0135	-0.0091	0.0003	0.0052	-0.0001
0.045	2.052	0.3957	0.0240	0.0320	0.0000	-0.0001	0.0134	-0.0075	-0.0005	-0.0009	-0.0009
0.045	3.250	0.4539	0.0229	0.0335	0.0001	-0.0006	0.0113	-0.0085	0.0007	-0.0008	-0.0014
0.045	5.146	0.4823	0.0270	0.0315	0.0000	-0.0002	0.0130	-0.0060	0.0004	-0.0006	0.0003
0.045	8.155	0.5941	0.0778	0.0414	0.0001	-0.0002	0.0046	-0.0055	-0.0012	-0.0018	0.0006
0.080	1.293	0.4562	0.0323	0.0543	0.0000	0.0002	0.0175	-0.0053	-0.0004	0.0218	-0.0021
0.080	2.052	0.5495	0.0229	0.0422	0.0001	-0.0004	0.0165	-0.0079	0.0002	0.0092	0.0010
0.080	3.250	0.6133	0.0178	0.0436	0.0002	-0.0009	0.0143	-0.0015	0.0005	-0.0002	0.0015
0.080	5.146	0.6478	0.0200	0.0419	0.0003	-0.0008	0.0128	-0.0053	-0.0009	-0.0016	0.0003
0.080	8.155	0.7249	0.0220	0.0433	0.0003	-0.0007	0.0122	-0.0030	-0.0001	-0.0001	0.0004
0.080	12.925	0.6371	0.0460	0.0441	0.0001	-0.0005	0.0165	-0.0015	0.0006	-0.0035	-0.0020
0.125	2.052	0.5793	0.0295	0.0531	0.0000	0.0000	0.0120	-0.0034	0.0007	0.0255	0.0000
0.125	3.250	0.6755	0.0211	0.0386	0.0001	-0.0006	0.0073	-0.0034	0.0003	0.0081	0.0001
0.125	5.146	0.7509	0.0154	0.0440	0.0004	-0.0012	0.0054	-0.0029	-0.0001	-0.0008	0.0008
0.125	8.155	0.7823	0.0166	0.0396	0.0005	-0.0013	0.0067	-0.0012	0.0006	-0.0036	-0.0005
0.125	12.925	0.7897	0.0189	0.0423	0.0004	-0.0009	0.0047	-0.0006	0.0000	-0.0020	-0.0011
0.125	20.520	0.8431	0.0367	0.0515	0.0003	-0.0005	0.0033	0.0001	0.0007	-0.0064	-0.0010
0.175	2.052	0.7335	0.0487	0.0594	0.0000	0.0000	0.0094	0.0006	0.0014	0.0498	-0.0002
0.175	3.250	0.6721	0.0356	0.0416	0.0000	0.0000	0.0069	-0.0049	-0.0006	0.0205	-0.0038
0.175	5.146	0.7554	0.0145	0.0349	0.0003	-0.0012	-0.0002	0.0000	-0.0008	0.0102	0.0013

Table B.6: xF_3 table (continued).

x	Q^2	xF_3	σ_{stat}	σ_{syst}	sh 9	sh 10	sh 11	sh 12	sh 13	sh 14	sh 15
0.175	8.155	0.8047	0.0175	0.0297	0.0003	-0.0009	-0.0009	-0.0005	-0.0005	-0.0005	0.0012
0.175	12.925	0.8298	0.0158	0.0341	0.0005	-0.0011	-0.0014	-0.0009	0.0004	-0.0007	-0.0017
0.175	20.520	0.8352	0.0182	0.0391	0.0003	-0.0006	-0.0009	0.0018	-0.0005	-0.0002	0.0003
0.175	32.500	0.7165	0.0584	0.0331	0.0001	-0.0001	-0.0021	0.0005	-0.0016	-0.0065	-0.0022
0.225	3.250	0.6923	0.0458	0.0399	0.0001	-0.0001	-0.0038	0.0005	-0.0025	0.0160	-0.0021
0.225	5.146	0.6982	0.0215	0.0316	0.0001	-0.0003	-0.0011	0.0010	0.0014	0.0118	0.0014
0.225	8.155	0.8044	0.0133	0.0263	0.0002	-0.0009	-0.0021	0.0023	0.0013	0.0047	0.0004
0.225	12.925	0.7749	0.0142	0.0281	0.0003	-0.0009	-0.0037	0.0018	-0.0006	0.0022	0.0001
0.225	20.520	0.7768	0.0154	0.0271	0.0003	-0.0007	-0.0035	0.0006	0.0002	-0.0022	0.0004
0.225	32.500	0.7911	0.0241	0.0275	0.0001	-0.0003	-0.0033	0.0009	-0.0002	-0.0059	-0.0019
0.275	3.250	0.7128	0.0473	0.0461	0.0001	0.0000	0.0002	0.0040	0.0004	0.0297	-0.0025
0.275	5.146	0.6773	0.0325	0.0228	0.0000	-0.0002	-0.0042	-0.0006	0.0002	0.0091	-0.0008
0.275	8.155	0.7368	0.0126	0.0179	0.0002	-0.0009	-0.0036	0.0002	-0.0001	0.0036	0.0007
0.275	12.925	0.7091	0.0154	0.0173	0.0002	-0.0006	-0.0040	-0.0003	0.0007	0.0019	0.0011
0.275	20.520	0.7297	0.0127	0.0190	0.0003	-0.0008	-0.0035	0.0007	0.0003	-0.0031	-0.0005
0.275	32.500	0.7034	0.0144	0.0209	0.0002	-0.0004	-0.0024	0.0017	0.0004	-0.0001	-0.0007
0.350	5.146	0.5820	0.0282	0.0219	0.0000	0.0000	-0.0053	-0.0006	-0.0009	0.0016	0.0000
0.350	8.155	0.6051	0.0097	0.0215	0.0000	-0.0005	-0.0039	-0.0001	-0.0005	-0.0039	0.0002
0.350	12.925	0.5819	0.0114	0.0211	0.0001	-0.0003	-0.0030	0.0005	0.0003	-0.0020	0.0010
0.350	20.520	0.5753	0.0083	0.0171	0.0001	-0.0004	-0.0019	0.0015	0.0003	-0.0023	0.0008
0.350	32.500	0.5781	0.0080	0.0149	0.0001	-0.0004	-0.0021	0.0008	-0.0001	-0.0032	-0.0006
0.350	51.455	0.5391	0.0118	0.0174	0.0001	-0.0002	-0.0013	0.0013	-0.0002	-0.0027	0.0018
0.450	8.155	0.3814	0.0141	0.0315	0.0000	-0.0001	-0.0025	0.0015	-0.0001	-0.0105	0.0012
0.450	12.925	0.4037	0.0074	0.0276	0.0000	-0.0003	-0.0017	0.0000	-0.0001	-0.0067	0.0007
0.450	20.520	0.3962	0.0085	0.0284	0.0000	-0.0002	-0.0005	0.0009	0.0003	-0.0042	0.0006
0.450	32.500	0.3630	0.0076	0.0239	0.0000	-0.0002	-0.0022	0.0003	-0.0001	-0.0032	-0.0002
0.450	51.455	0.3338	0.0063	0.0145	0.0000	-0.0002	-0.0010	0.0008	0.0002	-0.0027	0.0001

Table B.7: xF_3 table (continued).

x	Q^2	xF_3	σ_{stat}	σ_{syst}	sh 9	sh 10	sh 11	sh 12	sh 13	sh 14	sh 15
0.450	81.550	0.3234	0.0193	0.0124	0.0000	0.0000	-0.0018	0.0014	0.0005	-0.0047	-0.0013
0.550	8.155	0.2604	0.0174	0.0330	0.0000	0.0000	-0.0030	0.0010	-0.0004	-0.0130	0.0005
0.550	12.925	0.2327	0.0072	0.0249	0.0000	-0.0001	-0.0023	0.0001	0.0003	-0.0087	0.0003
0.550	20.520	0.2138	0.0066	0.0255	0.0000	-0.0001	-0.0035	0.0000	-0.0001	-0.0090	0.0008
0.550	32.500	0.2038	0.0049	0.0194	0.0000	-0.0001	-0.0029	0.0004	0.0001	-0.0053	0.0001
0.550	51.455	0.1898	0.0057	0.0176	0.0000	-0.0001	-0.0030	0.0004	-0.0001	-0.0032	-0.0003
0.550	81.550	0.1767	0.0058	0.0125	0.0000	0.0000	-0.0031	-0.0003	-0.0002	-0.0020	-0.0001
0.650	8.155	0.1325	0.0129	0.0289	0.0000	0.0000	-0.0076	-0.0004	-0.0001	-0.0162	-0.0010
0.650	12.925	0.1262	0.0054	0.0224	0.0000	0.0000	-0.0049	-0.0003	-0.0001	-0.0114	0.0000
0.650	20.520	0.1008	0.0054	0.0168	0.0000	0.0000	-0.0045	0.0002	-0.0001	-0.0069	0.0001
0.650	32.500	0.0928	0.0033	0.0133	0.0000	0.0000	-0.0032	0.0003	0.0000	-0.0034	-0.0002
0.650	51.455	0.0803	0.0031	0.0105	0.0000	0.0000	-0.0039	-0.0001	0.0000	-0.0027	0.0002
0.650	81.550	0.0725	0.0033	0.0080	0.0000	0.0000	-0.0037	0.0000	-0.0001	-0.0008	-0.0002